Fall 2014

Investigation Of Microstructural Alterations In M50 And 52100 Steel Using Nanoindentation

Kristin R. Paulson
Purdue University

Recommended Citation

Paulson, Kristin R., "Investigation Of Microstructural Alterations In M50 And 52100 Steel Using Nanoindentation" (2014). *Open Access Theses*. 365.
https://docs.lib.purdue.edu/open_access_theses/365

Graduate School Form 30
(Updated 11/20/2014)

PURDUE UNIVERSITY
GRADUATE SCHOOL
Thesis/Dissertation Acceptance

This is to certify that the thesis/dissertation prepared

By Kristin R Paulson

Entitled
INVESTIGATION OF MICROSTRUCTURAL ALTERATIONS IN M50 AND 52100 STEEL USING NANOINDENTATION

For the degree of Master of Science in Materials Science Engineering

Is approved by the final examining committee:

Rodney Trice

Farshid Sadeghi

David Johnson

To the best of my knowledge and as understood by the student in the Thesis/Dissertation Agreement, Publication Delay, and Certification/Disclaimer (Graduate School Form 32), this thesis/dissertation adheres to the provisions of Purdue University's "Policy on Integrity in Research" and the use of copyrighted material.

Approved by Major Professor(s): Rodney Trice

Approved by: David Bahr 12/08/2014

Head of the Department Graduate Program Date

INVESTIGATION OF MICROSTRUCTURAL ALTERATIONS IN M50 AND 52100 STEEL USING NANOINDENTATION

A Thesis
Submitted to the Faculty
of
Purdue University
by
Kristin R Paulson

In Partial Fulfillment of the
Requirements for the Degree
of
Master of Science in Materials Engineering

December 2014
Purdue University
West Lafayette, Indiana

For my dad.

ACKNOWLEDGEMENTS

First and foremost, I want to thank God for guiding me every step of the way, especially in times of doubt and wavering faith, and for teaching me lessons that go far beyond the scope of my Master's thesis and education. I would also like to thank my mom, my sisters, and my friends in far-off places for all of their love and support along the way and for always believing in me. A big thanks goes out to all of my friends here at Purdue because without all of you, my experience would not have been nearly as fun and exciting!

I would especially like to thank my advisor, Professor Rodney Trice, for all of the time he spent helping me become a better student/researcher/person. I can't imagine having had a better advisor, and I am especially grateful for his support in all aspects of my life. I would like to thank Professor Sadeghi for his guidance and help in choosing a project, as well as lending me the opportunity to work with industry. Finally, I would like to thank Professor Johnson for being on my committee.

TABLE OF CONTENTS

Page

LIST OF TABLES vii
LIST OF FIGURES viii
CHAPTER 1. INTRODUCTION 1
1.1 Motivation 1
1.2 Roller Bearings and Rolling Contact Fatigue 2
1.3 Bearing Material Selection 2
1.4 Heat Treatment and Resultant Bearing Steel Microstructure 5
1.5 Hertzian Pressure and Corresponding Stress States[15] 10
  1.5.1 General Contact Equation Applied to a Sphere-Cylinder Contact 10
  1.5.2 Three Ball-on-Rod Fatigue Testing 12
  1.5.3 Hertzian Pressure Distribution on Surface 13
  1.5.4 Maximum Shear Stress Distribution 13
1.6 Microstructural Alterations in Bearing Steels 15
  1.6.1 Dark Etching Regions 16
  1.6.2 30° WEB 18
  1.6.3 80° WEB 21
  1.6.4 Butterfly Transformations 22
1.7 Main Mechanisms of Formation 24
1.8 Previous Hardness Investigations 27
1.9 Goal And Approach 28
CHAPTER 2. EXPERIMENTAL PROCEDURE 30
2.1 Materials for Testing 30
2.2 Three Ball-on-Rod Testing 31

Page

2.2.1 Loading Parameters Used in Three Ball-on-Rod Test 36
2.3 Wear Track Measurements 37
2.3.1 M50 Steel Tested at a Load of 4.5 GPa for 10^8 Cycles 37
2.3.2 M50 Steel Tested at a Load of 5.0 GPa for 10^8 Cycles 37
2.3.3 52100 Steel Tested at a Load of 4.0/4.5 GPa for 10^8 Cycles 39
2.4 Experimental Design 39
2.5 Sample Preparation 41
2.5.1 Cutting and Surface Grinding 42
2.5.2 Mounting 44
2.5.3 Polishing 45
2.5.4 Optical Microscopy 47
2.6 Nanoindentation 48
2.6.1 Calibration 48
2.6.2 Automated Indentation 49
2.6.3 Indentation Using Scanning Probe Microscopy 50
2.6.4 Determination of Hardness and Elastic Modulus from Nanoindentation Data 51
2.7 Scanning Electron Microscopy 55
CHAPTER 3. RESULTS AND DISCUSSION 56
3.1 Starting Microstructure 58
3.1.1 M50 Steel 58
3.1.2 52100 Steel 61
3.2 Characterization of Microstructural Alterations 63
3.2.1 Lubricated/Unlubricated 4.5 GPa Loaded M50 to 108 Cycles (Microscopy) 63
3.2.2 Lubricated/Unlubricated 4.5 GPa Loaded M50 to 10^8 Cycles (Nanoindentation) 75
3.2.3 Lubricated/Unlubricated 5.0 GPa Loaded M50 to 108 Cycles 88
3.2.4 Lubricated 4.0/4.5 GPa Loaded 52100 to 10^8 Cycles 96
CHAPTER 4. CONCLUSIONS AND FUTURE RECOMMENDATIONS 106

Page

4.1 Microstructural Alterations 106
4.2 Hardness 107
4.3 Suggestions for Future Work 108
LIST OF REFERENCES 110

LIST OF TABLES

Table Page

1.1 Composition of M50 and AISI 52100 steel.[6] 4

1.2 X-ray diffraction measurements of altered structure compared with known interplanar spacing values for ferrite (α-iron).[37] 21

3.1 Overview of observations in all the test specimens. 57

3.2 Calculated maximum Hertzian pressures for the different investigated regions. 58

3.3 The average hardness calculated for Regions 1, 2, and 3 of the 4.5 GPa/10^8 cycles lubricated M50 sample. 82

3.4 Hardness measurements taken in different prior austenite grains as well as on the boundaries. 84

3.5 The average hardness values for indents taken within a prior austenite grain vs. indents taken on a prior austenite grain boundary. 84

3.6 The average hardness values from both 5.0 GPa/10^8 cycles M50 samples. 96

3.7 Comprehensive hardness table of the different regions for the 4.0/4.5 GPa 52100 samples. 105

LIST OF FIGURES

Figure Page

1.1 Hardness of 52100 compared to other aerospace grade bearing steels shows the significant drop in 52100 hardness as the temperature rises.[13] 4

1.2 Iron-carbon phase diagram depicting different phase fields and temperatures in which they occur.[10] 6

1.3 Time-temperature-transformation diagram for AISI 52100 steel.[5] 7

1.4 Time-temperature-transformation diagram for M50 steel.[6] 7

1.5 Morpholgy of plate martensite (a) containing 1.2%C and lath martensite (b) containing 0.2% C.[10] 9

1.6 This plot shows the effect of carbon on the M_s temperature as well as the amount of carbon on the martensite morphology.[10] 9

1.7 Semi-major and Semi-minor axes of elliptical contact from Hertzian pressure. 10

1.8 Principles stresses and maximum shear stress as a function of distance below the contact surface.[17] 14

1.9 The conditions in which DERs (DEA) and WEBs (flat/steep WB) are observed in SAE 52100 steel.[19] 15

1.10 Original microstructure is shown alongside a dark etching region that has manifested. The dark etching region seen on the left[26] is related to the region of maximum shear stress depicted on the right.[17] 17

1.11 30° white etching bands observed in the subsurface region in 52100 steel.[19] 19

1.12 Radial cross section of M50 steel displaying change in density of WEB from center of contact.[34] 19

1.13 Cracks, labeled with white arrows, can be seen running parallel to the white etching bands along lenticular carbides that are present in the microstructure.[31] 20

Figure Page

1.14 Both 30° and 80° white etching bands are observed in the rolling direction.[19] 21

1.15 Butterfly wings formed around an alumina inclusion with cracks above the upper wing and below the lower wing.[39] 23

1.16 Each successive image represents the same butterfly as it is serial sectioned.[40] 23

1.17 The development of hardness as a function of depth below the surface and the number of cycles experienced by the bearing. Likewise, the regions associated with the respective microstructural alterations are labeled.[38] 28

2.1 A Federal-Mogul RCF tester. The left image shows where the sample is loaded with an oil drip and the right image shows the machine controls and the hour count associated with the motor time........ 32

2.2 A bronze cage is used to separate and keep the balls in place during a rolling contact fatigue test. 33

2.3 A schematic illustrating the forces acting upon the cups which in turn is transferred to the ball and finally the cylindrical rod (adapted from Ref. 48). 34

2.4 Angle A associated with the tapered bearing cup is used to determine the horizontal force imparted on the balls. 34

2.5 A representative image of the spalling in the M50 samples loaded to 5.0 GPa. Each red line in the image is a millimeter. This can be compared to a representative wear track of a sampled loaded to 4.5 GPa in Figure 2.6. 38

2.6 The wear track of the 52100 cylindrical rod tested in rolling contact fatigue. 39

2.7 Image of the 4.5 GPa/10^8 cycles lubricated M50 wear track designating different locations in which indentation was performed as Regions 1, 2, and 3. 40

2.8 The approximate shear stress profiles associated with the differing Hertzian pressures in regions 1, 2, and 3 (R1, R2, R3, respectively) within the contact ellipse. 41

2.9 The vice that was used to hold the cylindrical bar while surface grinding. The notch in the right image helps assure the sample is correctly loaded and perpendicular to the wheel. 43

2.10 SEM image from one of the samples showing the spacing and set-up of a typical indentation array. 50

Figure Page

2.11 Upper portion of the unloading curve is fitted to solve for stiffness, S. 52

2.12 A cross sectional view of the geometry of the indenter-material 53

3.1 Pristine microstructure as observed in M50 steel that has not undergone rolling contact fatigue. 59

3.2 EDS spectrum showing the presence of molybdenum, vanadium, and chromium in the large white features of Figure 3.1. 59

3.3 (a) Prior austenite grain size in M50 Steel etched with 2% Nital at 500x. (b) PAGs in the same sample as (a) at 1000x. The white arrows point to the prior austenite grain boundaries.. 61

3.4 Starting microstructure for 52100 steel showing tempered martensite and finely distributed carbides at 1000x. 62

3.5 SEM imaged of 52100 microstructure after etching in 2% Nital showing the tempered martensite and spherical carbides present. 62

3.6 Both images are representative of the matrix microstructure as well as revealing butterflies (pointed out by the white arrows) that are present in region 2 of the 4.5 GPa/10^8 cycles lubricated M50 sample. 64

3.7 Images (a) and (b) show different types of butterflies observed in region 3 of the 4.5/10^8 cycles lubricated M50 sample. Figure 3.8a is a good representation of a butterfly centered on a dark etching inclusion and Figure 3.8b shows large butterfly wings emanating from a M_6C carbide as well as two smaller ones centered on dark etching inclusions. 64

3.8 At the same magnification (500x), the 4.5 GPa unlubricated M50 sample (a) contains a greater amount of butterflies in general as well as an increase in the number of butterflies of significant size relative to the 4.5 lubricated M50 sample in region 3 (b). The Vickers indent in image (a) is used as a reference point within the sample cross section.. 65

3.9 A white etching feature that occurs approximately 30° to the surface in the rolling direction is shown in the 4.5 GPa/10^8 cycles unlubricated M50 sample. 67

3.10 The white etching features are designated by the white arrows and the butterflies by the red arrows. They are all oriented in relatively the same direction. 67

Figure Page

3.11 (a) The original image and location within the sample, designated by a Vickers indent, of a microstructural alteration being examined (defined by white oval) and (b) the evolution of a butterfly in the predefined region shown in 12 slices. The single scale bar applies to all images. 69

3.12 SEM image of a butterfly centered around a dark-etching inclusion as shown by the arrow in M50 steel. 70

3.13 All the expected alloying elements of M50 (Mo, V, Cr) as well as Fe are present but aluminum and oxygen peaks are also present suggesting the dark etching center of a butterfly is formed around an alumina inclusion. 71

3.14 Both images show cracks present in two separate butterflies. 72

3.15 Very small acicular white etching areas (circled in (a) and marked with arrows in (b)) were also observed in region 3 of the 4.5 GPa/10^8 cycles lubricated M50 sample. 73

3.16 30° white etching bands (a few pointed out by the white arrows) observed in 52100 steel by Swahn.[38] 75

3.17 Hardness measurements as a function of depth beneath the surface in pristine M50 material of two separate data sets. 76

3.18 Hardness measurements as a function of depth beneath the surface in pristine M50 material for two more data sets. 77

3.19 Hardness measurements as a function of depth beneath the surface with 10 micron increments in Region 1. 78

3.20 Hardness measurements in two separate locations as a function of depth beneath the surface with 10 micron increments in Region 2. 79

3.21 Hardness measurements in two separate locations as a function of depth beneath the surface with 10 micron increments in Region 3. 80

3.22 Comprehensive hardness measurements as a function of depth beneath the surface with 10 micron increments in all regions indented in the 4.5 GPa/10^8 cycles lubricated M50 sample. 81

3.23 Pristine M50 and Region 1 were plotted with standard error bars and compared to observe data overlap. 81

Figure Page

3.24 Hardness values in a butterfly wing (outlined by dotted white line) as well as in the matrix surrounding it. 86

3.25 The values in this image are in GPa, and are performed just above a butterfly wing from Region 3 of the 4.5 GPa/10^8 cycles lubricated M50 sample. 87

3.26 Image (a) is shown to identify the white etching features examined in the nanoindenter using SPM. Image (b) is a topography image from the Hysitron TI-950 and the feature designated by the arrow is the same feature circled in Image (a). Values in Image (b) are in GPa. 88

3.27 The typical microstructure observed in Region 1 of the lubricated 5.0 GPa/10^8 cycles M50 sample. Cracks as the one seen in this image were commonly observed (500x). 89

3.28 More cracks observed in Region 2 of the lubricated 5.0 GPa/10^8 cycles M50 sample, but no microstructural alterations (500x). 89

3.29 Microstructure observed in Region 3 at 500x (left) and 1000x (right) of the lubricated 5.0 GPa/10^8 cycles M50 sample. Cracks are again observed in this region. 90

3.30 Microstructure in Region 1 of the unlubricated 5.0 GPa/10^8 cycles M50 sample. Cracks are observed near the surface. 90

3.31 Microstructure showing cracks in Region 2 of the unlubricated 5.0 GPa/10^8 cycles M50 sample. 91

3.32 Microstructure in Region 3 of the unlubricated 5.0 GPa/10^8 cycles M50 sample. Shows the same as Regions 1 and 2, however it was more lightly etched. 91

3.33 The spalling of the 5.0 GPa was severe as can be seen in image (a). Each red tick mark on the right represents a millimeter and the total width of spalling is on the order of 3 mm. It is compared to the spalling of a sample loaded at 4.5 GPa in image (b). 92

3.34 Hardness as a function of depth below the surface in which case the amount spalled off the surface was taken into consideration in Region 1 of the 5.0 GPa loaded to 10^8 cycles lubricated sample. 93

3.35 Hardness as a function of depth below the surface in which case the amount spalled off the surface was taken into consideration in Region 2 of the 5.0 GPa loaded to 10^8 cycles lubricated sample. 93

Figure Page

3.36 Hardness as a function of depth below the surface in which case the amount spalled off the surface was taken into consideration in Region 3 of the 5.0 GPa loaded to 10^8 cycles lubricated sample. 94

3.37 Hardness as a function of depth below the surface in which case the amount spalled off the surface was taken into consideration in Region 1 of the 5.0 GPa loaded to 10^8 cycles unlubricated sample. 94

3.38 Hardness as a function of depth below the surface in which case the amount spalled off the surface was taken into consideration in Region 2 of the 5.0 GPa loaded to 10^8 cycles unlubricated sample. 95

3.39 Hardness as a function of depth below the surface in which case the amount spalled off the surface was taken into consideration in Region 3 of the 5.0 GPa loaded to 10^8 cycles unlubricated sample. 95

3.40 Microstructure in Region 1 of the 4.5 GPa 52100 sample. No alterations are observed in this sample (a) (1000x) relative to the pristine microstructure but cracking is present as there was spalling (b) (500x). 97

3.41 Microstructure in Region 2 of 4.5 GPa/10^8 cycles 52100 sample showing no change. 98

3.42 Microstructure in Region 3 of 4.5 GPa/10^8 cycles 52100 sample showing no change. 98

3.43 Microstructure in Region 1 of 4.0 GPa/10^8 cycles 52100 sample showing no change. 99

3.44 Microstructure in Region 2 of 4.0 GPa/10^8 cycles 52100 sample showing no change. 99

3.45 Microstructure in Region 3 of 4.0 GPa/10^8 cycles 52100 sample showing no change microstructural change but this image contains an inclusion (most likely alumina). 100

3.46 Hardness measurements as a function of depth below the surface in a pristine 52100 specimen. 101

3.47 Hardness measurements as a function of depth below the surface in Region 1 of the 4.5 GPa loaded to 10^8 cycles 52100 sample. 102

3.48 Hardness measurements as a function of depth below the surface in Region 2 of the 4.5 GPa loaded to 10^8 cycles 52100 sample. 102

Figure Page

3.49 Hardness measurements as a function of depth below the surface in Region 3 of the 4.5 GPa loaded to 10^8 cycles 52100 sample. 103

3.50 Hardness vs. distance below surface in Region 1 of the 4.0 GPa loaded sample to 10^8 cycles. 103

3.51 Hardness vs. distance below surface in Region 2 of the 4.0 GPa loaded sample to 10^8 cycles. 104

3.52 Hardness vs. distance below surface in Region 3 of the 4.0 GPa loaded sample to 10^8 cycles. 104

ABSTRACT

Paulson, Kristin R. M.S.M.S.E., Purdue University, December 2014. Investigation of Microstructural Alterations in M50 and 52100 Steel Using Nanoindentation. Major Professor: Rodney Trice.

Bearing steels are used in rolling elements and are designed to withstand heavy loads for an extended period of time. At the end of life, microstructural alterations within the material have been observed and are linked to failure. In this study, a three ball-on-rod fatigue tester was used to test M50 and 52100 steel cylindrical rods at differing loads of 4.0 GPa, 4.5 GPa, and 5.0 GPa and in lubricated and unlubricated conditions to 10^8 cycles in an attempt to produce microstructural alterations. Microstructural alterations characterized as butterflies were observed and investigated further in two M50 samples that were tested at 4.5 GPa to 10^8 cycles in the lubricated and unlubricated condition. Microstructural alterations characterized as dark etching regions (DER), and white etching bands (WEBs) were not observed. Additionally, hardness was investigated cross sectionally as a function of depth and location within the wear track produced by the fatigue test. No conclusive evidence was derived from the hardness measurements as a function of depth in relation to the formation of microstructural alterations or the stress experienced subsurface within the material. Hardness measurements performed specifically within a butterfly wing, however, returned hardness values significantly higher than the matrix hardness values.

CHAPTER 1. INTRODUCTION

1.1 Motivation

Rolling-element bearings are machine components used to allow rotary motion while withstanding heavy loads and are some of the most widely used components in industry today.[1] They are used in a multitude of applications, some of which include gearboxes, transmissions, gas turbines, etc., and are typically the heaviest loaded parts within a mechanical system.[2] With that said, it becomes extremely important to use the correct materials able to withstand those loads at an elevated number of cycles in order to maximize bearing life.

More often than not, the life of these bearings are defined by their rolling contact fatigue (RCF) life.[3] A valuable approach to comprehending the RCF life is understanding the microstructural features within the steel and the possible defects or planes of weakness that potentially lead to RCF failure. If the mechanisms of failure can be understood, engineers can work towards solutions to prevent it from happening in the future. Possible future solutions may include better processing and heat treatment techniques for current rolling-element steels in order to refine the microstructure or implementing newer/better materials more readily equipped to withstand the required conditions associated with rolling contacts.

1.2 Roller Bearings and Rolling Contact Fatigue

Because of high contact pressures, cyclical loading, inherent material defects, and the surrounding environment associated with rolling-element contacts, multiple types of failures can occur. The different types of failures include wear, galling, plastic indentation, heat imbalance, and rolling contact fatigue.[4] The most common failure that occurs if a rolling-element is loaded and lubricated properly and run in an uncontaminated environment is thought to be rolling contact fatigue (RCF).[3] Fatigue in materials occurs due to the accumulation of plastic deformation.[5] RCF failures are observed as either surface-originated pitting or subsurface-originated spalling.[3] Both modes of failure involve material removal but with different origins. Surface-originated pitting nucleates from surface damage, however, if the surfaces are in good condition, subsurface-originated spalling dominates RCF damage.[1] Subsurface-originated spalling occurs when a subsurface crack forms at a material defect such as an inclusion. The crack then propagates to the surface and small material flakes are removed to form spalls. These failures can occur in a multitude of systems of which include rail/wheel interactions, bearings, gears, and camshaft/follower mechanisms.[6,7]

1.3 Bearing Material Selection

Although RCF is inevitable, proper material selection plays a significant role in the lifetime of bearing elements. Selection credentials include hardenability resulting in high hardness, toughness, steel cleanliness, good wear resistance, and dimensional stability.[8] It has been proven that as the hardness increases the L_{10} life, or number of revolutions experienced by bearings with a 90% reliability rating, increases for roller bearings.[9] Since the early 1900s, an AISI 52100 type steel has been used and is still the most widely used bearing steel today.[10,11] AISI 52100's high carbon content (~1%) and chromium alloying addition (~1.5%) increases the hardenability of the steel[12] allowing it to be through hardened.

Even though AISI 52100 has been used for over 100 years, new technologies during that time have assisted in increasing the quality of steel and hence bearing life. One major contribution was the vacuum-induction melted, vacuum-arc remelted process (VIM-VAR).[13] The VIM-VAR process enhanced steel cleanliness and substantially improved the RCF life by a factor of 100 compared to bearing life in the 1940s.[13]

Another commonly used bearing steel is M50. The composition for both AISI 52100 and M50 are given in Table 1.1. M50 has more alloying elements compared to AISI 52100 and a greater percentage of chromium (~4%). The necessity for M50 and other similar bearing steels was due to a limited operating temperature of AISI 52100.[14] Above 125-175°C, the hot hardness of AISI 52100 drops significantly as depicted in Figure 1.1.[8]

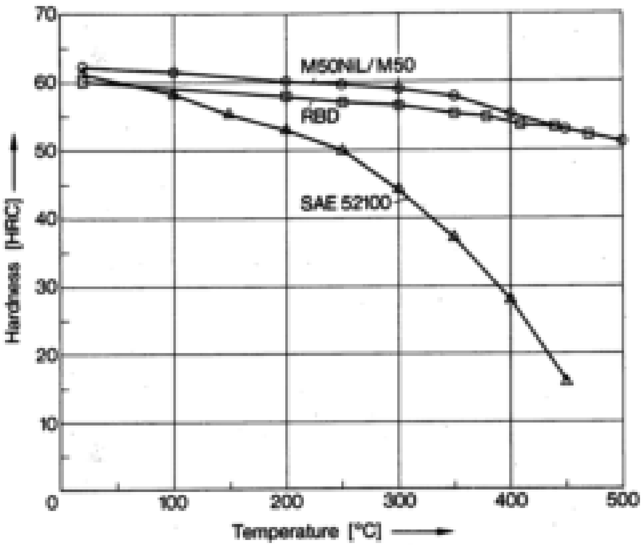

Figure 1.1 Hardness of 52100 compared to other aerospace grade bearing steels shows the significant drop in 52100 hardness as the temperature rises.[15]

M50 cannot only operate at higher temperatures, but it can also withstand higher loads. There are a multitude of bearing steels that are used in service today, but for the purpose of this thesis, the focus will be on AISI 52100 and M50.

Table 1.1 Composition of M50 and AISI 52100 steel.[8]

	%C	%Mn	%Si	%Cr	%Ni	%Mo	%Cu	%S	%P	%V
M50	0.77-0.85	≤0.35	≤0.25	3.75-4.25	≤0.15	4.0-4.5	≤0.1	≤0.015	≤0.015	0.9-1.1
AISI 52100	0.95-1.1	0.2-0.5	≤0.35	1.3-1.6	-	-	≤0.025	≤0.025	-	-

1.4 Heat Treatment and Resultant Bearing Steel Microstructure

The desired microstructure for M50 and AISI 52100 steels is tempered martensite. This particular microstructure offers high hardness, with increased ductility compared to quenched martensite, which in turn enhances the wear properties of the material. To form this microstructure, the steel typically goes through a number of thermal cycles that may include annealing, normalizing, hardening, and tempering.

For the purpose of this section, assume the steel part is received in its desired shape for service but still needs to be heat treated to attain its desired microstructure. With this as-received steel, the first step to is to austenitize it. The goal of austenitization is to produce a uniform microstructure of austenite. Austenite is a face-centered cubic structure that occurs at elevated temperatures on the iron-carbon phase diagram as shown in Figure 1.2.

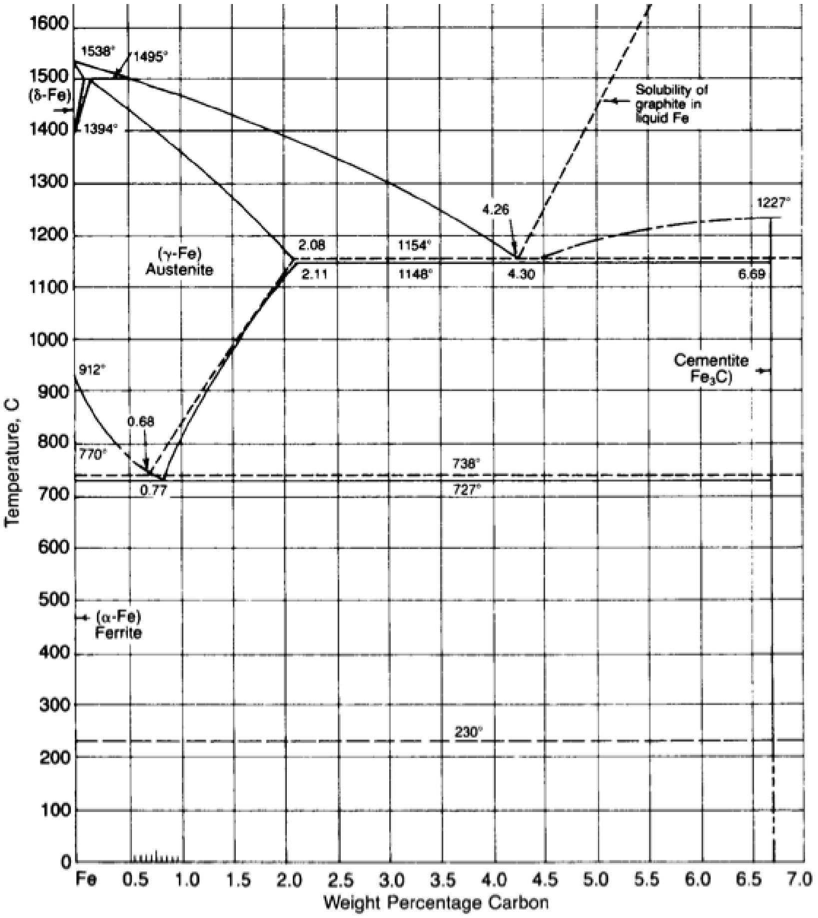

Figure 1.2 Iron-carbon phase diagram depicting different phase fields and temperatures in which they occur.[12]

Martensite is produced by rapidly cooling (quenching) the steel in a medium of water, salt, or oil. If the cooling rate is too fast, quench cracks may be the result, but if it is too slow, undesired microstructures may form, such as pearlite. In order to balance these things, a time-temperature transformation (TTT) diagram is needed. Figure 1.3 is a representative TTT diagram and illustrates at what time and temperature different microstructural transformations will occur in AISI 52100 steel.

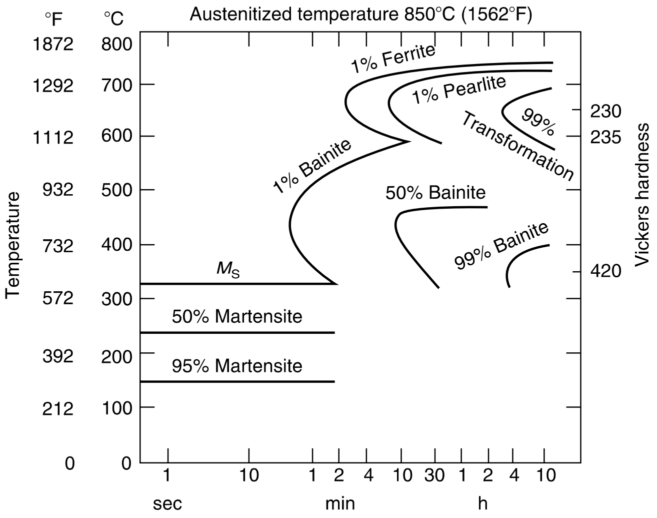

Figure 1.3 Time-temperature-transformation diagram for AISI 52100 steel.[5]

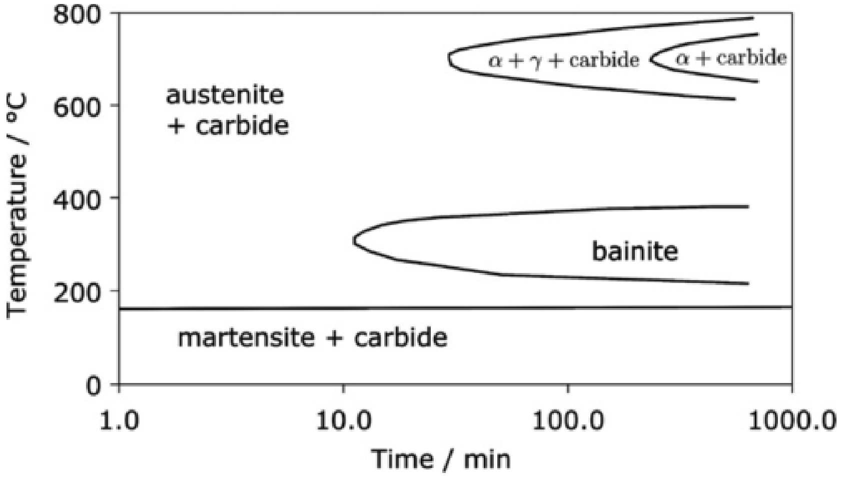

Figure 1.4 Time-temperature-transformation diagram for M50 steel.[8]

According to Figure 1.3, martensite begins to transform at the martensite start temperature, M_s, of approximately 325°C and reaches 95% transformation just below 150°C.

Both AISI 52100 and M50 steel are through-hardened. This means the part completely transforms from retained austenite to martensite on the surface and reaches at least a 50% transformation to martensite in the center.[12] Martensite is the hardest microstructure in steel and hence is desirable in bearing steel applications. When the steel is quenched from austenite to martensite, it transforms from a face-centered cubic (FCC) structure to a body-centered tetragonal (BCT) structure. The carbon atoms become trapped in the octahedral interstitial sites because of the high cooling rate and do not have time to diffuse to a more stable phase. This causes distortion of the lattice, which in turn makes it more difficult for dislocation motion. Suppressed dislocation motion coupled with a high density of dislocations in martensite are what contribute to its high strength.[12] In its original quenched state, however, it can be very brittle.[12] The final step is to temper the steel, which is performed by holding at elevated temperatures below the M_s. This increases the toughness and relieves stresses imparted by quenching because carbon diffuses out of the martensitic matrix relieving lattice distortion and forming epsilon or eta carbides.[5,12]

When this process is complete, homogeneously distributed spherical Cr-carbides in a martensitic matrix with approximately 6-10% retained austenite is observed.[16] Plate martensite starts to form in systems that contain over 0.6% C as can be seen in Figure 1.6 and therefore is the dominate martensitic structure in bearing steels rather than lath martensite. An image of both types of martensite are shown in Figure 1.5.

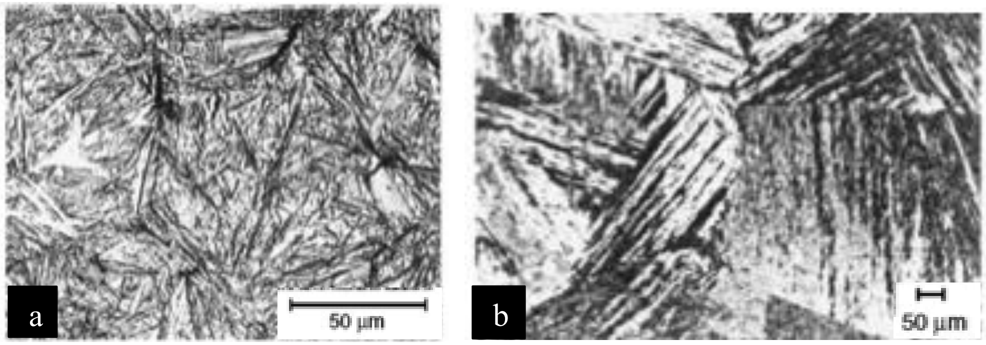

Figure 1.5 Morpholgy of plate martensite (a) containing 1.2%C and lath martensite (b) containing 0.2% C.[12]

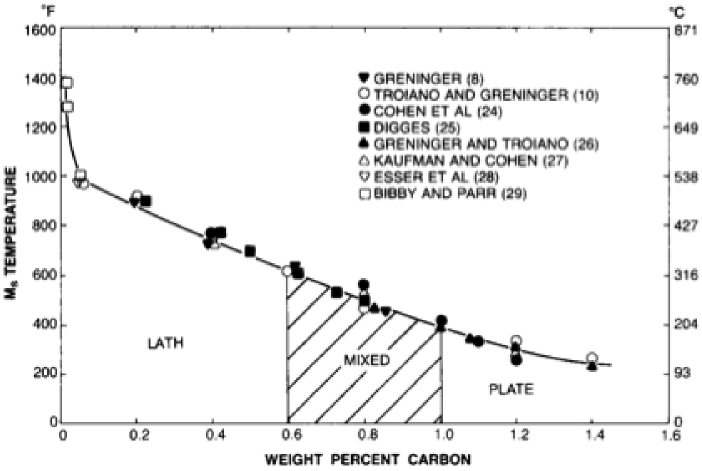

Figure 1.6 This plot shows the effect of carbon on the M_s temperature as well as the amount of carbon on the martensite morphology.[12]

Plate martensite is distinguishable by the multiple orientations in which it is observed because it forms on irrational habit planes that have multiple variants.[12] The distinguishable feature of lath martensite is multiple martensitic laths orienting themselves in the same direction within a prior austenite grain. Martensitic plates tend to be larger and are easily observed using optical microscopy, but martensitic laths tend to be approximately 0.5 µm in width[12] and are therefore difficult to observe because that is below the resolution limit of a light microscope.

1.5 Hertzian Pressure and Corresponding Stress States[17]

1.5.1 General Contact Equation Applied to a Sphere-Cylinder Contact

The general contact equation for two solids with known radii of curvature is as follows:

$$P_0 = 1.5\frac{F}{\pi ab} \tag{1.1}$$

Where P_0 is the maximum Hertzian pressure, F is the applied force and *a* and *b* are semi axes of the contact area, shown in Fig. 1.7 and defined as:

$$a = c_a\sqrt[3]{\frac{Fm}{n}} \tag{1.2}$$

$$b = c_b\sqrt[3]{\frac{Fm}{n}} \tag{1.3}$$

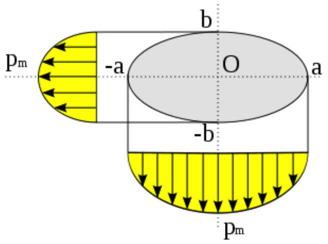

Figure 1.7 Semi-major and Semi-minor axes of elliptical contact from Hertzian pressure.

and m and n are defined as:

$$m = \frac{4}{\left(\frac{1}{r_1} + \frac{1}{r_1'} + \frac{1}{r_2} + \frac{1}{r_2'}\right)} \tag{1.4}$$

$$n = \frac{4E}{3(1 - \nu)} \tag{1.5}$$

and E is Young's Modulus, and ν is Poisson's Ratio . The constants c_a and c_b are given in literature in relation to α, which is defined as:

$$cos\,\alpha = \frac{B}{A} \tag{1.6}$$

and A and B are defined as:

$$A = \frac{2}{m} \tag{1.7}$$

$$B = \frac{1}{2}\left[\left(\frac{1}{r_1} - \frac{1}{r_1'}\right)^2 + \left(\frac{1}{r_2} - \frac{1}{r_2'}\right)^2 + 2\left(\frac{1}{r_1} - \frac{1}{r_1'}\right)\left(\frac{1}{r_2} - \frac{1}{r_2'}\right) cos\,2\theta\right]^{\frac{1}{2}} \tag{1.8}$$

Now let r_1 be the minimum radius of curvature for a cylinder, r_1' be the maximum radius of curvature for a cylinder, r_2 be the minimum radius of curvature for a sphere, r_2' be the maximum radius of curvature for a sphere, and θ be the angle between the normal planes in which radii r_1 and r_2 lie.

Since the cylinder and ball dimensions are known as well as the Young's modulus and Poisson's ratio for steel, constants m, n, A, and B can be determined. Alpha, α, is then determined using the values for A and B and the corresponding values for c_a and c_b can be found in literature. The general contact equation is then rearranged to solve for force, F:

$$F = \frac{{P_0}^3 (\pi c_a c_b)^3 m^2}{1.5^3 n^2} \tag{1.9}$$

F is solved for because the user determines the desired Hertzian pressure is the determined value and the corresponding force needed to produce the Hertzian pressure is calculated. It is important to know these equations to be able to use a three-ball-on-rod fatigue test rig.

1.5.2 Three Ball-on-Rod Fatigue Testing

Because full-scale rolling-element testing is expensive and time-consuming, it is desirable to use a machine that accelerates the process and simplifies the part geometry. This is the purpose of the three ball-on-rod fatigue tester. The machine allows accelerated testing times by creating three points of contact from three roughened balls on a cylindrical rod sample. The specifics of the three ball-on-rod fatigue tester will be discussed in more detail in a later section.

1.5.3 Hertzian Pressure Distribution on Surface

The maximum Hertzian pressure is observed at the center of the elliptical contact (Fig. 1.7), but the distribution of the Hertzian pressure on the surface is also of interest. To calculate the Hertzian pressure at any point within the elliptical contact, the following equation[18] can be used:

$$P(x,y) = P_0\left\{1 - \left(\frac{x}{a}\right)^2 - \left(\frac{y}{b}\right)^2\right\}^{\frac{1}{2}} \tag{1.10}$$

where P_0 is the maximum Hertzian pressure, a and b are the semi-axes of the contact ellipse as defined in equations (2) and (3), and x and y boundary conditions are as follows:

$$-a \leq x \leq a$$

$$-b \leq y \leq b$$

1.5.4 Maximum Shear Stress Distribution

As discussed in section 1.1, failure often occurs some distance below the surface where cracks form. This can be attributed to the maximum shear stress occurring in the same subsurface region.[5] To better illustrate this phenomenon, the equations that govern the maximum shear stress as a function of depth are given below. First, the principal stresses must be calculated (for a point contact)[19]:

$$\sigma_x = \sigma_y = \sigma_1 = \sigma_2 = -P_0\left[\left(1 - |\zeta_a|\, tan^{-1}\frac{1}{|\zeta_a|}\right)(1+\upsilon) - \frac{1}{2(1+{\zeta_a}^2)}\right] \tag{1.11}$$

$$\sigma_3 = \sigma_z = \frac{-P_0}{1 + {\zeta_a}^2} \tag{1.12}$$

in which P_0 is the maximum Hertzian pressure, $\zeta_a = z/a$, the dimensionless depth below the surface, and υ is Poisson's ratio. From the principles stresses, the shear stress is obtained:

$$\tau_{max} = \frac{\sigma_x - \sigma_z}{2} = \frac{\sigma_y - \sigma_z}{2} = \frac{\sigma_1 - \sigma_3}{2} \tag{1.13}$$

By inputting different values for ζ_a, the shear stress can be plotted as a function of depth below the surface as illustrated in Figure 1.8. Although the principal stresses are maximized at the contact surface, the shear stress maximum occurs some distance below the surface. This subsurface maximum shear stress zone is important in understanding microstructural alterations in bearing steels.

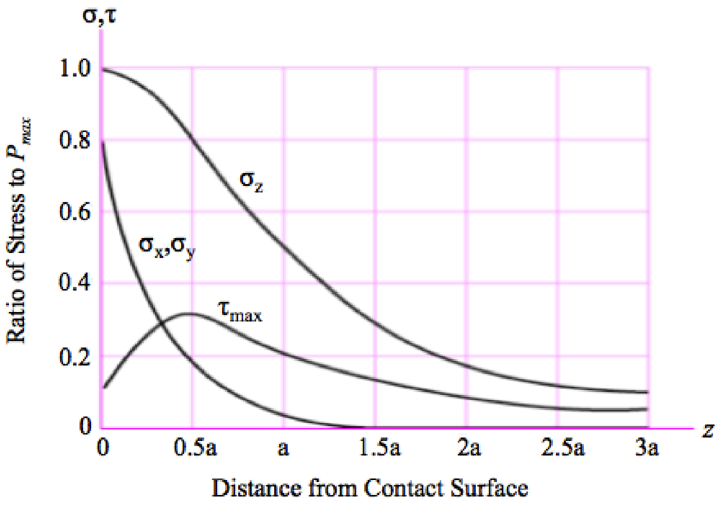

Figure 1.8 Principles stresses and maximum shear stress as a function of distance below the contact surface.[19]

1.6 Microstructural Alterations in Bearing Steels

Microstructural alterations due to RCF were first observed by Jones in 1947.[20] These alterations have been referred to as many different names, but are now commonly known as dark etching regions (DER), white etching bands (WEB), and butterflies. Each is named for how they appear under an optical microscope. Two categories of WEBs exist: 30° white etching bands and 80° white etching bands. The 30° and 80° correspond to the distinct directions each respective band makes with the raceway surface in the rolling direction. All three alterations are typically observed together in a linear progression of DER, followed by 30° WEB and finally 80° WEB. Figure 1.9 illustrates this and shows the range of cycles/loads in which these alterations appear in 52100 steel.[21]

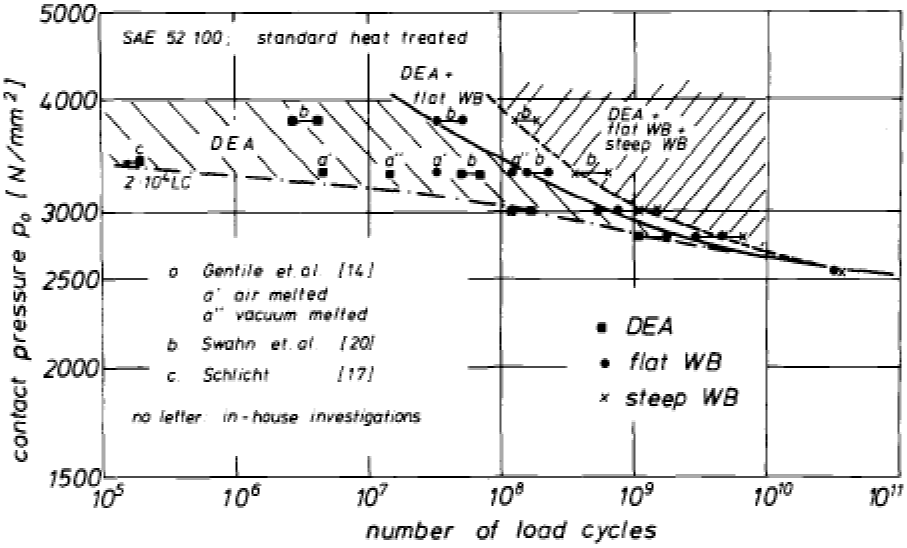

Figure 1.9 The conditions in which DERs (DEA) and WEBs (flat/steep WB) are observed in SAE 52100 steel.[21]

DER can be seen as early as 10^5 cycles. 30° WEBs, however, do not appear until approximately 10^7 cycles, and 80° WEBs, not until 10^8 cycles.[21] Butterfly alterations can form at much lower maximum Hertzian stresses (<1.5 GPa) than DERs and WEBs and are observed around nonmetallic inclusions in the steel matrix. Although the point in life in which butterflies first form is unknown, it is hypothesized to be between a tenth and a thousandth of the bearing life. Each alteration will be discussed in more detail in the following sections.

1.6.1 Dark Etching Regions

As previously stated, dark etching regions are regions etched much darker relative to the parent martensite matrix when viewed under an optical microscope and are characterized by ferritic microbands in between the original martensitic matrix. At this stage, the overall carbon content in this region is the same as the parent martensite.[22,23] The parent martensite disappears and is replaced by a dislocation cell structure that appears in the form of the ferritic microbands.[24] It is initiated in the region of maximum shear stress as depicted in Fig. 1.10 and is associated with the migration of carbon atoms to heavily dislocated regions.[25, 26, 27]

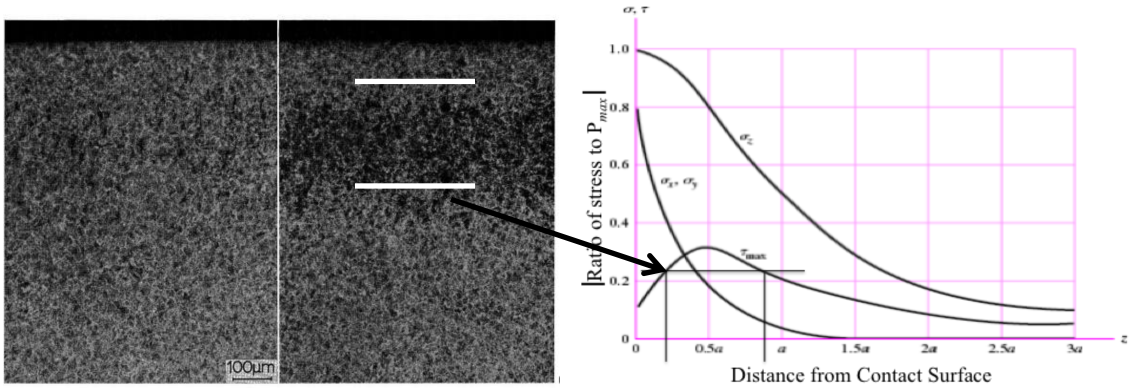

Figure 1.10 Original microstructure is shown alongside a dark etching region that has manifested. The dark etching region seen on the left[28] is related to the region of maximum shear stress depicted on the right.[19]

In these regions, the hardness decreased compared to the original matrix.[29] A {100}<110> texture was observed in heavily loaded (>4.5 GPa) bearings run at a moderate temperature (<55°C)[27] and a {111}<112> texture was observed in moderately loaded bearings (3.8 GPa) run at a higher temperature (90°C).[30,31] The DER width also increases as the number of cycles increase.[29] It is interesting to note that DERs are not observed if the steel is tempered to a hardness of 57 HRC.[8] This is most likely related to the fact that DER microstructure resembles high-temperature tempered martensite.[25] Correspondingly, as the plastic deformation (slip) within the material increases, the microstructure etches darker.[25,32] The hardness within this region is decreased in relation to the parent matrix by approximately 140 HVN (1.3 GPa) and the minimum hardness value shifts toward the surface as the number of cycles increases.[21]

1.6.2 30° WEB

30° white etching bands appear after dark etching regions at approximately 10^7 cycles[21] and get their name from the distinct direction they form in relation to the raceway. They typically make an angle ranging from 26°-32° with the raceway in the rolling direction with the angle decreasing as the depth below the surface increases.[33] The specific band angles are also dependent on contact conditions, lubrication and frictional heating. They are characterized by their white, disc-like morphology that is composed of a dislocation cell structure of ferrite[34] that contains a dislocation density comparable to martensite.[25,35] They are 5-30 µm in length, 2µm in width, and are spaced 0.5 to 10 µm apart (Fig. 1.11).[26] The range beneath the surface in which the 30° bands are observed is 200-760 µm (region of maximum shear stress)[26] but this range is dependent on the geometry of the parts used in rolling contact. The density of the WEBs reach a maximum under the center of the wear track and decreases as distance from the center increases as shown in Figure 1.12.

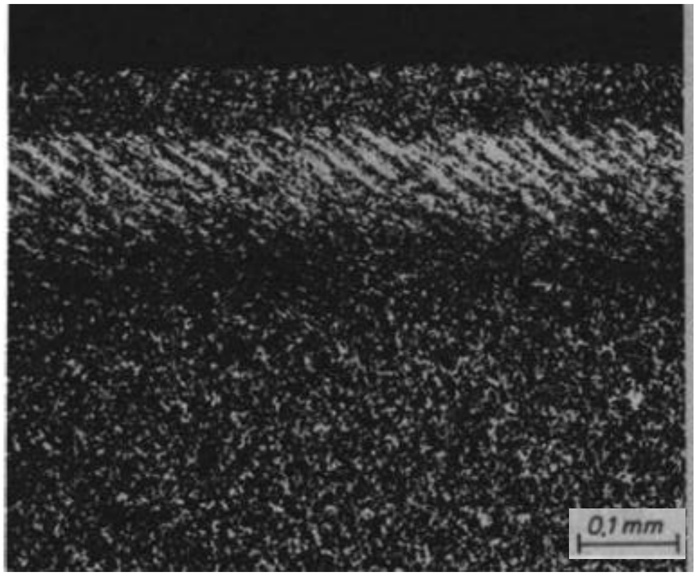

Figure 1.11 30° white etching bands observed in the subsurface region in 52100 steel.[21]

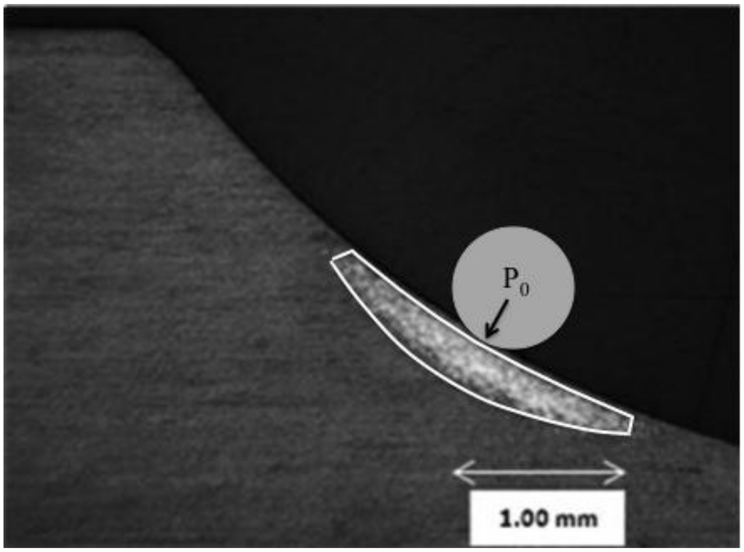

Figure 1.12 Radial cross section of M50 steel displaying change in density of WEB from center of contact.[36]

There are no carbides present within the bands themselves, but lenticular carbides are present running parallel to the WEBs.[26] Cracking has been associated with lenticular carbides as is shown in Figure 1.13.

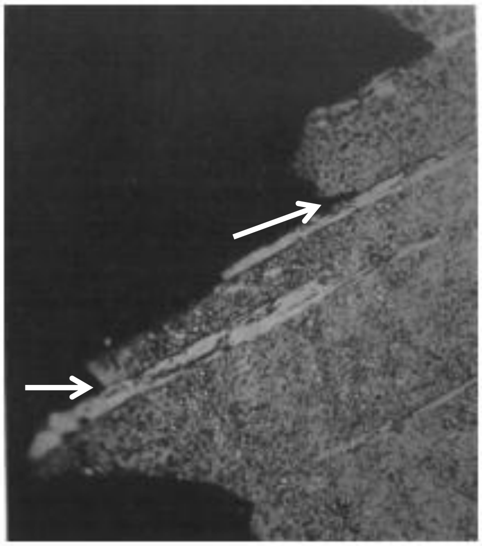

Figure 1.13 Cracks, labeled with white arrows, can be seen running parallel to the white etching bands along lenticular carbides that are present in the microstructure.[33]

However, even though lenticular carbides are observed in 52100 steel, they are not present in all bearing steels. When investigating WEBs in M50 steel, no lenticular carbides were detected.[37] The bands themselves have almost no carbon present (0.06%) but the surrounding material was found to contain 1.25% C.[38] As previously stated, ferrite comprises the WEB microstructure and was determined by using x-ray diffraction. The results are given in Table 1.2.[39]

Table 1.2 X-ray diffraction measurements of altered structure compared with known interplanar spacing values for ferrite (α-iron).[39]

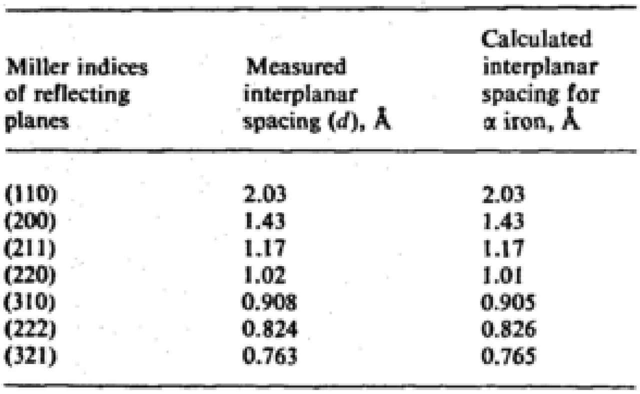

Miller indices of reflecting planes	Measured interplanar spacing (d), Å	Calculated interplanar spacing for α iron, Å
(110)	2.03	2.03
(200)	1.43	1.43
(211)	1.17	1.17
(220)	1.02	1.01
(310)	0.908	0.905
(222)	0.824	0.826
(321)	0.763	0.765

1.6.3 80° WEB

80° white etching bands are the final observed alteration in the bearing steel and can appear after approximately 10^8 cycles with a high enough load.[21] As the name implies, these bands form at a higher angle of approximately 70-80° with respect to the surface in the rolling direction.[21] They form in the same region over the 30° WEBs, but are centered at a depth closer to the surface as shown in Fig. 1.14.

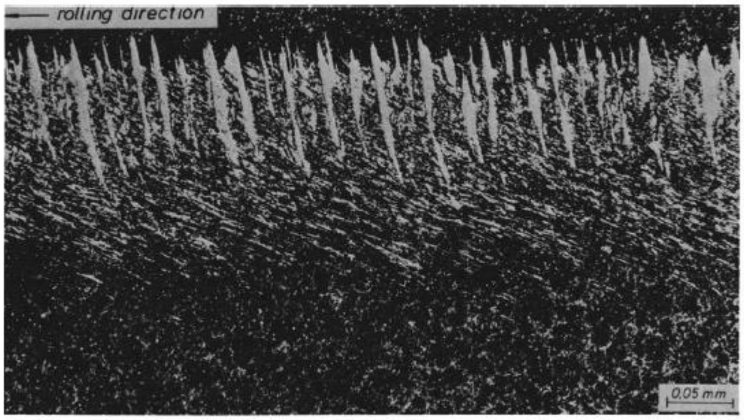

Figure 1.14 Both 30° and 80° white etching bands are observed in the rolling direction.[21]

These bands also do not have any carbon present[23,40] and consist of nano-sized ferrite grains on the order of 20 nanometers that are significantly plastically deformed.[5] The mechanism of formation for the 80° WEBs is unknown but it must include the break-up of the lenticular carbides associated with the 30° bands since the 80° bands overlay them.[40] Figure 1.14 illustrates the larger dimensions of the 80° bands. They are typically 10 μm in width, 50-100 μm in length, and are spaced 5-50 μm apart.

1.6.4 Butterfly Transformations

Another microstructural transformation that occurs in bearing steels associated with rolling contact fatigue is called a butterfly. It is considered a type of white etching area (WEA)[5] and is named a butterfly because of the wing-like etching areas that protrude from a nonmetallic inclusion.[25] Although butterflies can be observed with many types of nonmetallic inclusions, they preferentially form around alumina-type inclusions.[25] This is because alumina inclusions are hard and brittle relative to the martensitic matrix, causing incoherent interfaces and encouraging crack formation which is a prerequisite for butterfly formation.[25] In many instances, cracks can be observed on top of the upper wing and below the lower wing as can be observed in Figure 1.15.

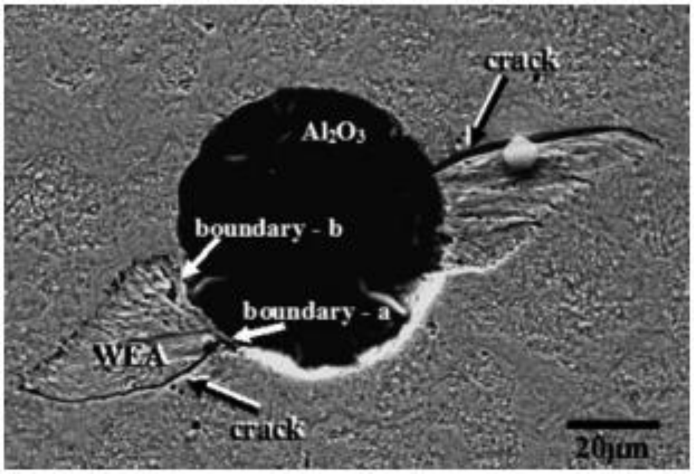

Figure 1.15 Butterfly wings formed around an alumina inclusion with cracks above the upper wing and below the lower wing.[41]

As can be seen in Figure 1.16, the inclusion or center of the butterfly etches dark, while the wings etch white and are angled approximately 45° to the raceway towards the rolling direction.

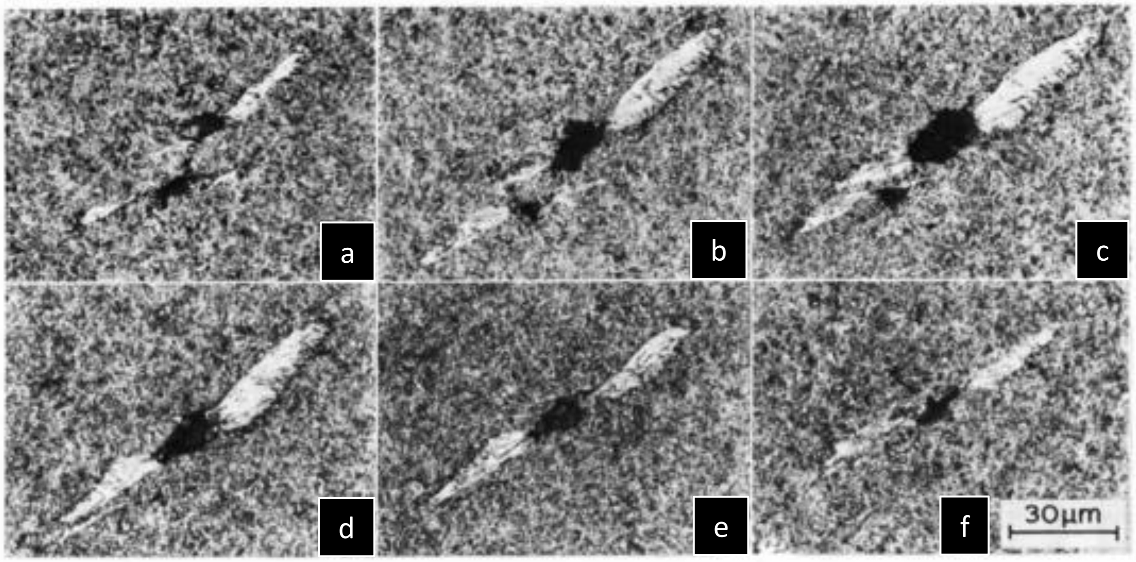

Figure 1.16 Each successive image represents the same butterfly as it is serial sectioned.[42]

Butterflies are assumed to form due to the maximum shear stress that occurs as a result of contact stresses.[25] Butterflies do form at depths much lower than where the maximum shear stress occurs, but the density of butterflies increases in the region of maximum shear stress.[42] The density of butterflies is also proportional to the number of cycles. As the number of cycles increase, the density of butterflies increase.[42]

The microstructural transformation occurs gradually. The martensite matrix first breaks down into ferrite and as the material experiences more stress cycles, the ferrite is refined to have an ultrafine grain size. However, the ferrite grain size varies in relation to location within the butterfly wing with inner ferrite grains closest to the inclusion being approximately 10 times smaller than those located near the edges of the wing.[42] The larger grains are also observed to be relatively dislocation free. The average overall ferrite grain size was 10 nm. The determination of the white etching phase that makes up the butterfly wings to be ferrite was done using transmission electron microscopy (TEM). TEM ring patterns taken from a randomly oriented ferrite sample matched the ring patterns produced from the wing microstructure.[42]

1.7 Main Mechanisms of Formation

There are three main mechanisms of formation thought to be associated with dark etching regions and white etching bands: plastic deformation, stress-induced transformations, and carbon diffusion. The development of microstructural alterations are linked to the magnitude of the shear stresses as well as the number of cycles imparted upon the bearing.[21, 25] The location of maximum shear stress, as shown in Fig. 1.8, occurs some distance below the surface and coincides with the region of microstructural alterations. The minimum shear stress below which microstructural alterations do not occur was determined to be approximately 105 ksi, or 0.72 GPa.[37] Likewise, below a minimum Hertzian pressure of approximately 2.5 GPa, there have been no observations of microstructural alterations.[21] This pressure corresponds to the same value needed to induce plastic deformation in bearing steels leading to the conclusion that plastic deformation is a mechanism of formation for microstructural alterations. Plastic deformation in polycrystalline materials happens via dislocation slip along certain crystallographic planes.[25,43] Over numerously loaded cycles, the consequences of plastic deformation are observed in a fine cell-like dislocation structure that presents itself in the ferritelike phase of WEBs.[25]

During the cyclic stressing, dislocations interrupt the coherence of carbides with the martensite matrix and breakup the carbides.[25] The response of dislocations to cyclic stressing is complex and highly depends on the material microstructure[37], but it is known that dislocation motion contributes to the energy needed for carbon diffusion.[25] One proposed hypothesis related to microstructural alterations states that the original fine carbides present in the martensitic matrix dissolve as the material is cyclically stressed and the carbon diffuses to regions of high dislocation densities.[25] Supporting this is the fact that the binding energy of an interstitial carbon atom adjacent to an edge dislocation is greater than the carbon in carbides.[44] When this happens, the matrix becomes oversaturated with carbon and the carbon reprecipitates out at preferential sites such as grain boundaries.[24] The white etching bands themselves do not contain any carbon atoms which means they had to diffuse from the location where the bands form. The lenticular carbides that form parallel to the 30° bands also support this idea since they are not present before the formation of the bands. Likewise, discontinuous precipitation of carbides has been observed along the slip planes of a 0.47%C steel after undergoing deformation[44] and it has been suggested that carbide dissolution is related to the degree of slip and would therefore cause the orientation of microstructural alterations to be dependent upon the orientation of the martensitic crystals.[25]

Polonsky and Keer[22] offer an explanation for the carbon diffusion. As stated previously, interstitial carbon atoms like to segregate around edge dislocations forming a carbon atmosphere. If a mobile and immobile dislocation meet and annihilate each other, carbon atoms that were segregated around the dislocation go into ordinary solution. The concentration of the carbon atoms in ordinary solution in the area of a developing white etching band is now greater than the carbon concentration in solution in the matrix. Similarly, the concentration of the carbon in a dislocation atmosphere in the band is less than the average concentration of carbon segregated in the form of a dislocation atmosphere in the matrix. The resultant is a driving force for carbon outflow of the white etching band.

Residual stresses are another factor that also impacts microstructural alterations. If a material is cyclically stressed at a load high enough to cause plastic deformation, compressive residual stresses develop in the region of maximum shear stress.[21] A small compressive residual stress actually reduces the max shear stress and does not affect its location, but as the compressive residual stress increases, the maximum shear stress increases and its location shifts toward the surface.[21] Residual stresses also alter the direction of maximum shear stresses which support an angle other than 45° in WEBs to occur.[21] These residual stresses that form during rolling service, residual stresses already present at the onset of testing, and tangential stresses all affect the formation of DERs and WEBs.[32]

1.8 Previous Hardness Investigations

Hardness has been frequently investigated in relation to microstructural alterations, but the majority of experiments have been performed via microindentation. Throughout these experiments, a number of results have been obtained and unless otherwise specified, the material of interest was 52100.

An increase in hardness was observed in the region of maximum shear stress if retained austenite (>10%) was originally present in the microstructure after approximately 10^6 cycles.[29,45] If dark etching regions were present, a decrease in hardness was observed.[46] A continual decrease in hardness occured as the number of cycles increased and DER and WEBs were gradually observed.[21,40] Figure 1.17 illustrates the development of hardness as the number of cycles increase as well as the subsurface regions associated with the DER and 30° and 80° WEBs.[40]

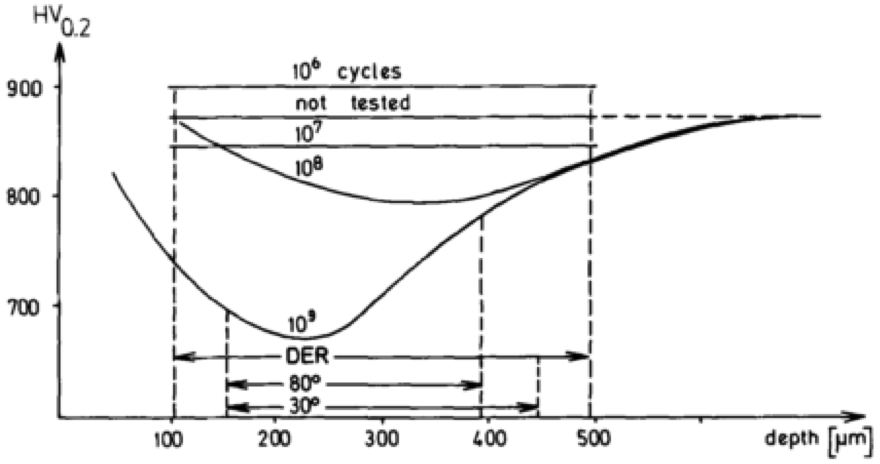

Figure 1.17 The development of hardness as a function of depth below the surface and the number of cycles experienced by the bearing. Likewise, the regions associated with the respective microstructural alterations are labeled.[40]

Hardness values performed inside a butterfly wing were harder than the surrounding matrix.[42,47] Finally, a decrease in hardness was observed in M50 in which WEBs were present.[36] Based on these studies, a decrease in hardness would be expected in the region of microstructural alterations unless retained austenite was present in the material prior to fatigue testing.

1.9 Goal And Approach

In the past, numerous experiments have been performed to better understand microstructural alterations that occur in bearing steels. A common experiment was to use microindentation to measure hardness in and around the region of microstructural transformations. The goal of this thesis was to investigate the development of hardness as a function of depth below the surface as well as its development in multiple regions experiencing varied applied stresses within the Hertzian contact ellipse by using nanoindentation. Nanoindentation allows for a much smaller indent (~1 micron) which in turn decreases the plastic zone associated with the indent and allows indents to be more closely spaced. For this study, the indents were able to be separated by a 10 micron spacing rather than the 40-50 microns needed when employing a Vicker's or Knoop indenter. This allows the experimenter to track a change that is occurring in the material more precisely as well as indent more locally within a microstructural alteration.

CHAPTER 2. EXPERIMENTAL PROCEDURE

2.1 Materials for Testing

For this study, five cylindrical rods of 3/8 inch diameters were used. Four of those rods were M50 steel and one was AISI 52100 steel. The exact heat treatment for the M50 rods are unknown. They were found in a mechanical testing laboratory and labeled as M50. They are believed to have been ordered by a previous researcher to be used in his/her study but were left untested. The typical heat treatment, therefore, will be discussed for M50 steel instead, and the known heat treatment details will be given for the 52100 steel.

A previous student from the same current research group in 2006 utilized the 3 ball-on-rod test rigs and used M50 and BG42 cylindrical bars for his study.[48] The heat treatment parameters for his bars were as follows:

"Both types of rods were heat treated. The BG42 rods were preheated to about 1450 to 1550°F and then were austenitized at approximately 2050°F. Next, the rods were oil quenched to room temperature. They were stress relieved at 300°F for an hour and air cooled. The rods were refrigerated at -100°F until they were equalized and then warmed to room temperature. They were quadruple tempered at 975°F and were cooled to room temperature between each temper. The M50 rods were prepared in a similar fashion."

This heat treat sequence and corresponding temperatures match well with what literature states about the heat treatment process of M50 steel.[49]

The AISI 52100 cylindrical rod was bought from McMaster-Carr in the annealed state. It was then heat treated by heating it to 1550°F, soaking it for 10 minutes and then quenching it in oil. It was then tempered at 400°F for approximately 15 minutes. This produced a hardness of 60-65 HRC. Finally, to prepare the sample to be run in a 3 ball-on-rod test rig, the sample was surface ground to a surface roughness of 0.3 microns.

2.2 Three Ball-on-Rod Testing

A Federal-Mogul three ball-on-rod rolling contact fatigue tester was used in this study to produce rolling contact fatigue in cylindrical bars and is shown in Figure 2.1. The information in this section relied heavily upon a paper by D. Glover in which he described this machine.[50]

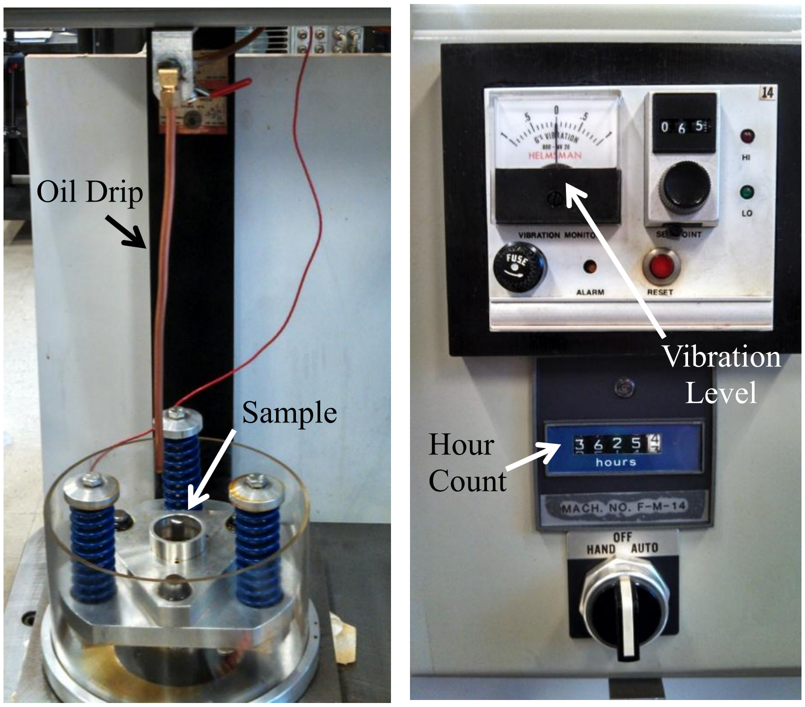

Figure 2.1 A Federal-Mogul RCF tester. The left image shows where the sample is loaded with an oil drip and the right image shows the machine controls and the hour count associated with the motor time.

The cylindrical specimens are 9.525 millimeters in diameter and the balls are 12.7 millimeters in diameter. As the name implies, there are three balls used as points of contact in this machine and are housed and separated by a cage made of bronze that can be seen in Figure 2.2.

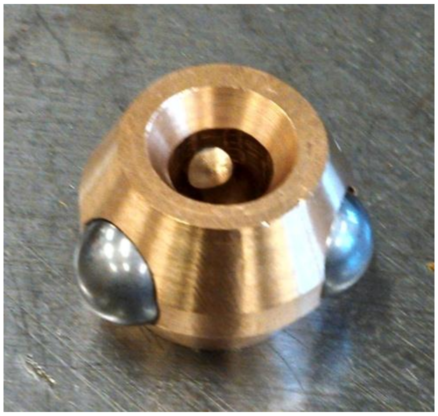

Figure 2.2 A bronze cage is used to separate and keep the balls in place during a rolling contact fatigue test.

To impart a force on the balls, a spring-loaded three-plate contraption is used. The three springs that can be observed in Figure 2.1 are preloaded with hanging weights so the force of each spring equals:

$$F_S = \frac{W}{3} \tag{2.1}$$

where F_s is the force of the spring and W is the hanging weight added to compress the springs. The springs are housed in the center plate that connects to the upper and lower plates. Those in turn house the standard bearing cups that actually transfer the force from the springs to the balls. Figure 2.3 illustrates how the forces from the springs are transferred to the cylindrical specimen.

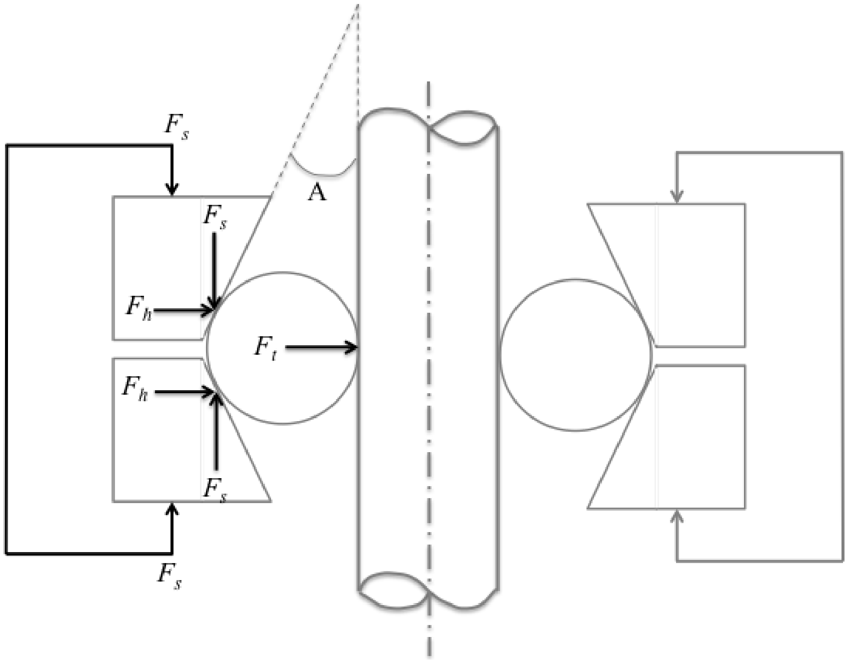

Figure 2.3 A schematic illustrating the forces acting upon the cups which in turn is transferred to the ball and finally the cylindrical rod (adapted from Ref. 48).

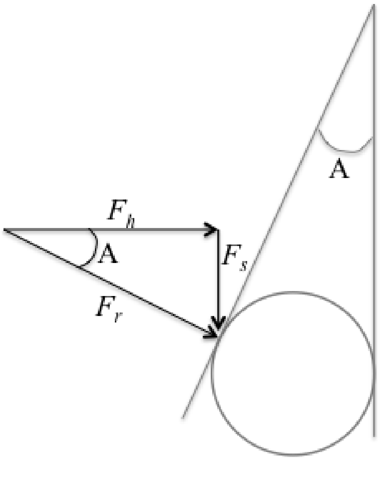

Figure 2.4 Angle A associated with the tapered bearing cup is used to determine the horizontal force imparted on the balls.

In Figures 2.3 and 2.4, angle A is the cup angle and is 25.083° for this system. F_s, as defined earlier, is the force imparted on the cups by the springs, F_h is the horizontal force acting on the ball, and F_r is the resultant force that acts perpendicular to the point of contact of the ball. Using the geometry given in Figure 2.4, the horizontal force acting on the ball can be calculated by using the following equation:

$$F_h = \frac{F_S}{tan\, A} \tag{2.2}$$

Because the ball is compressed by a top and bottom cup, there are two horizontal forces acting on the ball and the force transferred to the cylindrical rod is the sum of the horizontal forces as follows:

$$F_t = F_h + F_h = 2F_h \tag{2.3}$$

where F_t is the total force acting horizontally on the cylindrical rod. If equation 2.2 is substituted into equation 2.3, an equation relating the force acting on the cylindrical rod to the force of the spring can be written as:

$$F_t = \frac{2F_s}{tan\, 25.083\,°} \tag{14}$$

If a known Hertzian pressure is desired, this equation can be equated to equation 1.9 in section 1.4 of this document to solve for the desired force imparted by each spring within the system:

$$F_S = \frac{{P_0}^3 (\pi c_a c_b)^3 m^2\, tan\, 25.083}{2 * 1.5^3 n^2} \tag{2.5}$$

Variables are predefined in section 1.4 of this document.

2.2.1 Loading Parameters Used in Three Ball-on-Rod Test

As previously stated, four M50 cylindrical bars and one 52100 cylindrical bar were tested in the three ball-on-rod tester to 10^8 cycles. The 52100 cylindrical bar was reused a second time to impart a lower load in a different location. Two of the M50 rods as well as the first location on the 52100 rod were loaded at 4.5 GPa. The final two rods of M50 were loaded at 5.0 GPa and the second location on the 52100 rod was loaded at 4.0 GPa. For each set of M50 rods loaded at 4.5 and 5.0 GPa, one was lubricated during the test at a rate of 8-10 drops per minute and the other was tested without lubrication. Both tests performed on the 52100 sample were lubricated. Federal-Mogul three ball-on-rod test rigs are typically equipped with an accelerometer that measures the vibration levels as the test is performed. The accelerometer is set so that when the vibration level reaches a designated value associated with failure, the machine automatically shuts off. For this study, the accelerometer was not used as the number of cycles was an important control parameter and was desired to be uniform in all specimens. Failure, as measured by the accelerometer, would have automatically shut off the machine before it reached the desired 10^8 cycles.

2.3 Wear Track Measurements

2.3.1 M50 Steel Tested at a Load of 4.5 GPa for 10^8 Cycles

After the M50 samples tested at a load of 4.5 GPa completed 10^8 cycles in a RCF test, the wear tracks were well defined in both the lubricated and unlubricated specimen and could be observed by the eye. Spalling was observed on the wear track but did not encompass the entire circumference of the sample. To measure the width of the wear track, the specimen was placed under a stereoscope to obtain a magnified image. A scale bar used specifically for optical and stereograph microscopy was also imaged at the same magnification to ensure the scale bar within the program was correctly calibrated. The wear track of the 4.5 GPa loaded sample that was lubricated was measured to be 570 µm. The wear track of the 4.5 GPa loaded unlubricated sample was not measured prior to polishing. This sample was used in order to determine if the samples tested did indeed contain desirable microstructural alterations before proceeding forward with an experimental plan.

2.3.2 M50 Steel Tested at a Load of 5.0 GPa for 10^8 Cycles

Unlike the wear tracks of the M50 steel rods tested at a load of 4.5 GPa for 10^8 cycles, the wear tracks in these specimens were convoluted due to a significant amount of spalling around the entire circumference as can be seen in Figure 2.5.

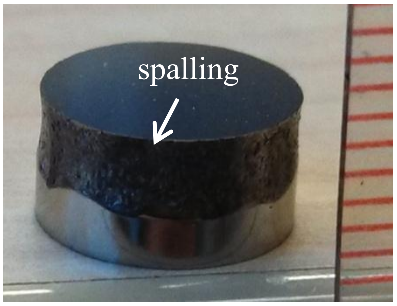

Figure 2.5 A representative image of the spalling in the M50 samples loaded to 5.0 GPa. Each red line in the image is a millimeter. This can be compared to a representative wear track of a sampled loaded to 4.5 GPa in Figure 2.6.

Due to the lack of distinct definition, the wear track was defined according to the calculated values for the ellipse major axis values of *a*. In the case of a ball-on-cylinder geometry with a load of 5.0 GPa, *a* was determined to be 322 micrometers, and the entire width of the wear track, *2a*, was 643 micrometers.

The damage caused by spalling was significantly larger than this value, and therefore the center of the spalled region was assumed to be the center of the wear track. The edges of the spalled region were extremely undulating so ten random locations that spanned the entire circumference of the rod were chosen to measure the width of the spalled region. The ten values were then averaged and from this value, the center of the spalled region was determined to be located at half the average value. The wear track was then designated as spanning 322 micrometers in either direction from the center.

2.3.3 52100 Steel Tested at a Load of 4.0/4.5 GPa for 10^8 Cycles

The 52100 rod was tested in two separate locations and the wear track was determined in the same manner as the M50 rods tested at a load of 4.5 GPa. An image of the 4.5 GPa loaded sample wear track can be seen in Figure 2.6 as outlined by the white lines. From this image, the wear track was measured to be 620 ± 10 μm.

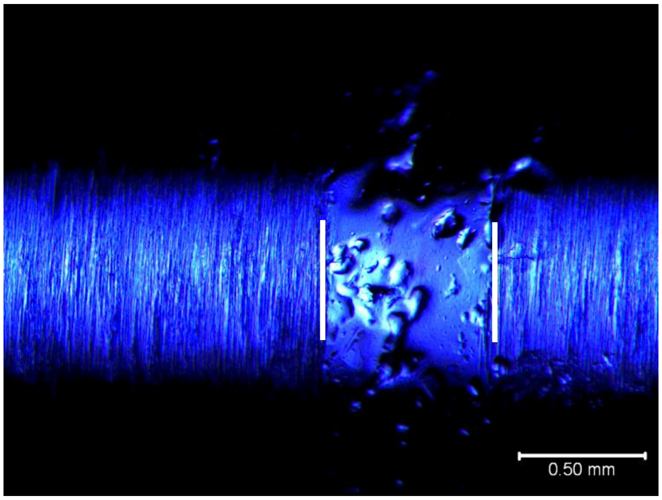

Figure 2.6 The wear track of the 52100 cylindrical rod tested in rolling contact fatigue.

2.4 Experimental Design

As explained in section 1.4.3, the Hertzian pressure changes as a function of location within the contact ellipse created by the contact between the ball and the rod. To identify the effects of differing pressures on the microstructure beneath the surface, the following experimental set-up utilizing nanoindentation was performed.

The measured wear track of each sample was assumed to be equivalent to $2a$. To probe regions of differing experienced stresses, three locations along the wear track were chosen. These locations represented essentially no stress, medium stress, and maximum stress and were designated as Regions 1, 2, and 3, respectively. The physical locations of these regions are shown in Figure 2.7.

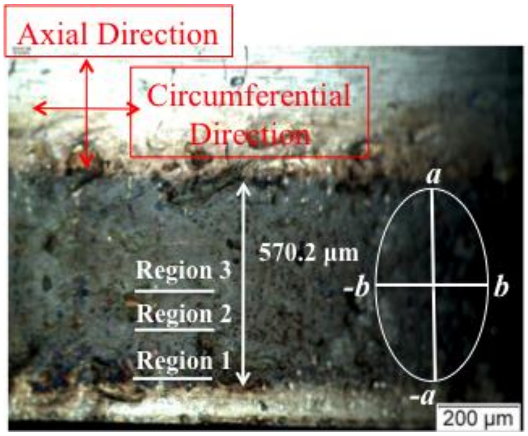

Figure 2.7 Image of the 4.5 GPa/10^8 cycles lubricated M50 wear track designating different locations in which indentation was performed as Regions 1, 2, and 3.

Figure 2.8 more clearly depicts the stresses experienced below the surface in these different regions. Region 3 experienced the largest shear stress below the surface because the largest Hertzian pressure occurs at the center of contact between the ball and rod.

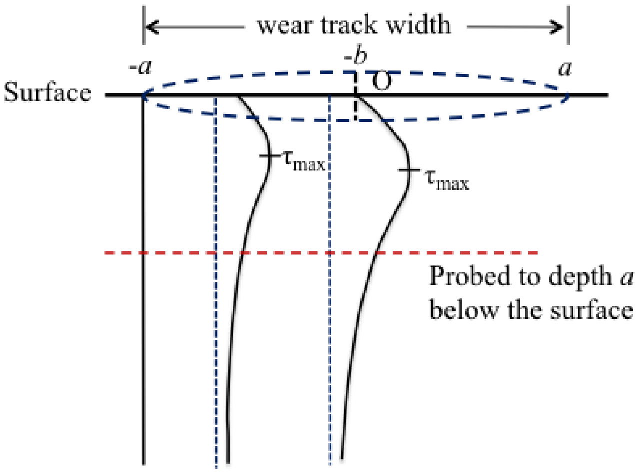

Figure 2.8 The approximate shear stress profiles associated with the differing Hertzian pressures in regions 1, 2, and 3 (R1, R2, R3, respectively) within the contact ellipse.

As one moves further from the center of contact toward ±*a*, the Hertzian pressure and the maximum shear stress below the surface decreases until both are zero at ±*a*.

As previously mentioned, nanoindentation was used to investigate hardness within the material. Specifically, hardness versus depth was of interest to track whether or not it was possible to observe changes within the microstructure in the region of maximum shear stress. The following sections outline the sample preparation used for nanoindentation in this experiment as well as the different nanoindentation techniques employed.

2.5 Sample Preparation

The following sections will outline the procedure used to prepare the sample for nanoindentation. One important consideration in sample preparation for nanoindentation is the flatness of the sample. This requires not only the surface of interest to be flat, but it also requires the back surface to be parallel and flat to get the most accurate results.

2.5.1 Cutting and Surface Grinding

The first step was to remove the region of interest from the rest of the cylindrical bar. To do this, the samples were clamped in place by a vice and then cut using an abrasive saw with a silicon carbide blade.

The first cut made was approximately 1-2 mm away from the wear track. From this location, the material would be polished off and into the wear track to regions of interest. After cutting with this saw, there was a small amount of material that wasn’t flat with the rest of the surface as the blade reached the end of the sample. To flatten that portion to the rest of the surface, a belt grinder of 320 SiC grit was used. Because there was still a significant amount of material to be polished off before reaching the edge of the wear track, and to ensure the surface of interest was flat, a surface grinder was used.

In the case of steel specimens, an aluminum oxide wheel was used to grind the material off. The first step was to clean the wheel using a dressing tool with an industrial grade diamond tip.

The dressing tool was mounted on the stage and the wheel was slowly lowered until it was barely touching the tip. The wheel would be passed across the tip to remove surface layers of the wheel. After each pass, the wheel would be lowered approximately 2-5 μm and passed over the tip again. This was done at least three times to remove any surface material left by the previous sample on the wheel. A good visual check was to look at the wheel itself. If the wheel was completely white, it was appropriate to proceed.

After cleaning the wheel, the cylindrical specimen was loaded in a vice that is shown in Figure 2.9. The specimen is loaded so that the surface of interest is approximately a centimeter above the top surface of the vice. The sample surface is then colored over by a sharpie marker. When the sharpie marks have completely disappeared from the surface while it is being ground, the surface is flat.

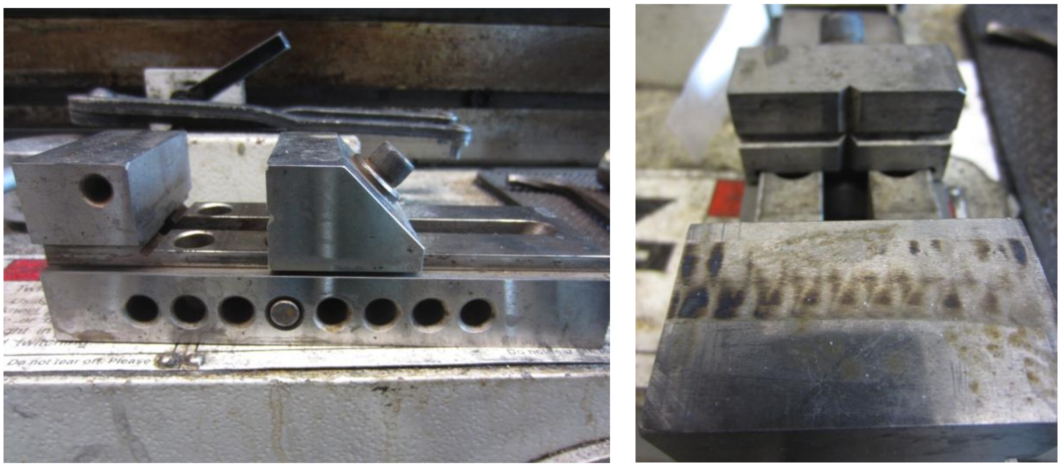

Figure 2.9 The vice that was used to hold the cylindrical bar while surface grinding. The notch in the right image helps assure the sample is correctly loaded and perpendicular to the wheel.

When the sample is loaded, the vice is placed on the surface grinding stage and a magnetic chuck is turned on to hold the vice in place. The sample is then placed directly below the center of the wheel. A piece of paper is held over the sample surface as the wheel is slowly lowered toward the sample. When the wheel kicks out the paper, it is very close to reaching the sample surface. The wheel can then be lowered even more slowly until the sample surface is reached and it starts to remove material. At this point, the sample is passed underneath the wheel while continually lowering the wheel in between passes until the desired amount of material is polished off. Coolant was periodically applied to keep the surface from overheating.

At this point, the surface of interest was flat, but another portion of the cylindrical bar needed to be removed in order to obtain a sample height on the order of a centimeter. The sample was again loaded in the abrasive saw machine and a cut was made on the opposite side of the wear track to reach the desired sample thickness.

A similar procedure was used to flatten this side of the sample except it was mounted differently to perform surface grinding. Because it was undesirable to clamp the area of interest (wear track) in the vice, the surface of interest instead was glued to a flat surface of a puck of pressed bakelite using crystalbond. The bakelite puck was clamped in the vice instead with the sample surface above the vice surface and ready to be polished flat.

After the second surface was polished flat, the sample was removed from the puck by heating the crystalbond and then soaked in acetone to dissolve any residual crystal bond stuck to the sample itself. The sample was then placed under a stereoscope to observe how much material still needed to be polished off to reach the edge of the wear track. After a magnified image was taken and the amount of material to be polished off determined, the sample was ready to be mounted.

2.5.2 Mounting

To make polishing the sample easier and more efficient, it was mounted in a transparent thermoplastic using a LECO mounting press. It was desirable to have a transparent mount so the wear track could be observed at all times within the mount. Figure 2.8b shows the mounting parameters needed to set the thermoplastic. The mounting press was set at a pressure of 4200 psi, and was heated to 320°F at which point it was held for 10 minutes and 30 seconds and then allowed to cool in air to 180°F.

After the sample was mounted, the top and bottom edges of the puck were chamfered. This helps with fluid running under the puck while polishing and makes the puck more comfortable to hold. A micrometer was then used to measure the thickness of the puck. In order to attempt measuring the thickness in the same location, a Dremel engraver was used to outline the arm of the micrometer on the puck.

2.5.3 Polishing

Grinding and polishing was manually performed using a series of silicon carbide abrasive wheels, diamond paste, and alumina. Each specimen underwent the following steps:

1. The samples first went through a series of grinding wheels with progressively finer grits of silicon carbide. The sample started on 320 grit, then moved to 400, and finally 600 grit. In between each of these wheels, the sample was rinsed with water and dried with compressed air. At each step, all the scratches from that respective wheel needed to have been in the same direction and the scratches from the previous wheel needed to have been gone. The surface was also checked to make sure no facets were present.

2. The samples were then subject to diamond polishing on nylon cloth using particulates of 6 μm and 3 μm in size and oil as the medium. Similarly, the samples were polished until the previous scratches were gone, however, the scratches left by these steps were in all directions. After each diamond step, the sample was rinsed and washed with Ajax^{TM} dishwashing soap and then dried with compressed air before continuing.
3. The final step was to polish the samples on a nap cloth with 0.05 alumina slurry. The sample was polished until a mirror finish on the surface was observed and the majority, if not all, scratches were no longer visible. The sample was then rinsed and washed with water and Ajax^{TM} dishwashing soap followed by drying with compressed air.

There was no set time spent on each wheel or step. It was dependent on the flatness of the surface and the appearance of the scratches. For these samples, however, there was typically a set amount of material that needed to be polished off by the time the sample reached a mirror finish. Because of this, the puck thickness was measured using the micrometer in approximately the same location that was outlined using the engraver tool after each abrasive wheel. The majority of material removal was done on 320 grit before moving on to successive steps. After the abrasive wheels were completed, there was minimal material removal from the diamond and alumina wheels (<5 microns).

The next step was to break the sample out of the mount to prepare for nanoindentation testing. To do this, the mount was clamped in a vice and a hand saw was used to make cuts into the thermoplastic mount which allowed the sample to be easily popped out. Because the surface accumulated some debris from the mount during this process, the sample was touched up using the 0.05 alumina slurry. A rinse and wash followed as outlined before but the Ajax soap was lightly swabbed on the surface using a Q-tip for this final step, and again the sample was dried with compressed air. Finally, the sample surface was etched in 2% Nital for 15-30 seconds to reveal the microstructure.

2.5.4 Optical Microscopy

The surface was then checked under an optical microscope for scratches. A rule of thumb was if scratches were not observed under a 10x objective lens, the surface was good enough to perform nanoindentation. However, the higher the objective lens while still not observing scratches, the better.

At certain locations within the wear track, microstructural alterations were observed. If this was the case, multiple alterations would be imaged using the optical microscope with the correct scale bar added to the image. As stated earlier, a known calibration scale bar was imaged at the different magnifications and the correct scaling was provided for each. The original microstructure was also imaged so as to compare it to the microstructure containing alterations.

2.6 Nanoindentation

2.6.1 Calibration

After using optical microscopy to determine areas of interest on the surface, nanoindentation was ready to be performed. Before taking indents using the Hysitron TI-950 nanoindenter, a standard z-axis calibration was performed. This was performed to ensure the transducer was performing its function correctly. To do this, an air calibration indent was performed in which the tip was loaded to approximately 1441 μN and then unloaded. An Electrostatic Force (ESF) vs. displacement graph is produced in which a red line from the test should closely overlap a linearly fitted blue line. A root-mean-square-error (RMSE) value is also output and should be less than $1x10^{-5}$. If both of these conditions are met, the z-axis calibration passed and the transducer is functioning correctly.

The next step was to check the accuracy of the current area function. The area function of interest is derived by taking 100 indents in a fused quartz sample at incrementally increasing loads starting at approximately 500 μN and increasing to 12,500 μN. The contact area for each indent vs. the depth of that indent is plotted and the data is fitted using the area equation for an ideal Berkovich indenter. It is necessary to periodically update the area function because the Berkovich tip becomes blunted over time with use.

To ensure the most recent area function was fitting indentation data correctly, the fused quartz sample was indented once to check the reduced modulus and hardness values. After an indent was taken, the load-displacement curve generated was fit using the current area function. If the hardness value was 9.25 GPa ± 10% and the reduced modulus was 69.6 GPa ± 5%, the current area function could be used to fit other data. Area functions in general have an indentation depth range in which they remain accurate. The majority of indents taken in this study probed 150-200 nm into the surface which fell well within the 40nm-400nm limits of the area function used.

Indents made on the M50 samples were performed using two different methods. The first was an automated method in which an array of indents was set up to continuously run and the second method was using the scanning probe microscopy (SPM) function and clicking specifically in the areas that were desired to be indented by looking at an SPM image. Both methods will be discussed separately in the following sections.

2.6.2 Automated Indentation

Automated indentation was used when hardness vs. depth values were desired. An array of three columns by 30 rows was used in which case the first row was indented approximately 20 microns from the edge of the surface. Each row was spaced by 10 microns and each column was spaced by 20 microns as can be seen in Figure 2.10.

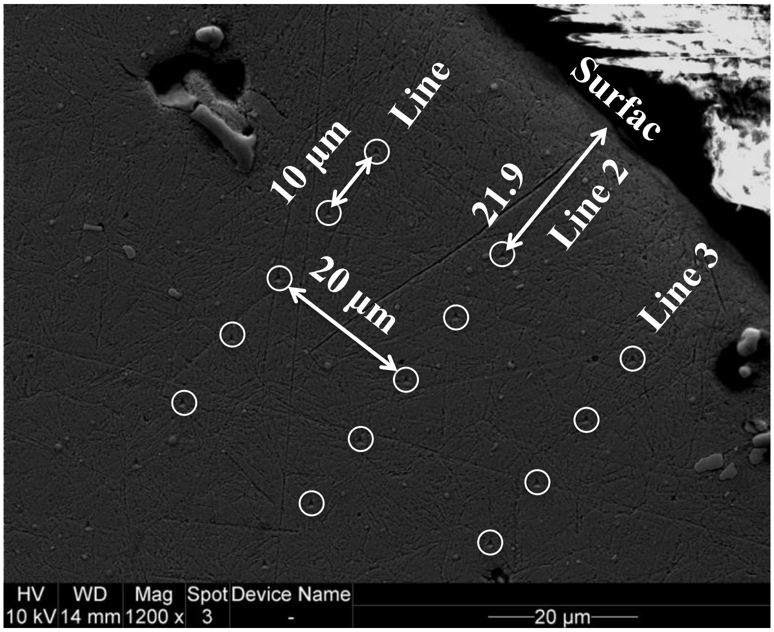

Figure 2.10 SEM image from one of the samples showing the spacing and set-up of a typical indentation array.

The location on the sample where this method would start was designated and the indents were taken continuously until completion, which typically took approximately 4.5 hours.

After all the indents were taken, the load-displacement curves were analyzed by fitting the upper 30-90% of the unloading curve. A multiple curve analysis was produced in which all the hardness, reduced modulus, and other values associated with the load-displacement curves were output into an excel spread sheet for all 90 indents that were just taken. This data could then be used for further analysis later.

2.6.3 Indentation Using Scanning Probe Microscopy

The second method employed the indents via imaging technique. The indenter tip would scan over the surface at a rate designated by the user (1-2 Hz) and produce forward/reverse topography images and forward/reverse gradient images. The topography images were produced by measuring the height of the indenter as it scanned the surface, and the gradient images were produced by measuring the slope the indenter was undergoing instantaneously.

This method was used specifically when doing indentation in and around microstructural alterations. The scanning window was designated by the user and was typically no larger than 50 microns but varied based on the size of the alteration. When using the SPM image, a "click script" was used to perform the indents. After the image finished scanning, the user could click anywhere within the window and wherever the mouse clicked, a dot was placed on the image with a number to indicate the location of desired indents. The designated load was then set and the test was run until all the indents had been completed. An image of the scanning window was taken after the completion of the test and the newly performed indents were observed. A small amount of drift that typically occurred during the test caused a slight offset of the originally desired location of the indents at times.

2.6.4 Determination of Hardness and Elastic Modulus from Nanoindentation Data

The Young's modulus and hardness of a material can be readily calculated from data taken via nanoindentation. The raw output data is given as the load applied versus the displacement, or depth in which the indenter probes into the material. A typical load-displacement curve is shown in Figure 2.11.[51]

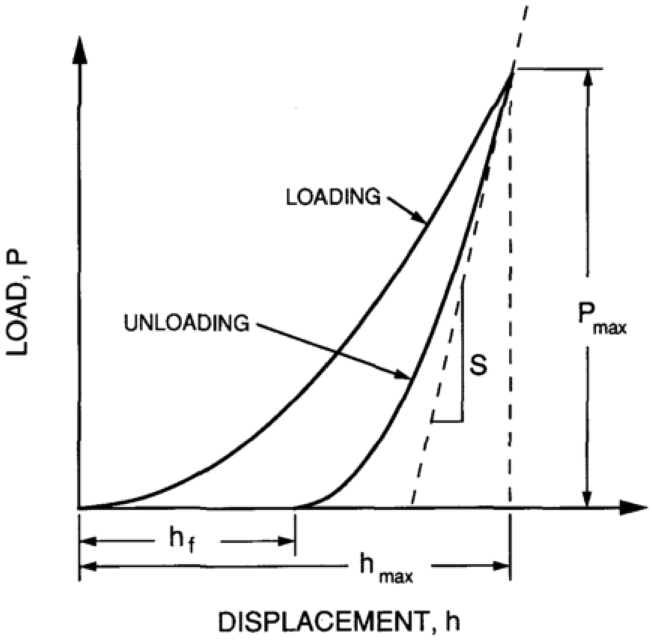

Figure 2.11 Upper portion of the unloading curve is fitted to solve for stiffness, S.

From this curve, the upper portion of the unloading curve is fitted and the stiffness of the material is equal to the change in load over the change in displacement:

$$S = \frac{dP}{dh} \tag{2.6}$$

The reduced modulus can be solved for by using the following relation:

$$S = \frac{dP}{dh} = \frac{2}{\sqrt{\pi}} E_r \sqrt{A} \tag{2.7}$$

where E_r is the reduced modulus and A is the contact area. To solve for A, the contact depth, h_c, must be known and is defined by:

$$h_c = h_{max} - h_s \tag{2.8}$$

where h_{max} is the displacement at maximum applied load and h_s is the displacement of the surface at the edge of contact as displayed in Figure 2.12.

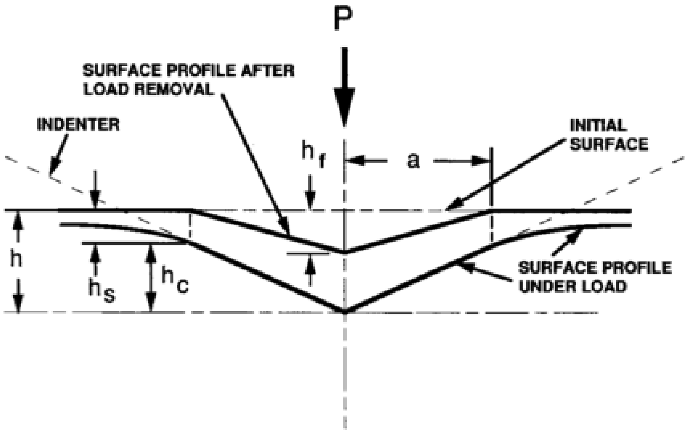

Figure 2.12 A cross sectional view of the geometry of the indenter-material interface at maximum load and after the load has been removed.[51]

The parameter h_{max} is directly taken from the raw data output, but h_s is dependent on the indenter geometry, and for a conical indenter is defined as:

$$h_s = \epsilon \frac{P_{max}}{S} \tag{2.9}$$

where ε is a geometric constant having a value of 0.72 and P_{max} is the maximum load applied to the surface. Even though the indenter of interest is a triangular pyramidal Berkovich indenter, it can be assumed to function as a conical indenter. Since h_s and h_{max} are known, the contact depth can be calculated and in turn, the contact area associated with a perfect Berkovich indenter:

$$A_c = 24.5{h_c}^2 \tag{2.10}$$

At this point, the reduced modulus can be evaluated by rearranging equation 2.7 to be:

$$E_r = \frac{\sqrt{\pi}}{2}\frac{S}{\sqrt{A_c}} \tag{2.11}$$

The reduced modulus is a function of the material's and indenter's Poisson's ratios and Young's moduli and is given in the following equation:

$$\frac{1}{E_r} = \frac{(1-\nu^2)}{E} + \frac{(1-{\nu_i}^2)}{E_i} \tag{2.12}$$

where E and ν are the Young's modulus and Poisson's ratio of the material indented and E_i *and* ν_i are the Young's modulus and Poisson's ratio for the indenter, which in the case of the Berkovich indenter is made of diamond. Since those values are known for diamond (E_i=1141 GPa and ν_i=0.07), the equation can be rearranged and solved for E assuming the Poisson's ratio of the material being indented is known.

Hardness is calculated using the following equation:

$$H = \frac{P_{max}}{A_c} \tag{2.13}$$

Where H is hardness, P_{max} is the maximum load applied, and A_c is the contact area as defined in equation 2.10. Hardness was of primary interest in this study and will be discussed in length in the following chapter.

2.7 Scanning Electron Microscopy

A scanning electron microscope was rarely used in this study, but it was utilized to image indents at one point as well as to perform electron dispersive Spectroscopy (EDS) on a feature contained in the microstructure. The microscope used was a FEI Philips XL-40. EDS can be used to determine what elements are in the material and the relative proportion of those elements. It does this by collecting x-rays produced from the interaction of the electron beam and the material being investigated. It counts the x-rays collected with their respective energy levels, and because different elements produce characteristic x-rays, the energies can be connected to the respective element. The parameters used to produce the EDS spectrum were a 15 KV beam, a working distance of 10.0 mm, a dead time of 20-25% and counts per second of approximately 1000.

CHAPTER 3. RESULTS AND DISCUSSION

The following sections present and discuss the findings of this study for all cylindrical bars that were tested. Table 3.1 is an overview of observations made from each sample, as well as calculated *a* and *b* values for the Hertzian contact ellipse related to each cylindrical rod. Table 3.2 then presents the calculated maximum Hertzian pressure acting in Regions 1, 2, and 3 during rolling contact.

.

Table 3.1 Overview of observations in all the test specimens.

Sample	**Spalling**	**Width of Wear Track (~2*a*)**	**Cal. (a) µm**	**Cal. (b) µm**	**WEBs Observed**	**Butterflies Observed**
4.5 GPa lubricated M50	+	570 µm	290	160	Possibly	Yes
4.5 GPa unlubricated M50	+	Unknown	290	160	Maybe	Yes
5.0 GPa lubricated M50	++	Excessive Spalling	322	177	No	No
5.0 GPa unlubricated M50	++	Excessive Spalling	322	177	No	No
4.5 GPa 52100 lubricated	+	620 µm	277	152	No	No
4.0 GPa 52100 lubricated	-	440 µm	246	136	No	No

+	Spalling occurs but does not encompass the entire circumference of the cylindrical rod and a wear track is identifiable
++	Severe spalling occurs encompassing the entire circumference and the original wear track is unidentifiable
-	No spalling observed

Table 3.2 Calculated maximum Hertzian pressures for the different investigated regions.

Location	**4.5 GPa Lub/Unlub M50**	**5.0 GPa Lub/Unlub M50**	**4.5 GPa 52100**	**4.0 GPa 52100**
Region 1	0 GPa	0 GPa	0 GPa	0 GPa
Region 2	3.9 GPa	4.3 GPa	3.9 GPa	3.5 GPa
Region 3	4.5 GPa	5.0 GPa	4.5 GPa	4.0 GPa

3.1 Starting Microstructure

3.1.1 M50 Steel

An image of the starting microstructure of M50 steel is shown in Figure 3.1. It is composed of plate martensite with fine, homogeneously distributed spherical carbides as well as other large irregularly shaped carbides. Electron dispersive spectroscopy (EDS) was performed on the large, shiny white regions that are observed in Figure 3.1 and the results are given in Figure 3.2.

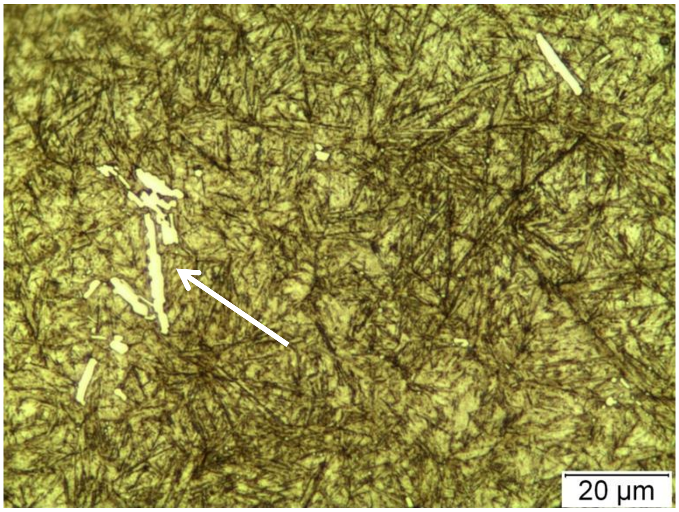

Figure 3.1 Pristine microstructure as observed in M50 steel that has not undergone rolling contact fatigue.

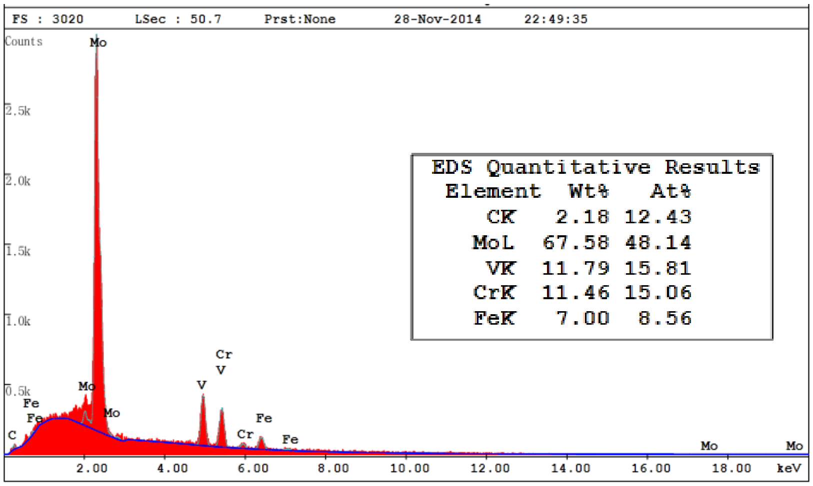

EDS Quantitative Results

Element	Wt%	At%
CK	2.18	12.43
MoL	67.58	48.14
VK	11.79	15.81
CrK	11.46	15.06
FeK	7.00	8.56

Figure 3.2 EDS spectrum showing the presence of molybdenum, vanadium, and chromium in the large white features of Figure 3.1.

The results show there is a high Mo content as well as some vanadium and chromium. Based on a quantitative analysis of the elements present and prior literature referencing M50 steel,[52,53,54] the features were determined to be M_6C carbides where M represents the carbide forming elements which in this case are Mo, Cr, and V.

Another aspect of the microstructure that was investigated was prior austenite grain size. It was of interest in this study for two reasons: (1) as a check to confirm the steel was processed correctly and (2) to confirm whether or not nanoindentation arrays were done in a single grain or over several prior austenite grains.

When analyzing the nanoindentation data, there was noticeable scatter in the M50 steel specimen data. In the interest of confirming or disproving whether or not indenting in different prior austenite grains affected the hardness significantly, the sample was etched to reveal the prior austenite grains. Historically, prior austenite grain size has been difficult to observe in martensitic steels because there is not a universal etchant that will reveal this structure. The most successful etchant is considered to be saturated aqueous picric acid plus a wetting agent (sodium tridecylbenzene sulfonate or sodium dodecylbenzene sulfonate).[55] In this particular study, prior austenite grain size was observed by etching in 2% Nital. All the specimens were etched in Nital to observe the microstructure and only one sample revealed prior austenite grains. It is unknown why it worked on one particular sample, but Figure 3.3 shows an optical micrograph of the prior austenite grains observed in the pristine microstructure of M50 steel.

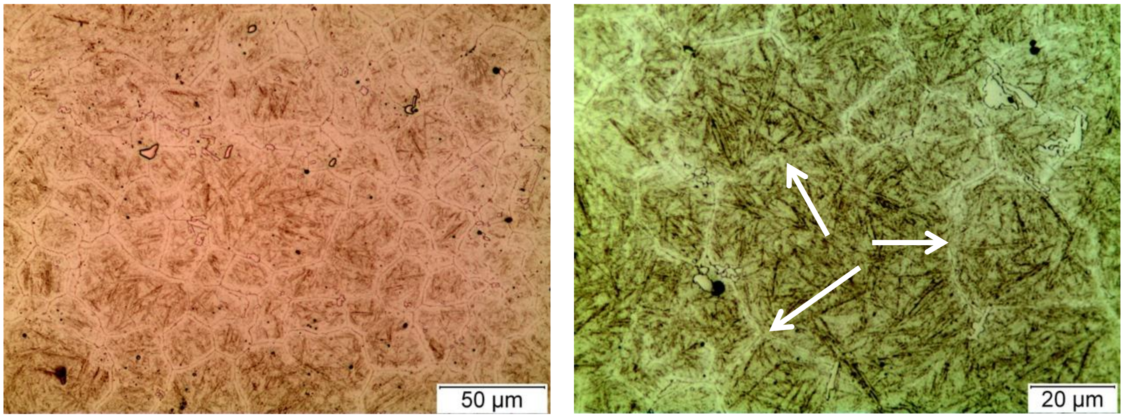

Figure 3.3 (a) Prior austenite grain size in M50 Steel etched with 2% Nital at 500x. (b) PAGs in the same sample as (a) at 1000x. The white arrows point to the prior austenite grain boundaries.

The grain size was calculated by using the line intercept method as outlined in ASTM standard E112-13. The intercept method was employed on a micrograph at 100x (10x objective) magnification. Seven lines of equal length were drawn randomly on the image and the intersections of the grain boundaries were counted. The total length of the lines added together was divided by the number of total intercepts and the grain size was determined to be approximately 24 microns. This corresponds to an ASTM grain size of 8. Having this knowledge gives a better understanding of how many different grains are being probed in a given indentation test and the general size of the grains.

3.1.2 52100 Steel

The starting microstructure of 52100 steel is tempered martensite with finely distributed (Fe,Cr)$_3$C carbides as can be seen in Figure 3.4. Scanning electron microscopy was also used to observe the microstructure at a higher magnification as can be seen in Figure 3.5.

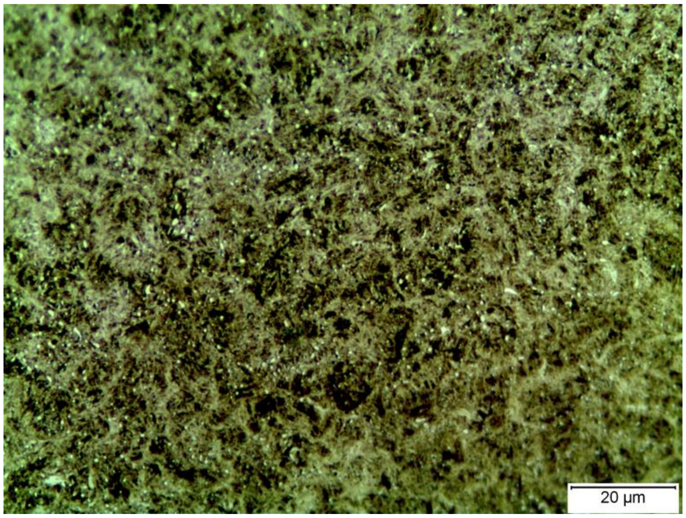

Figure 3.4 Starting microstructure for 52100 steel showing tempered martensite and finely distributed carbides at 1000x.

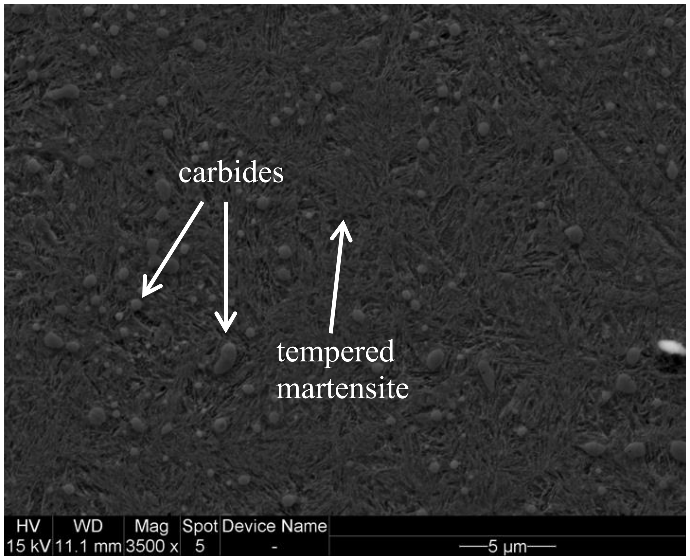

Figure 3.5 SEM imaged of 52100 microstructure after etching in 2% Nital showing the tempered martensite and spherical carbides present.

3.2 Characterization of Microstructural Alterations

A number of techniques were used to characterize the microstructure of the different cylindrical specimens. Included were optical microscopy, scanning electron microscopy, and nanoindentation. In the following sections, the results respective of each M50 and 52100 cylindrical rods relative to the aforementioned characterization techniques will be presented in detail.

3.2.1 Lubricated/Unlubricated 4.5 GPa Loaded M50 to 108 Cycles (Microscopy)

In the 4.5 GPa loaded lubricated M50 sample tested to 10^8 cycles, regions 1, 2, and 3 were all examined using optical microscopy to determine the presence of any microstructural alterations. Figures 3.6-3.7 show the microstructure as etched in 2% nital for regions 2, and 3. There was no image taken in Region 1 as no alterations were present. Likewise, the 4.5 GPa loaded unlubricated M50 sample tested to 10^8 cycles was investigated for microstructural alterations, but there is no designation for location within the wear track. Figure 3.8 shows a representative micrograph of the alterations observed and compares it with the 4.5 GPa lubricated sample.

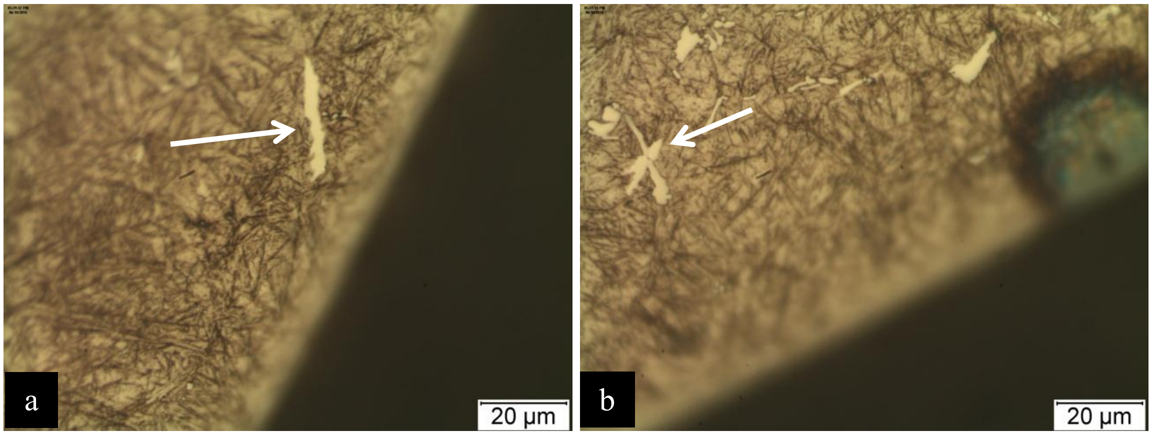

Figure 3.6 Both images are representative of the matrix microstructure as well as revealing butterflies (pointed out by the white arrows) that are present in region 2 of the 4.5 GPa/10^8 cycles lubricated M50 sample.

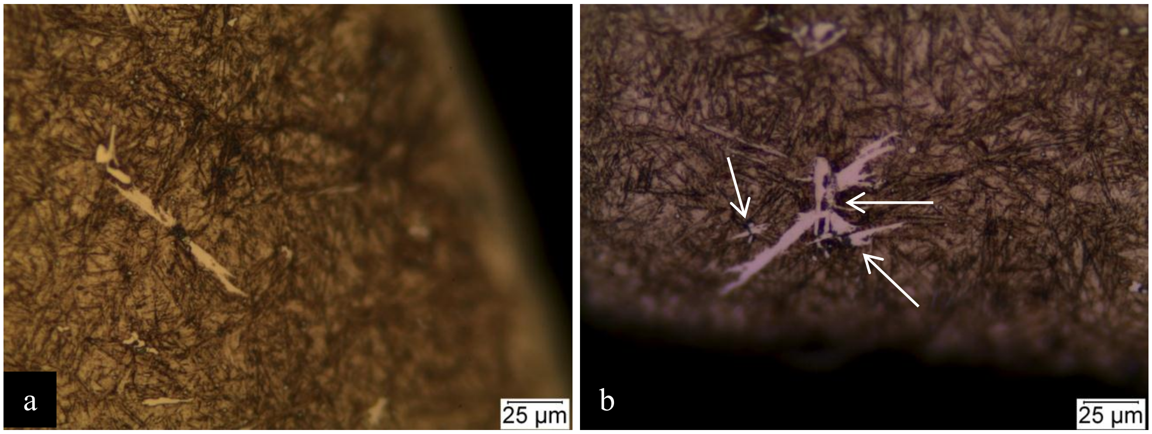

Figure 3.7 Images (a) and (b) show different types of butterflies observed in region 3 of the 4.5/10^8 cycles lubricated M50 sample. Figure 3.8a is a good representation of a butterfly centered on a dark etching inclusion and Figure 3.8b shows large butterfly wings emanating from a M_6C carbide as well as two smaller ones centered on dark etching inclusions.

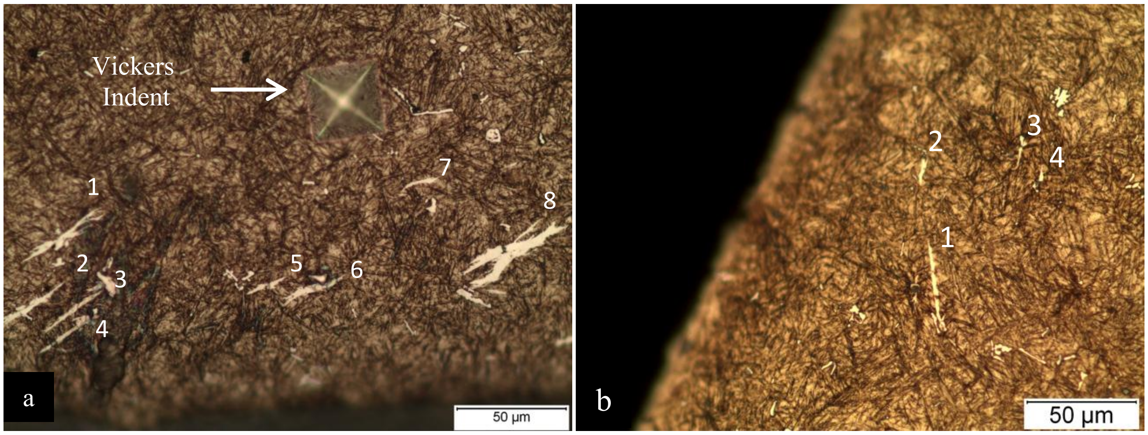

Figure 3.8 At the same magnification (500x), the 4.5 GPa unlubricated M50 sample (a) contains a greater amount of butterflies in general as well as an increase in the number of butterflies of significant size relative to the 4.5 lubricated M50 sample in region 3 (b). The Vickers indent in image (a) is used as a reference point within the sample cross section.

Butterflies were commonly observed in both regions 2 and 3 of this sample and in seemingly different conditions (not specific to region 2 or 3). Region 3 did, however, have a greater amount of butterflies present than in region 2, which is not surprising since a higher stress is experienced in region 3 than region 2. The unlubricated sample also had a significant number of butterflies. When comparing the unlubricated sample to the lubricated sample in Figure 3.8, the unlubricated sample had a greater number of butterflies present within a similar area as the lubricated sample and the butterflies were more easily identifiable due to their larger size. This is thought to be due to the additional stresses imparted on the sample because there is no lubrication between the balls and the cylinder in the RCF test.

Figure 3.6a shows a butterfly with no inclusion present, Figure 3.6b shows a butterfly formed around a M_6C carbide, Figure 3.7a shows a butterfly formed around a dark etching inclusion, and Figure 3.7b shows a butterfly formed around a carbide and two smaller ones formed around dark etching inclusions.

Looking back to Figure 3.6a, and presented again in Figure 3.9, some white etching features were not observed to center around an inclusion or a carbide. Figure 3.9 also shows the angle of the microstructural alteration relative to the surface in the rolling direction to be approximately 30° which is synonymous with low angle WEBs. Because of this, they were originally thought to be WEBs but were very sparse within the microstructure and lacked the density in which WEBs have been observed in past studies. Additionally, when looking at a lower magnification image (Figure 3.10), these white etching features are observed with butterflies and both the butterflies and the white etching features were oriented in relatively the same direction towards the surface in the rolling direction. These observations called for further investigation to verify the correct identity of these microstructural alterations.

To characterize the angle in which the butterflies were observed relative to the surface, forty total measurements were performed. The measurements consisted of data from both the lubricated and unlubricated samples in which there was not a significant different from one sample to the next. The average angle was 31° ± 7° with the lowest observed angle to be 19° and the highest observed angle to be 50°. This differs from previous literature in which butterflies are observed to occur 45° to the surface in the rolling direction.[42]

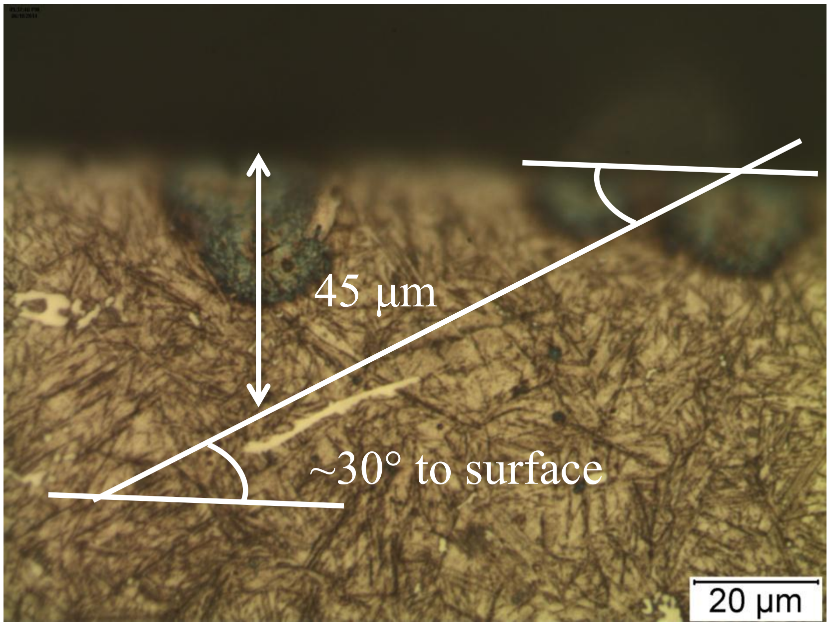

Figure 3.9 A white etching feature that occurs approximately 30° to the surface in the rolling direction is shown in the 4.5 GPa/10^8 cycles unlubricated M50 sample.

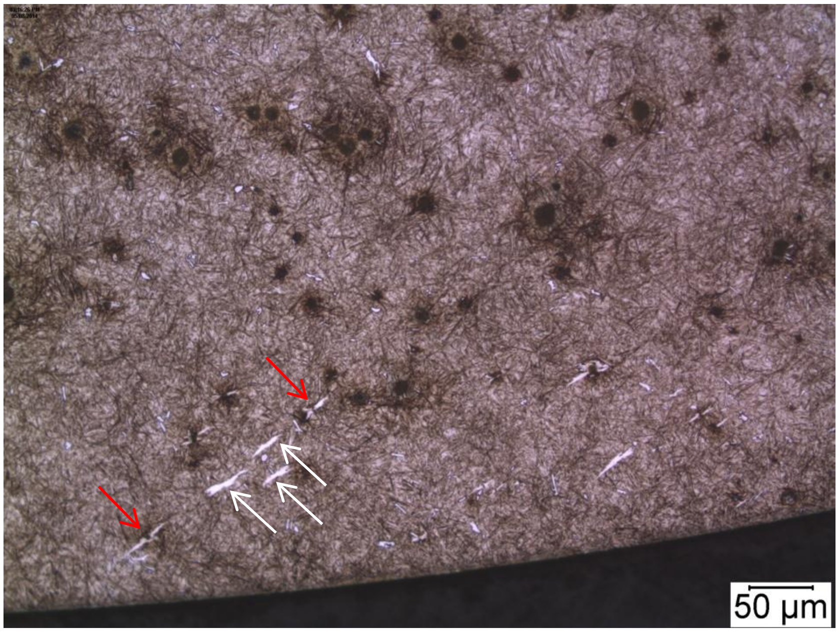

Figure 3.10 The white etching features are designated by the white arrows and the butterflies by the red arrows. They are all oriented in relatively the same direction.

To determine whether or not these white etching features were butterflies or bands, a form of serial sectioning was done to slowly remove material and investigate these features as a function of depth. The exact amount of material removed in each step is unknown, but the main purpose of this experiment was to reveal the white etching features to be either white etching bands or butterflies. The exact total amount of material removed, however, was close to 25 µm and was calculated by measuring the Vickers indent length in the image in which the butterfly began as well as in the frame the butterfly disappeared and determining the depth to area ratio of the indent. The results are shown in a series of images in Figure 3.11.

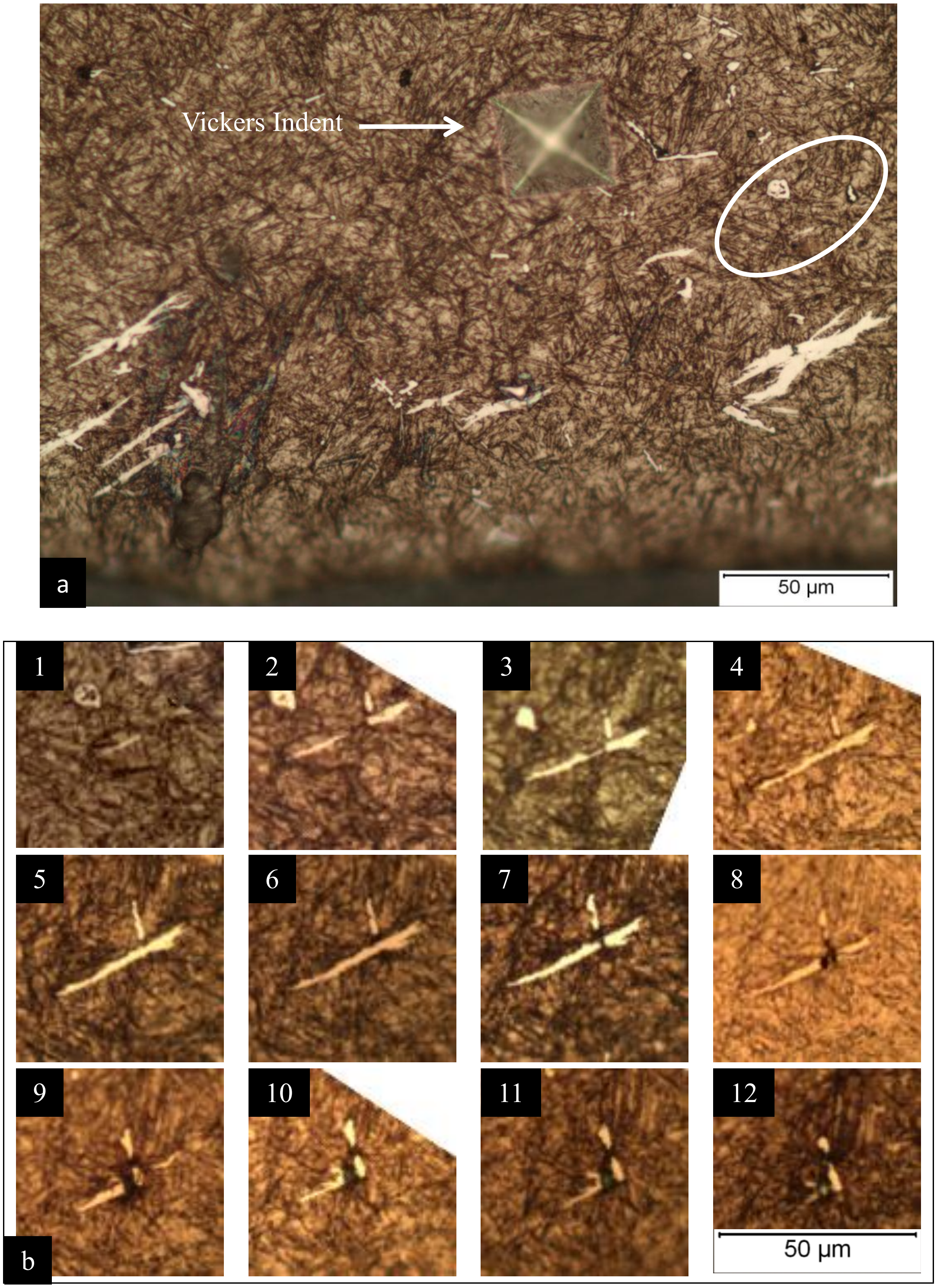

Figure 3.11 (a) The original image and location within the sample, designated by a Vickers indent, of a microstructural alteration being examined (defined by white oval) and (b) the evolution of a butterfly in the predefined region shown in 12 slices. The single scale bar applies to all images.

Figure 3.11 proves that the aforementioned white etching features that were once believed to be WEBs are indeed butterflies. Images 4-6 of Fig. 3.11b show a single white etching band, but upon further material removal, an inclusion is in fact present. Image 2 illustrates also that it is possible to view the wings of the butterfly with only the martensitic matrix between them so as to appear to be two separate entities.

As has been previously stated, butterflies are typically observed to form around nonmetallic inclusions.[5] The dark etching inclusion observed in Figures 3.7a and 3.7b was assumed to be an alumina inclusion based on previous literature. To verify this, however, electron dispersive spectroscopy (EDS) was performed on the inclusions. Figure 3.12 shows an SEM image of a butterfly centered on a dark etching inclusion and the spectrum and quantitative EDS results are presented in Figure 3.13.

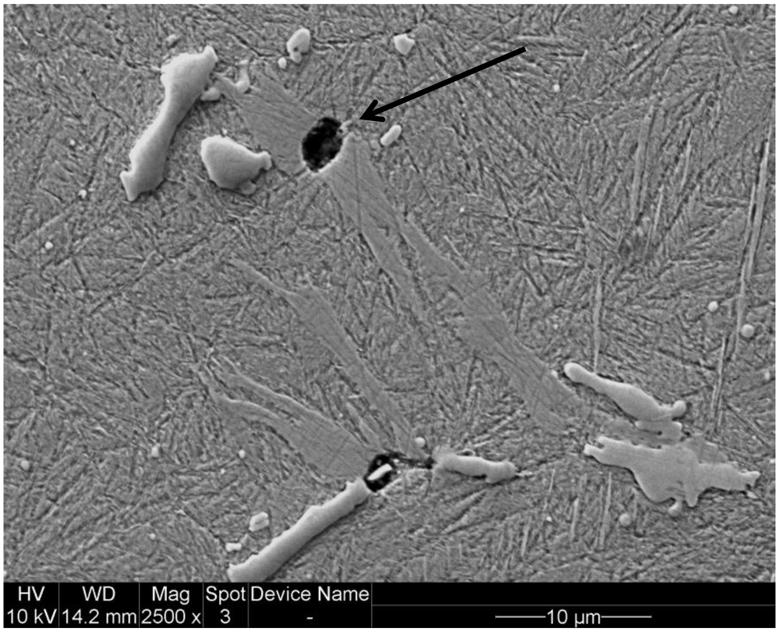

Figure 3.12 SEM image of a butterfly centered around a dark-etching inclusion as shown by the arrow in M50 steel.

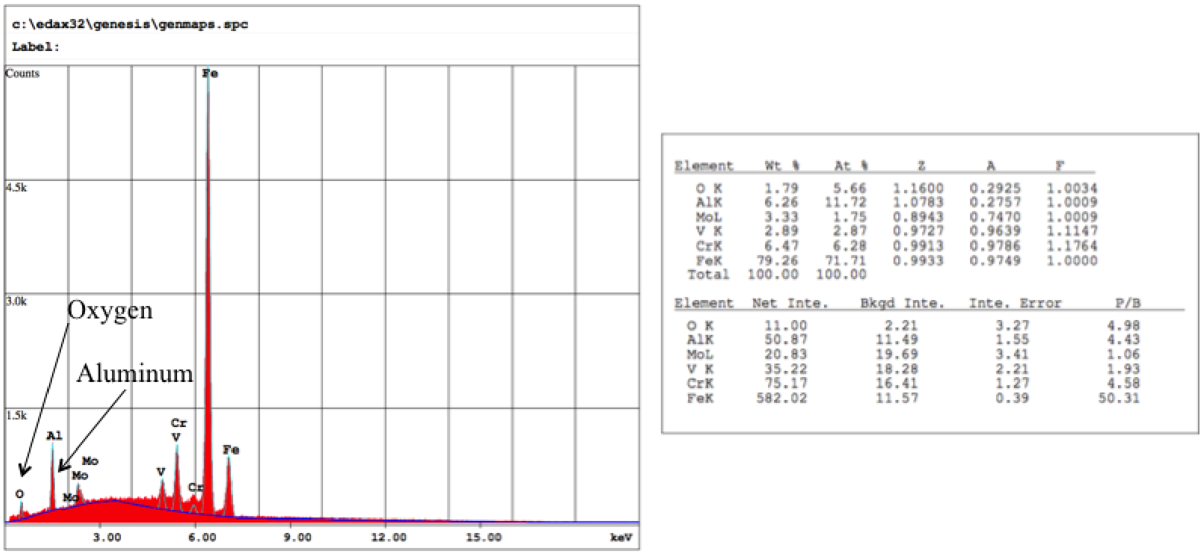

```
Element    Wt %     At %       Z         A         F
  O K      1.79     5.66    1.1600    0.2925    1.0034
  AlK      6.26    11.72    1.0783    0.2757    1.0009
  MoL      3.33     1.75    0.8943    0.7470    1.0009
  V K      2.89     2.87    0.9727    0.9639    1.1147
  CrK      6.47     6.28    0.9913    0.9786    1.1764
  FeK     79.26    71.71    0.9933    0.9749    1.0000
 Total   100.00   100.00

Element  Net Inte.    Bkgd Inte.   Inte. Error      P/B
 O K       11.00         2.21          3.27          4.98
 AlK       50.87        11.49          1.55          4.43
 MoL       20.83        19.69          3.41          1.06
 V K       35.22        18.28          2.21          1.93
 CrK       75.17        16.41          1.27          4.58
 FeK      582.02        11.57          0.39         50.31
```

Figure 3.13 All the expected alloying elements of M50 (Mo, V, Cr) as well as Fe are present but aluminum and oxygen peaks are also present suggesting the dark etching center of a butterfly is formed around an alumina inclusion.

As was originally suggested, the dark etching inclusion is most likely alumina. The exact stoichiometry is unknown, but both aluminum and oxygen peaks were present wherein they would not typically be present in and EDS spectrum of the matrix.

SEM was also used to investigate the butterflies for the presence of cracks as literature has commonly stated the presence of microcracks with the formation of butterfly wings. Figure 3.14 shows two separate butterflies in which cracks were present.

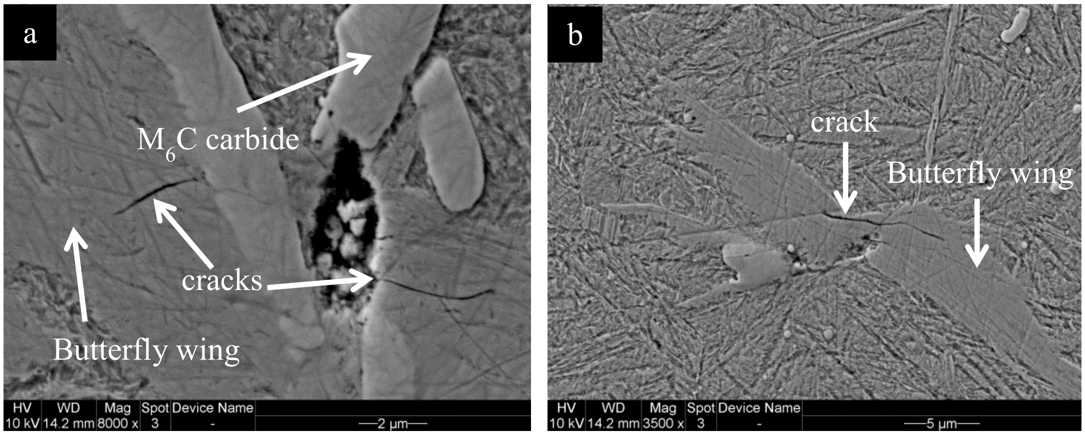

Figure 3.14 Both images show cracks present in two separate butterflies.

Only two SEM images are shown, but more butterflies were observed to contain similar cracks as those shown in Figure 3.15.

On a final note regarding the butterflies observed optically in regions 2 and 3 of this sample, it has previously been stated that butterflies do not form around carbides.[40] Based on Figure 3.6b and 3.7b, however, this appears to be false because butterflies are indeed observed to be centered around carbides. Alternatively, images 9-11 of Figure 3.11b show two carbides adjacent to an alumina inclusions (perpendicular to the actual butterfly) whereas before the top carbide is observed without the bottom carbide and alumina inclusion. This implies an alumina inclusion can be present adjacent to the carbide even though in a single cross section of a butterfly it might not be visible. To determine whether or not butterflies do form strictly around carbides, further experimentation such as serial sectioning would need to be performed.

Another interesting feature was observed in region 3 and is shown in Figure 3.15. There are small, acicular white etching features observed subsurface around the majority of the circumference granted that no spalling is present. There was a range of sizes in which these features were observed.

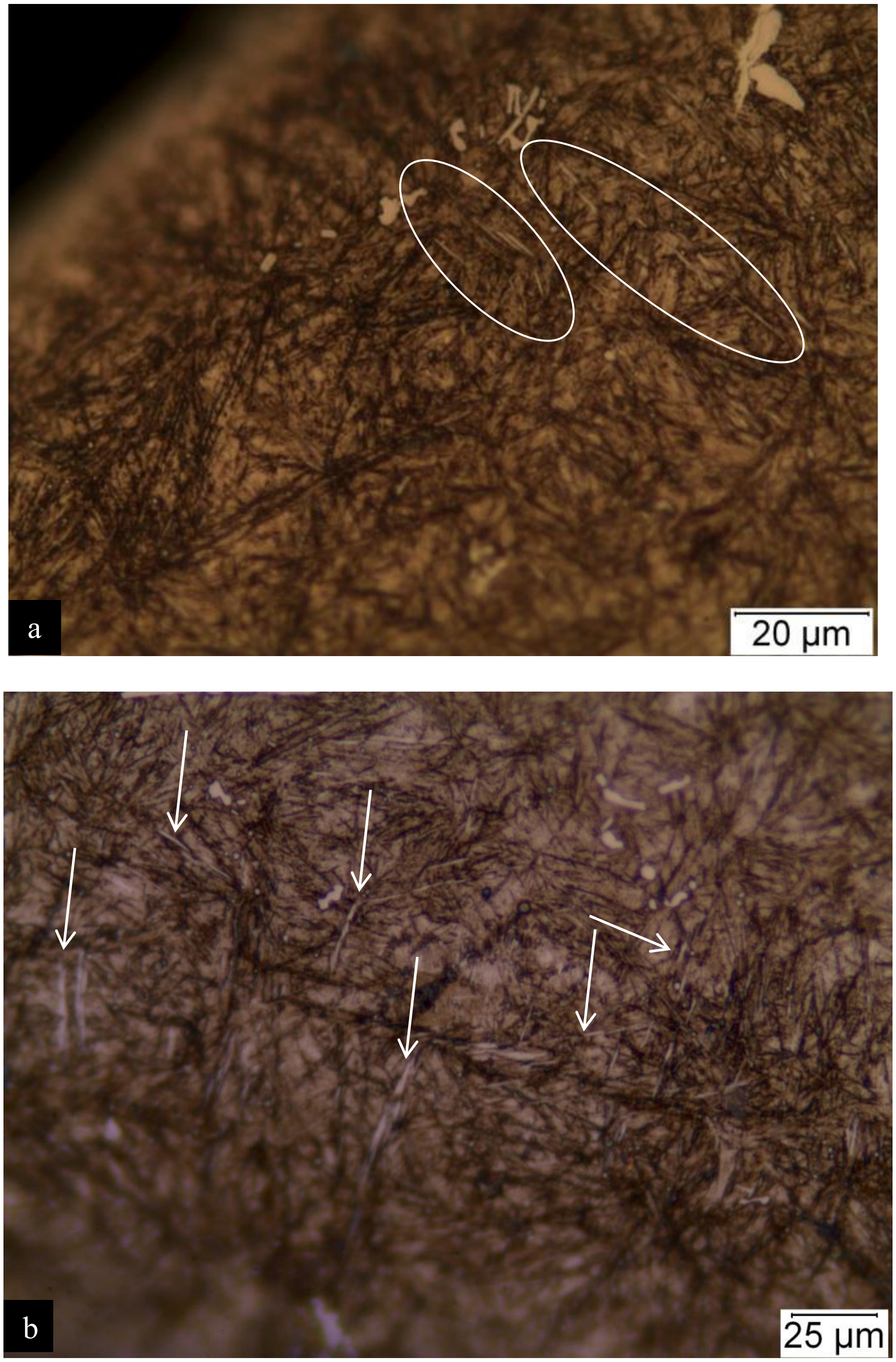

Figure 3.15 Very small acicular white etching areas (circled in (a) and marked with arrows in (b)) were also observed in region 3 of the 4.5 GPa/10^8 cycles lubricated M50 sample.

Ten dimensional measurements were taken on the smallest observed of these features. The length was 5.5 ± 1.1 μm and the width was 0.6 ± 0.1 μm. There were also similar white etching features that were slightly bigger in the same region and likewise, ten measurements were taken. The length of the larger observed white features was 17 ± 6 μm and the width was 2 ± 1 μm. In every observed instance, these features were somewhere between 40 to 100 microns below the surface. There were low angle features as well as high angle features. The low angle features were observed to be less than 20° in relation to the surface (assumed to be in the rolling direction) and the high angle features were typically between 80° and 100°. Although both low and high angle features were commonly observed, there were only a couple images taken in which a butterfly was present to validate the rolling direction. There were two separate micrographs containing butterflies and white etching features in which one showed a white etching feature to be close to 80° and the other showed it to be 100°.

Figure 3.16 is an image of 30° white etching bands observed by Swahn in 1976 in a 52100 deep groove ball bearing. Even though the angles in which these WEBs appear are different, they bear a marked resemblance to the white etching features observed in this study. However, more experiments would need to be performed to make a conclusion on the white features observed in this study.

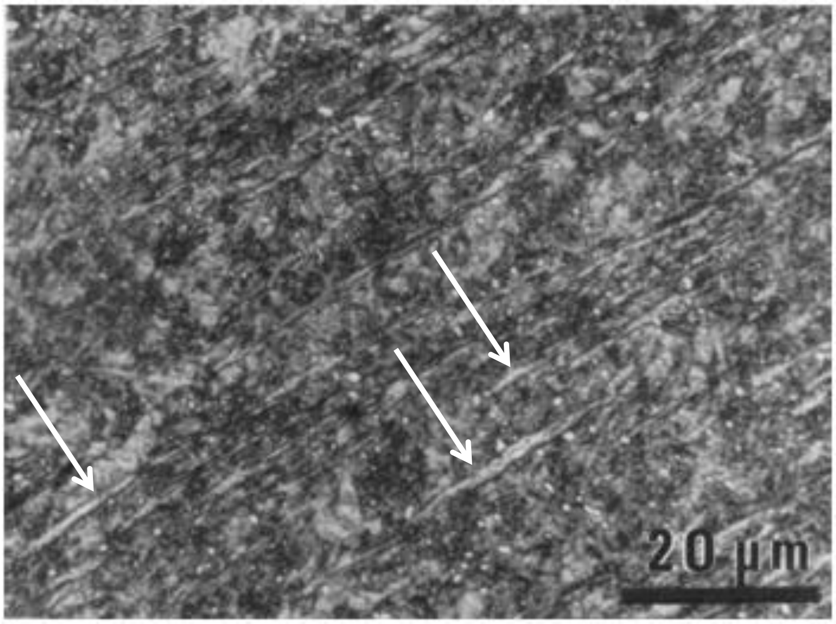

Figure 3.16 30° white etching bands (a few pointed out by the white arrows) observed in 52100 steel by Swahn.[40]

3.2.2 Lubricated/Unlubricated 4.5 GPa Loaded M50 to 10^8 Cycles (Nanoindentation)

Matrix arrays of 3 columns by 30 rows, as laid out in section 2.5.2, were done in pristine M50 material as well as in regions 1, 2, and 3 of the 4.5 GPa /10^8 cycles lubricated M50 sample. In the pristine material, four separate arrays were performed for a total of 360 indents and the average hardness was determined to be 8.86 ± 0.37 GPa. Indents that appeared to be high or low relative to the majority of the indents were excluded from the average because they either represented an indent performed on a carbide or inclusion (not representative of the matrix hardness) or there was something that affected the actual indentation process and produced an uncharacteristic load-displacement curve (also not representative of the matrix hardness). The four graphs are presented in Figures 3.17 and 3.18 as hardness plotted relative to depth below the surface. However, for indents performed in the pristine material the depth of the indents are trivial.

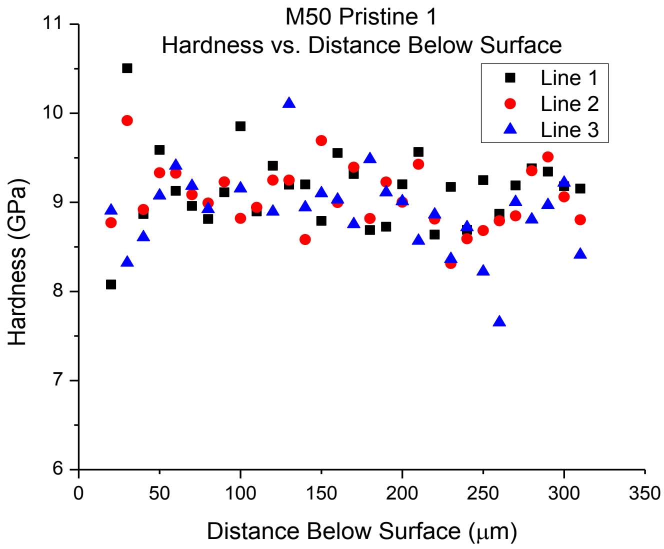

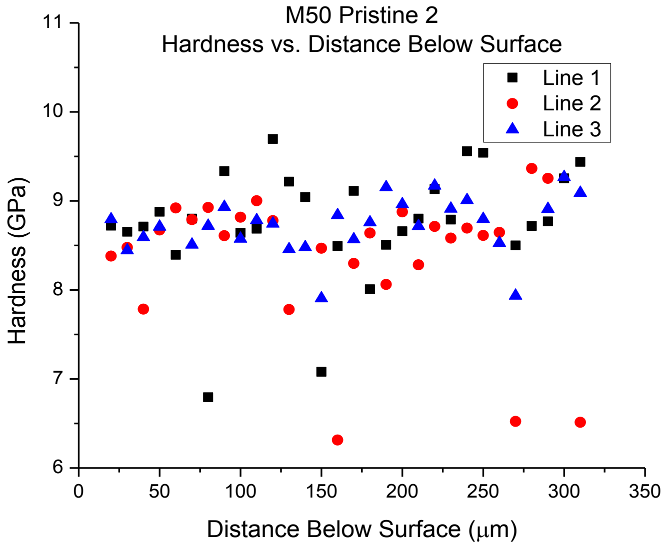

Figure 3.17 Hardness measurements as a function of depth beneath the surface in pristine M50 material of two separate data sets.

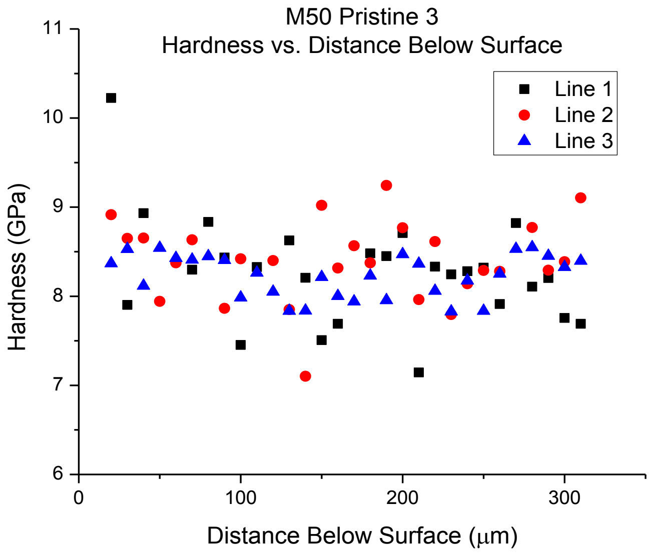

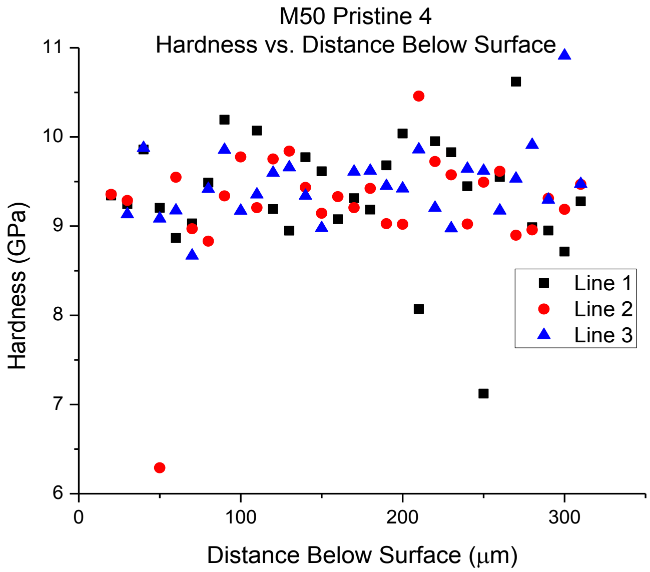

Figure 3.18 Hardness measurements as a function of depth beneath the surface in pristine M50 material for two more data sets.

Figures 3.19-3.22 present the data collected in regions 1-3 for the 4.5 GPa/10^8 lubricated M50 sample.

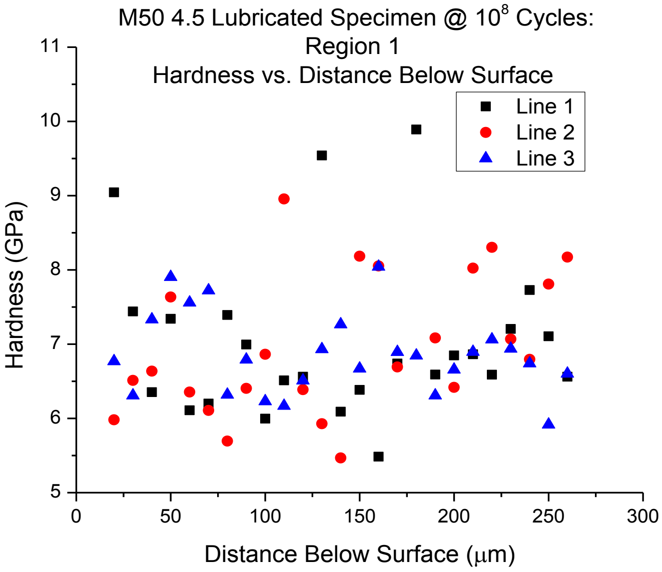

Figure 3.19 Hardness measurements as a function of depth beneath the surface with 10 micron increments in Region 1.

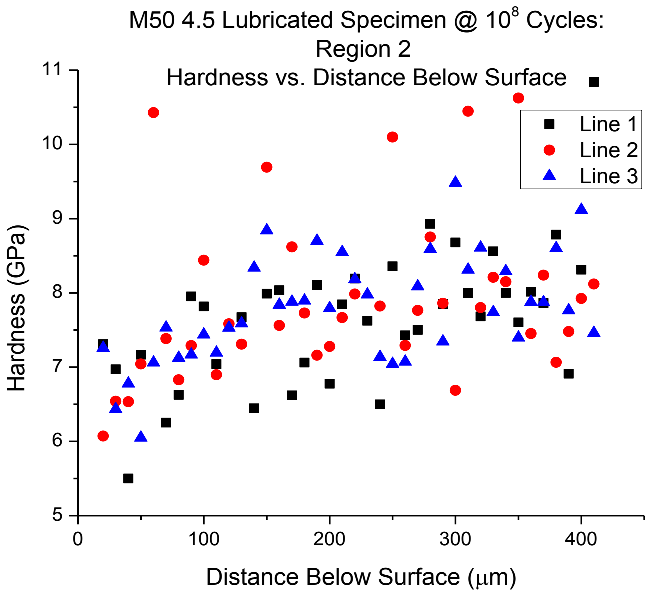

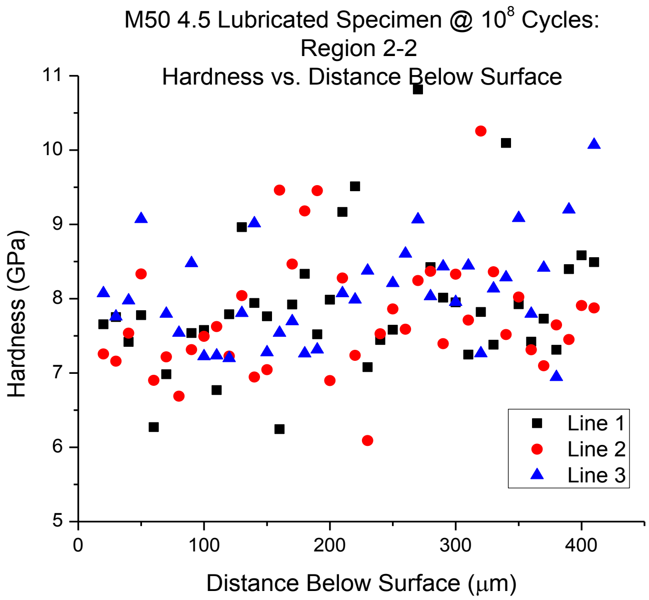

Figure 3.20 Hardness measurements in two separate locations as a function of depth beneath the surface with 10 micron increments in Region 2.

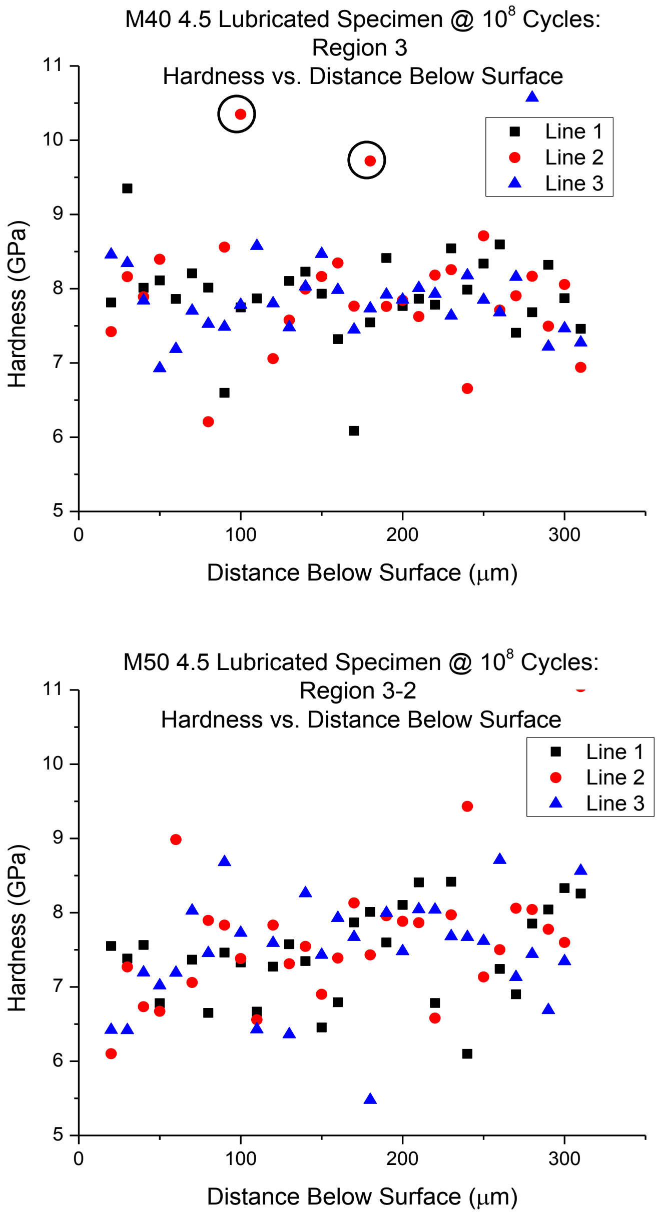

Figure 3.21 Hardness measurements in two separate locations as a function of depth beneath the surface with 10 micron increments in Region 3.

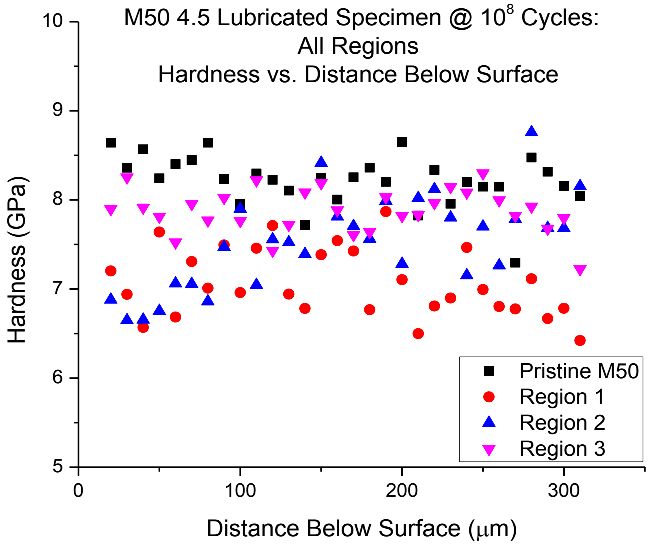

Figure 3.22 Comprehensive hardness measurements as a function of depth beneath the surface with 10 micron increments in all regions indented in the 4.5 GPa/10^8 cycles lubricated M50 sample.

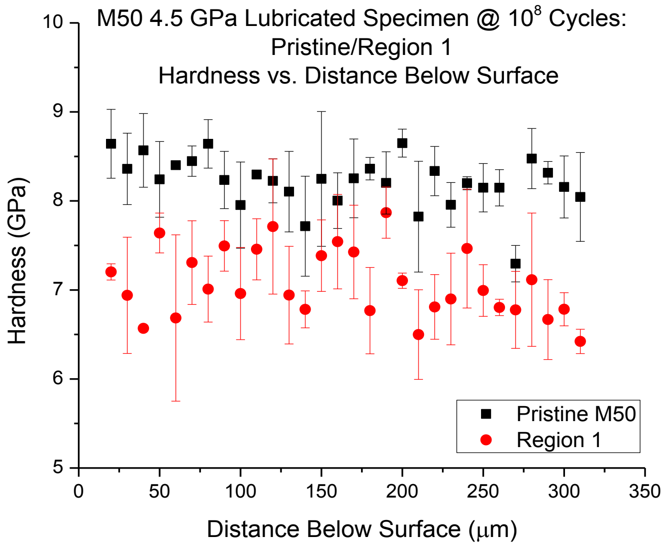

Figure 3.23 Pristine M50 and Region 1 were plotted with standard error bars and compared to observe data overlap.

When analyzing these graphs, there was no definitive trend in any region of the hardness as a function of depth. Since no trend was observed the average hardness was calculated for each region and is presented in Table. 3.3. Note in Figure 3.21, however, the data points that are circled. Some indents resulted in higher than average hardness values and those were very often related to indenting on a carbide rather than the matrix. For the purpose of average hardness values, those values were not included. In Figure 3.22, however, the average hardness as a function of depth for each region was plotted on the same graph for comparison purposes. A Kolmogorov-Smirnov statistical analysis was performed for the data sets of Figure 3.22, and in every case, each set of data was significantly different from each other set of data. For this particular analysis, this meant the distribution of the data was significantly different. From that graph, Figure 3.23 was generated to observe the lowest average values and highest average values plotted with standard error bars to observe any overlap. As can be seen, there is not significant overlap between the pristine values and region 1 values. However, if regions 2 and 3 were inserted into this graph, there would be significant overlap present between regions by using the standard error approach.

Table 3.3 The average hardness calculated for Regions 1, 2, and 3 of the 4.5 GPa/10^8 cycles lubricated M50 sample.

Sample	Average Hardness (GPa)	Std. Deviation
Pristine	8.86	0.37
4.5 Lub Region 1	7.08	0.66
4.5 Lub Region 2	7.67	0.75
4.5 Lub Region 3	7.8	0.4

A definite drop in hardness is observed from the pristine material to regions 1, 2, and 3. Region 1 shows the lowest hardness value, and regions 2 and 3 are not significantly different. At present, the data from region 1 was collected from the sample while the sample was still mounted in the transparent thermoplastic mount while the other regions were collected with the sample broken out of the mount. Because of this, there is extra compliance in the system, and the data may be less accurate. However, the extent of effect the thermoplastic mount has on the measurements is unknown.

The original objective of this experiment was to observe white etching bands and take hardness measurements in and around them and investigate the different regions in which different stresses were imparted to see how hardness changed as a function of depth within the material as well as location within the wear track. Unfortunately, no white etching bands (definitively) were observed. The plan, however, was still executed with the intent of observing possible hardness changes even before white etching bands form and with present butterfly formation. A drop in hardness might suggest the material has undergone plastic deformation and a form of mechanical tempering has occurred. However, if that were the case, it would be more plausible to see a drop in hardness in the region of maximum shear stress and to see the hardness increase as indents were taken deeper into the material rather than an overall average lower hardness for all the indents.

In general, the majority of the indents fall within the same hardness range, but there is still scatter in the data. Within the microstructure itself, there are inclusions and carbides along with the tempered martensitic matrix. The indents are small enough that they could be done within a martensitic plate or on a boundary of a martensitic plate. Several could be taken within a single prior austenite grain or on a prior austenite grain boundary. The purpose of this argument is to present the possibilities of scatter within the data. Because prior austenite grains were able to be revealed, a test was done to see if indenting in different grains or on grain boundaries had an effect. The results are given in Table 3.4. The grains were designated as small, medium, or large and a key is given below the table to understand the nomenclature. There was no specific requirement for a grain to be small versus medium, or medium versus large, they were simply designated that way based on viewing all the grains in the viewing window and appeared to fall into those three categories. Table 3.5 gives the average values associated with Table 3.4 for overall hardness values from within a prior austenite grain (regardless of grain size) versus those on a grain boundary.

Table 3.4 Hardness measurements taken in different prior austenite grains as well as on the boundaries.

Indent	**Hardness (GPa)**	**Indent**	**Hardness (GPa)**	**Indent**	**Hardness (GPa)**
GS-1	6.4	**GM-1**	6.24	**GL-1**	6.33
GS-2	6.28	**GM-2**	5.99	**GB-1**	7.84
GS-3	7.85	**GM-3**	6.14	**GB-2**	7.96
GS-4	6.58	**GM-3**	5.56	**GB-3**	8.01
GS-5	6.97	**GL-1**	6.13	**GB-4**	8.39
GS-6	5.57	**GL-1**	6.09	**GB-5**	7.98

**GS: small grain, GM: medium grain, GL: large grain, GB: grain boundary

Table 3.5 The average hardness values for indents taken within a prior austenite grain vs. indents taken on a prior austenite grain boundary.

	Grains	Grain Boundaries
Overall Average (GPa)	6.31	8.04

Different numbers associated with the letter designation represents different grains indented. If the number is the same (ex. GM-3 appears twice), the hardness values given correspond to indents performed in the same prior austenite grain. There is still scatter in the data when indented in different grains or within the same grain as in GM-3. The hardness values were consistent in GL-1, but more tests need to be performed to better understand the effect of prior austenite grains on the hardness values. The most definitive conclusion from this data is that the hardness is consistently higher when an indent is performed on a prior austenite grain than within a grain itself.

Seemingly, microindentation may be the overall better method to determine the matrix hardness since it samples a larger area. However, because of the dimension of the cylindrical rods and for this particular experiment, nanoindentation was the better choice. Nanoindentation allowed more indents to be taken in the region of interest, whereas microindentation would have limited that aspect. It especially would have been helpful in the event white etching bands had been observed.

Even though white etching bands were not observed, there were still a significant amount of butterflies present in the microstructure, and therefore multiple butterflies were investigated using the scanning probe microscopy function of the Hysitron TI-950 to investigate the hardness of the butterfly wing versus the matrix microstructure. A large, well-defined butterfly is presented in Figure 3.24 with indents taken in and around the region of the butterfly.

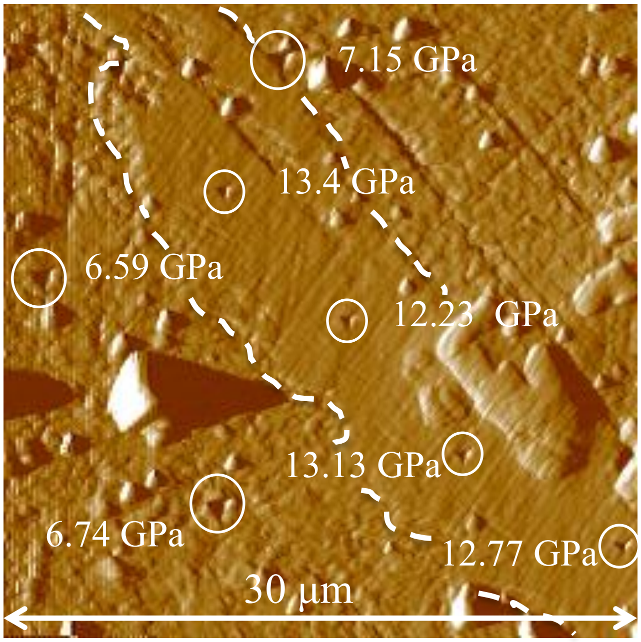

Figure 3.24 Hardness values in a butterfly wing (outlined by dotted white line) as well as in the matrix surrounding it.

The butterfly wing is recognizable by its smooth-appearing surface relative to the general martensitic matrix. As can be seen in Figure 3.24, the indents performed in the butterfly wing produced a significantly higher hardness value than the surrounding matrix. The higher values are consistent with previous literature in which it is stated that the wing is comprised of a very small dislocation cell structure with grains on the order of 10-20 nm. Other butterflies that were indented also showed the same trend of a higher hardness in the butterfly wing than in the surrounding matrix. Indents were also taken just outside the butterfly wing to investigate if the hardness was higher or lower in that area relative to the matrix. Figure 3.24 shows an image in which indents were taken on the edge of a butterfly wing.

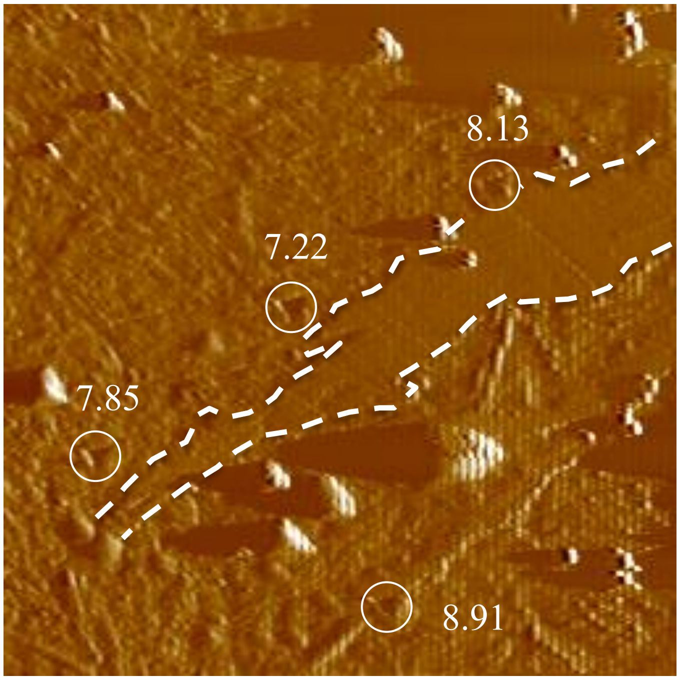

Figure 3.25 The values in this image are in GPa, and are performed just above a butterfly wing from Region 3 of the 4.5 GPa/10^8 cycles lubricated M50 sample.

The indents performed above the butterfly wing in Figure 3.25 have hardness values that fall within the scatter of data taken in a matrix array in Region 3. Additionally, more indents would need to be performed for a better set of data to analyze and make a conclusion on whether or not hardness just outside the wing was different than the matrix.

Finally, the white etching features observed in Region 3 that were unable to be positively identified were also investigated. Figure 3.26 shows the optical image associated with the scanning probe microscopy image to better understand the region that was probed. It also presents hardness in GPa within the region of these unknown alterations, however, again, there does not appear to be a consistent trend within the data.

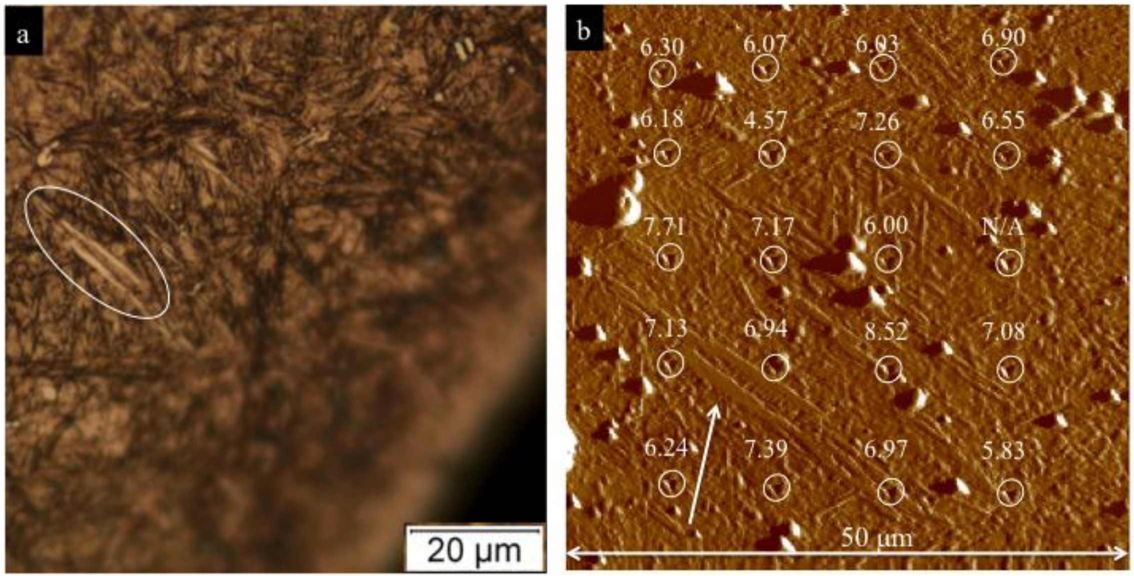

Figure 3.26 Image (a) is shown to identify the white etching features examined in the nanoindenter using SPM. Image (b) is a topography image from the Hysitron TI-950 and the feature designated by the arrow is the same feature circled in Image (a). Values in Image (b) are in GPa.

The scanning probe microscopy function of the Hystron TI-950 proved to be very useful in the investigation of any and all microstructural alterations that were observed in the microstructure. It allowed indents to be strategically placed with a better view of the microstructure than that of the digital optical column in the Hystron TI-950. Butterflies were easily identifiable and able to be probed and the white etching features were quite a bit smaller, but they showed a different structure than the typical martensitic matrix that seemed to resemble the smoothness of the butterfly structure.

3.2.3 Lubricated/Unlubricated 5.0 GPa Loaded M50 to 108 Cycles

The following section presents the optical images obtained from Regions 1-3 for both the lubricated and unlubricated 5.0 GPa/10^8 cycles M50 samples as well as the hardness matrices (as previously outlined) taken in each respective region. Figures 3.27-3.29 show the microstructure of the lubricated sample and Figures 3.30-3.32 show the microstructure of the unlubricated sample.

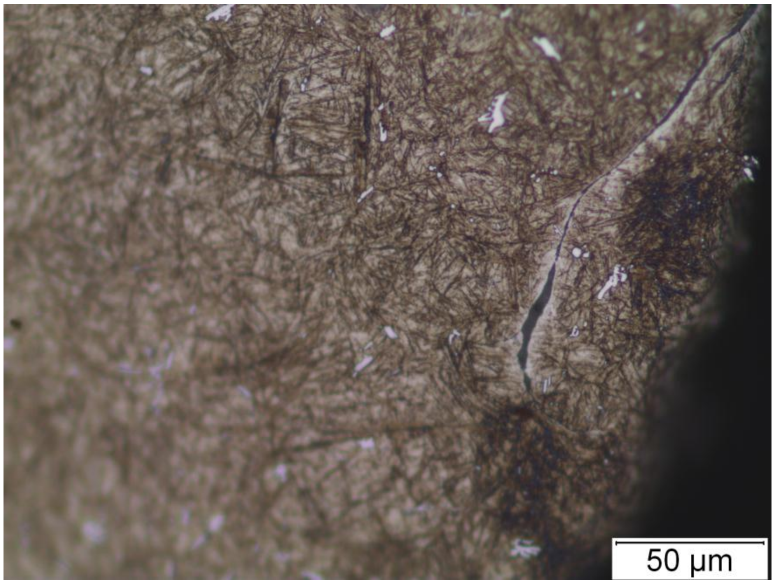

Figure 3.27 The typical microstructure observed in Region 1 of the lubricated 5.0 GPa/10^8 cycles M50 sample. Cracks as the one seen in this image were commonly observed (500x).

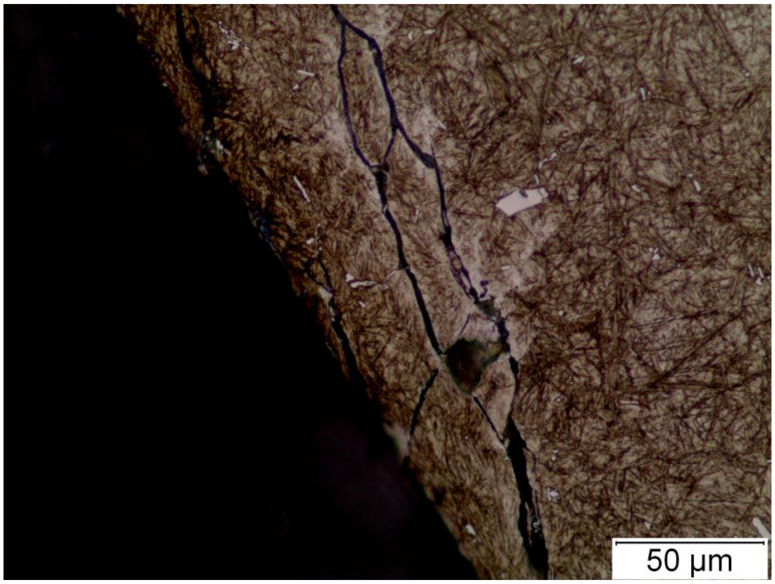

Figure 3.28 More cracks observed in Region 2 of the lubricated 5.0 GPa/10^8 cycles M50 sample, but no microstructural alterations (500x).

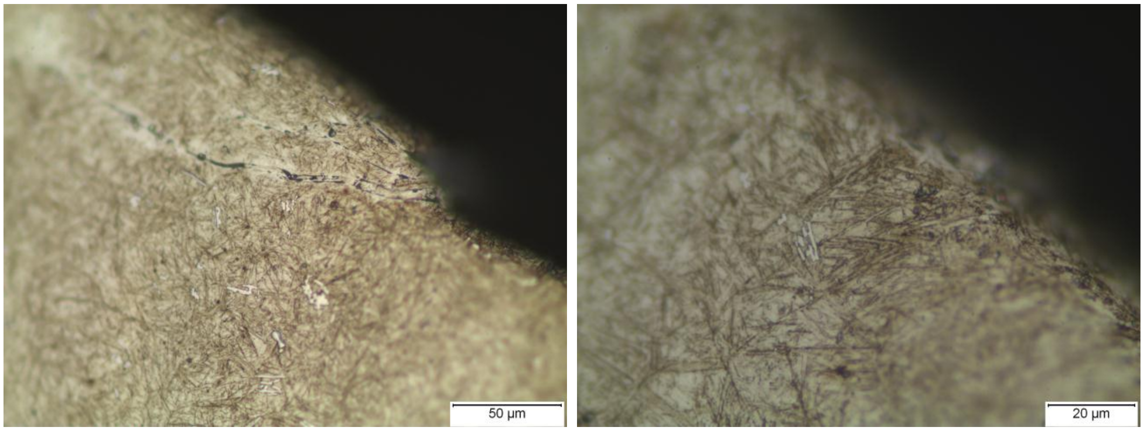

Figure 3.29 Microstructure observed in Region 3 at 500x (left) and 1000x (right) of the lubricated 5.0 GPa/10^8 cycles M50 sample. Cracks are again observed in this region.

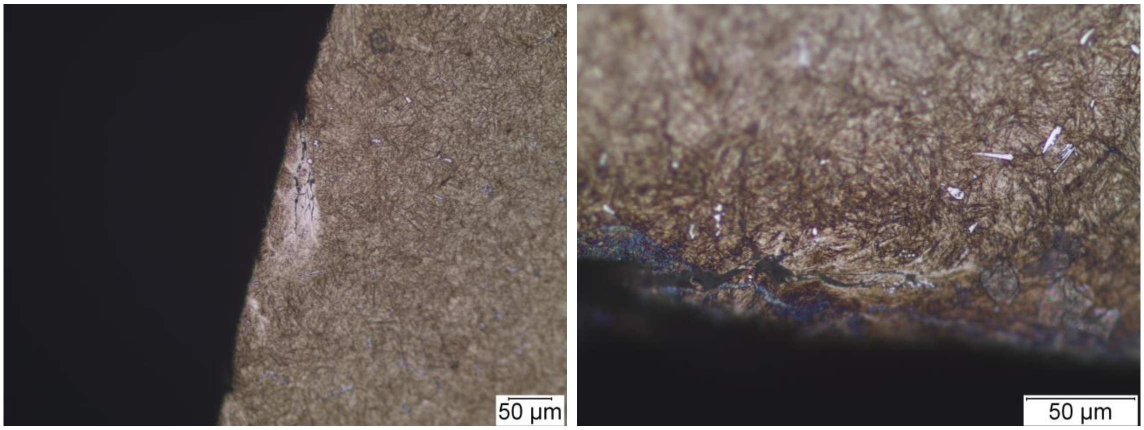

Figure 3.30 Microstructure in Region 1 of the unlubricated 5.0 GPa/10^8 cycles M50 sample. Cracks are observed near the surface.

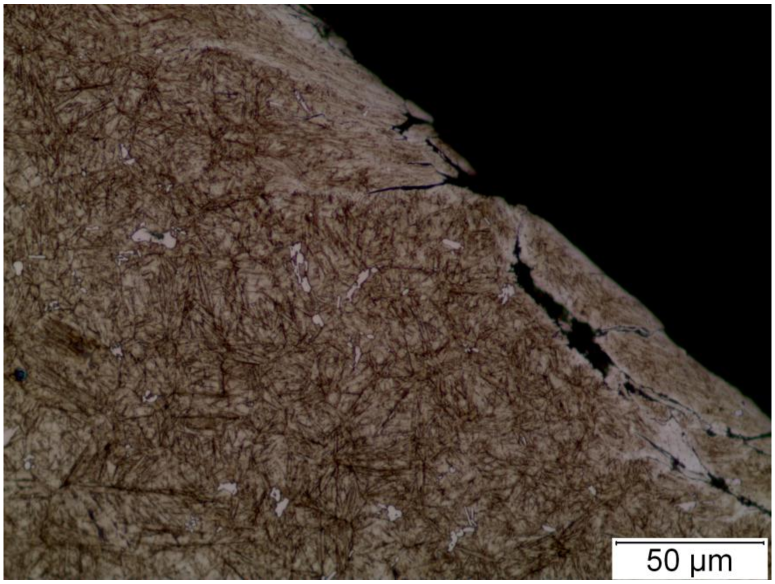

Figure 3.31 Microstructure showing cracks in Region 2 of the unlubricated 5.0 GPa/10^8 cycles M50 sample.

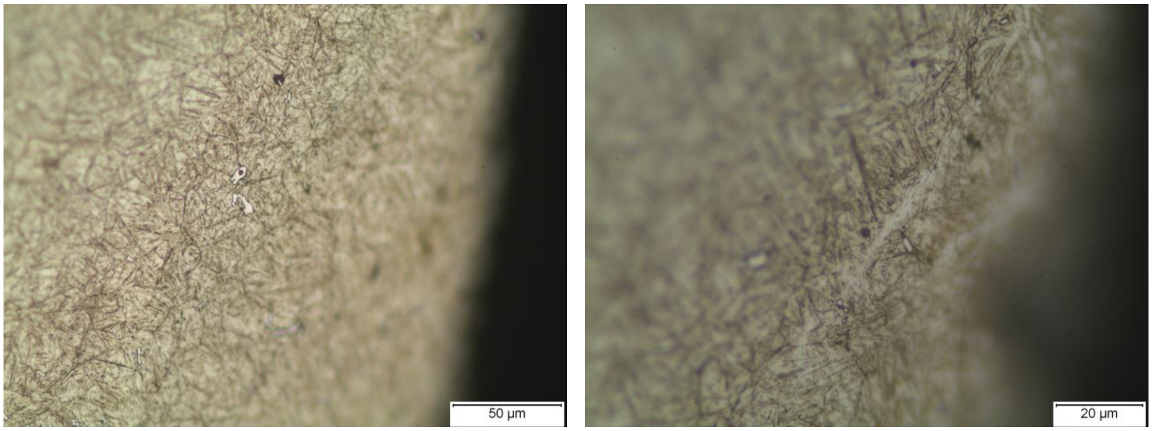

Figure 3.32 Microstructure in Region 3 of the unlubricated 5.0 GPa/10^8 cycles M50 sample. Shows the same as Regions 1 and 2, however it was more lightly etched.

In both the lubricated and unlubricated sample, and in every region, no microstructural alterations were observed. Subsurface cracks were observed, but that is expected as the entire circumference of the cylindrical rod in both samples had severe spalling. The severity of the spalling can be seen in Figure 3.33.

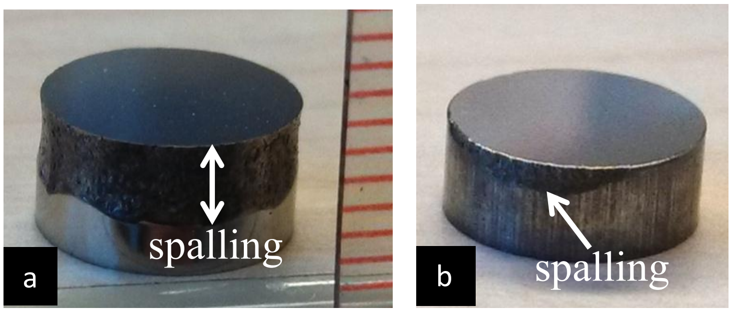

Figure 3.33 The spalling of the 5.0 GPa was severe as can be seen in image (a). Each red tick mark on the right represents a millimeter and the total width of spalling is on the order of 3 mm. It is compared to the spalling of a sample loaded at 4.5 GPa in image (b).

The amount of material removed due to spalling was calculated to be approximately 185 μm in Region 2 of both the lubricated an unlubricated sample and approximately 70 μm and 120 μm in Region 3 of the unlubricated and lubricated sample respectively. It was not determined for Region 1, however, for graphing purposes, the amount removed was assumed to be the same as Region 2.

The following graphs are the hardness vs. distance below the surface for both the lubricated and unlubricated 5.0 GPa/10^8 cycles M50 samples. The data starts at the values previously mentioned for the respective regions since the material from the original surface was removed.

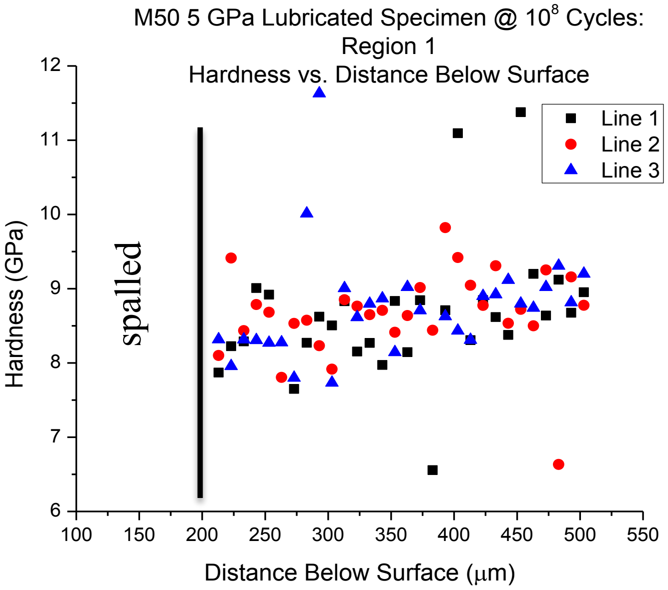

Figure 3.34 Hardness as a function of depth below the surface in which case the amount spalled off the surface was taken into consideration in Region 1 of the 5.0 GPa loaded to 10^8 cycles lubricated sample.

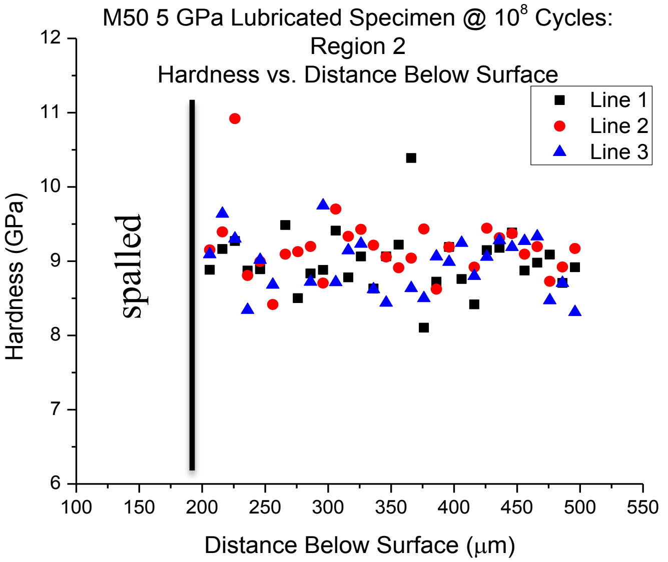

Figure 3.35 Hardness as a function of depth below the surface in which case the amount spalled off the surface was taken into consideration in Region 2 of the 5.0 GPa loaded to 10^8 cycles lubricated sample.

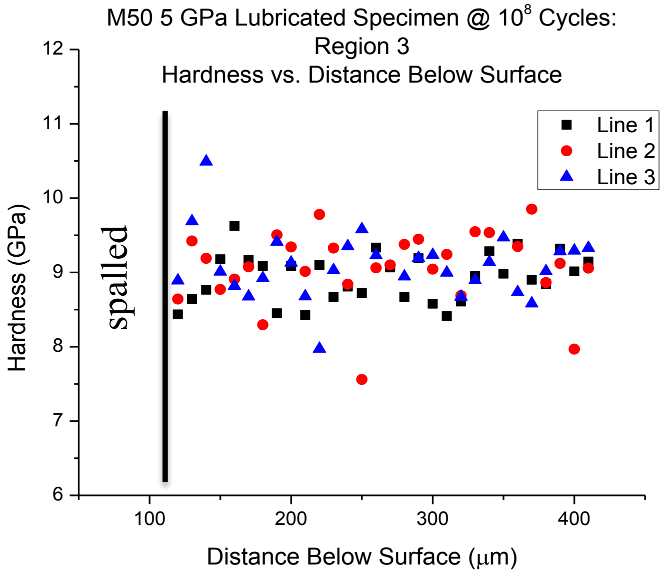

Figure 3.36 Hardness as a function of depth below the surface in which case the amount spalled off the surface was taken into consideration in Region 3 of the 5.0 GPa loaded to 10^8 cycles lubricated sample.

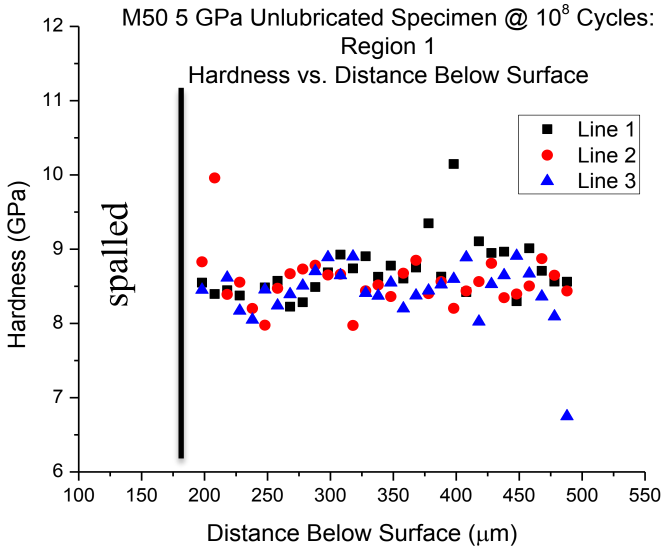

Figure 3.37 Hardness as a function of depth below the surface in which case the amount spalled off the surface was taken into consideration in Region 1 of the 5.0 GPa loaded to 10^8 cycles unlubricated sample.

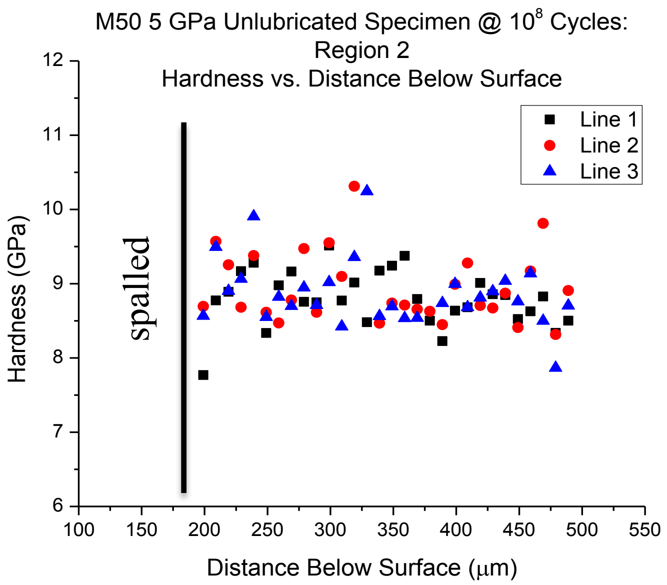

Figure 3.38 Hardness as a function of depth below the surface in which case the amount spalled off the surface was taken into consideration in Region 2 of the 5.0 GPa loaded to 10^8 cycles unlubricated sample.

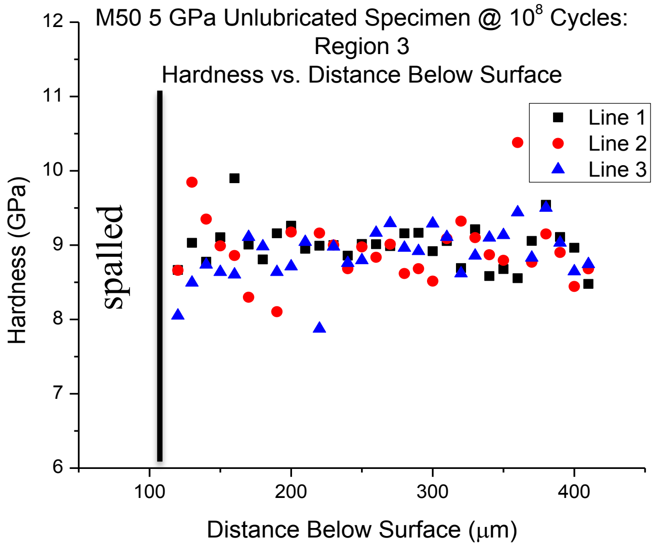

Figure 3.39 Hardness as a function of depth below the surface in which case the amount spalled off the surface was taken into consideration in Region 3 of the 5.0 GPa loaded to 10^8 cycles unlubricated sample.

Table 3.6 The average hardness values from both 5.0 GPa/10^8 cycles M50 samples.

Sample	Average Hardness (GPa)	Std. Deviation
Pristine	8.86	0.37
5 Lub Region 1	8.67	0.86
5 Lub Region 2	9.00	0.33
5 Lub Region 3	9.05	0.34
5 Unlub Region 1	8.57	0.3
5 Unlub Region 2	8.87	0.44
5 Unlub Region 3	8.91	0.28

The average hardnesses were determined for each region in both samples, and there was no significant change from region to region or from the pristine value. Because of the severe spalling, however, the regions of interest in both of these samples were spalled off from the surface. It is also unknown how many cycles the present material went through and at what load because of the spalling. Therefore, these samples were trivial for the investigation of the regions in which microstructural alterations occur.

3.2.4 Lubricated 4.0/4.5 GPa Loaded 52100 to 10^8 Cycles

The following section presents the microstructures observed and hardness data collected in the 4.0 GPa and 4.5 GPa lubricated 52100 samples.

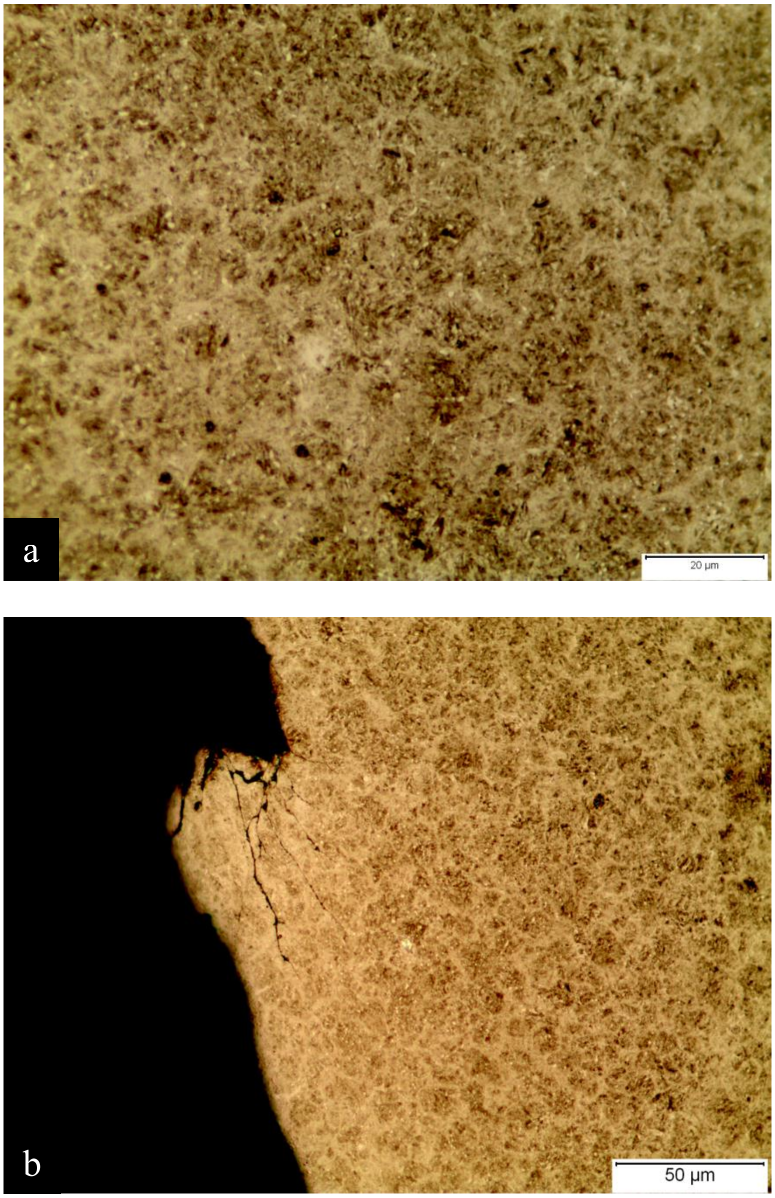

Figure 3.40 Microstructure in Region 1 of the 4.5 GPa 52100 sample. No alterations are observed in this sample (a) (1000x) relative to the pristine microstructure but cracking is present as there was spalling (b) (500x).

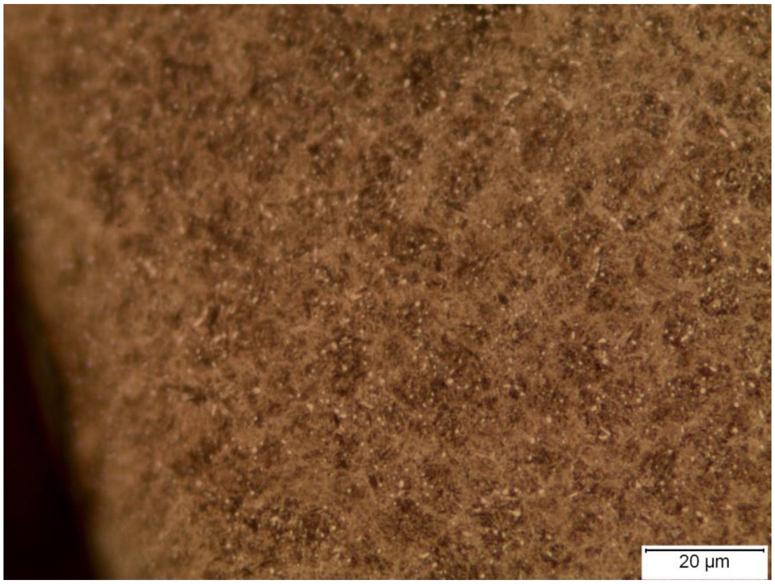

Figure 3.41 Microstructure in Region 2 of 4.5 GPa/10^8 cycles 52100 sample showing no change.

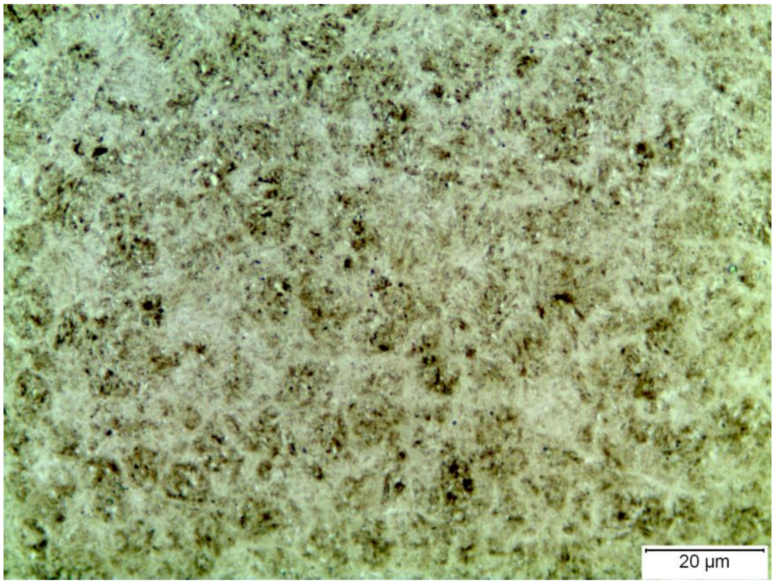

Figure 3.42 Microstructure in Region 3 of 4.5 GPa/10^8 cycles 52100 sample showing no change.

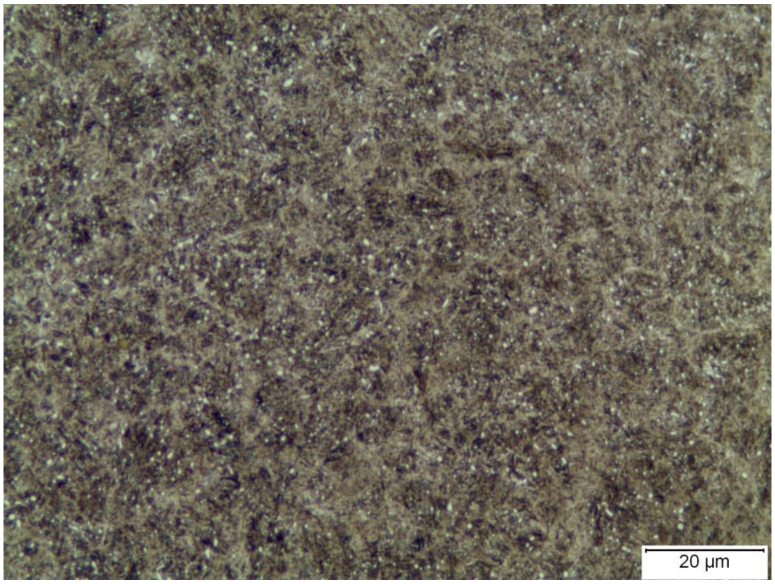

Figure 3.43 Microstructure in Region 1 of 4.0 GPa/10^8 cycles 52100 sample showing no change.

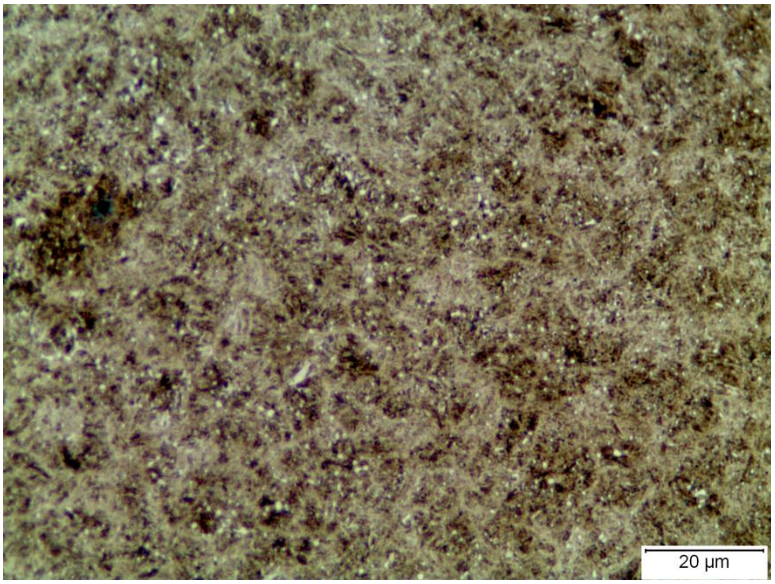

Figure 3.44 Microstructure in Region 2 of 4.0 GPa/10^8 cycles 52100 sample showing no change.

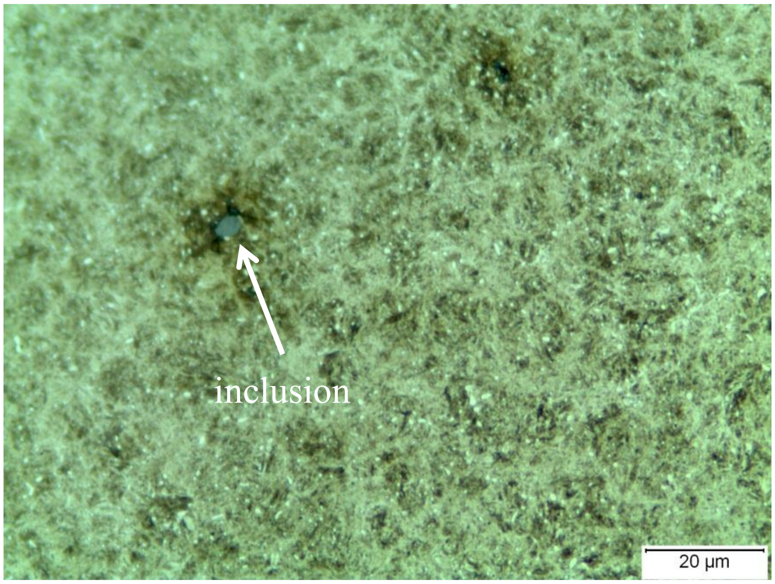

Figure 3.45 Microstructure in Region 3 of 4.0 GPa/10^8 cycles 52100 sample showing no change microstructural change but this image contains an inclusion (most likely alumina).

In both the 4.0 GPa and 4.5 GPa 52100 samples, no microstructural alterations were observed. The 4.5 GPa 52100 sample incurred spalling during the RCF test, but the 4.0 GPa sample did not. Even though the 4.0 GPa tested sample had a lower load, 4.0 GPa is still a high enough to expect spalling at 10^8 cycles. Based on previous literature, white etching bands had been formed in 52100 steel at loads lower than 4.0 GPa and tested to10^8 cycles. Because of this, white etching bands were expected to be observed in these samples.

The 52100 cylindrical rod was first run at 4.5 GPa/10^8 cycles, and after investigating the microstructure and not observing white etching bands, it was hypothesized that the WEBs may have been present but are indeed associated with failure and were in the material that had spalled off the surface. With that in mind, the 52100 cylindrical rod was then tested at 4.0 GPa/10^8 cycles, but again no WEBs were observed and this time, there was no spalling.

This alludes to the fact that the formation of WEBs is still not completely understood. If they formed due to plastic deformation, shear stresses, and carbon diffusion, as stated in the introduction, they would have been observed in these test specimens. If the mechanisms of transformation were completely understood, researchers would be able to repeatedly form them. These tests proved, however, that is not the case.

The following figures represent the hardness data collected in Regions 1, 2, and 3 in the 4.5 GPa/10^8 cycles 52100 sample and the 4.0 GPa/10^8 cycles 52100 sample, followed by a comprehensive table with all the corresponding average hardnesses and standard deviations.

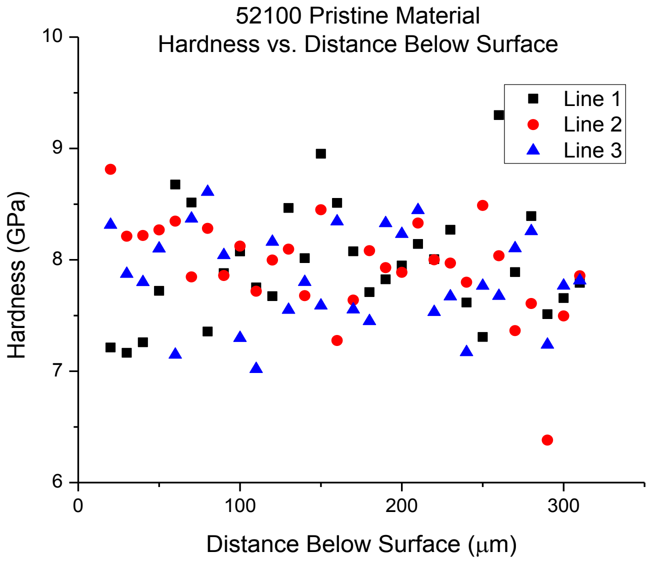

Figure 3.46 Hardness measurements as a function of depth below the surface in a pristine 52100 specimen.

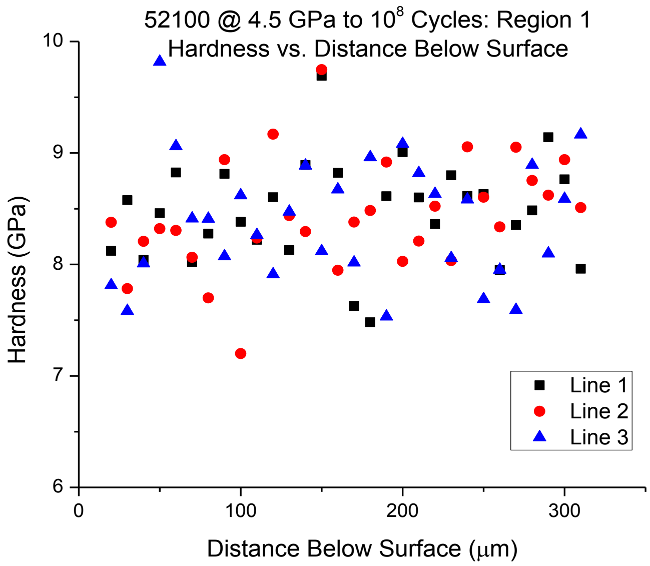

Figure 3.47 Hardness measurements as a function of depth below the surface in Region 1 of the 4.5 GPa loaded to 10^8 cycles 52100 sample.

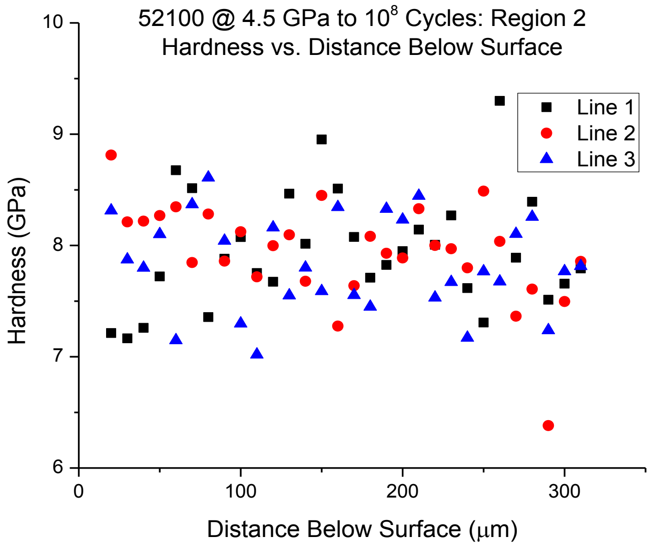

Figure 3.48 Hardness measurements as a function of depth below the surface in Region 2 of the 4.5 GPa loaded to 10^8 cycles 52100 sample.

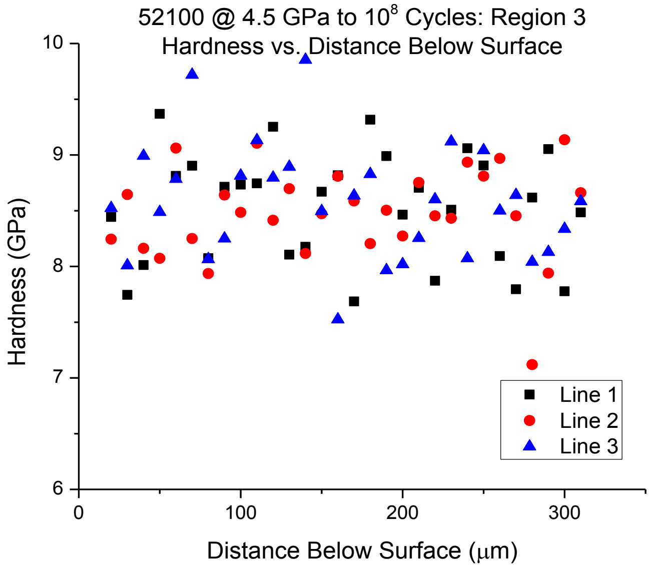

Figure 3.49 Hardness measurements as a function of depth below the surface in Region 3 of the 4.5 GPa loaded to 10^8 cycles 52100 sample.

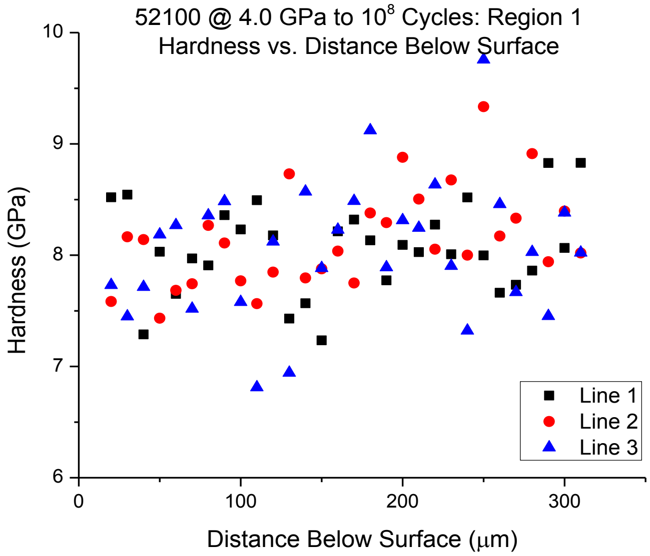

Figure 3.50 Hardness vs. distance below surface in Region 1 of the 4.0 GPa loaded sample to 10^8 cycles.

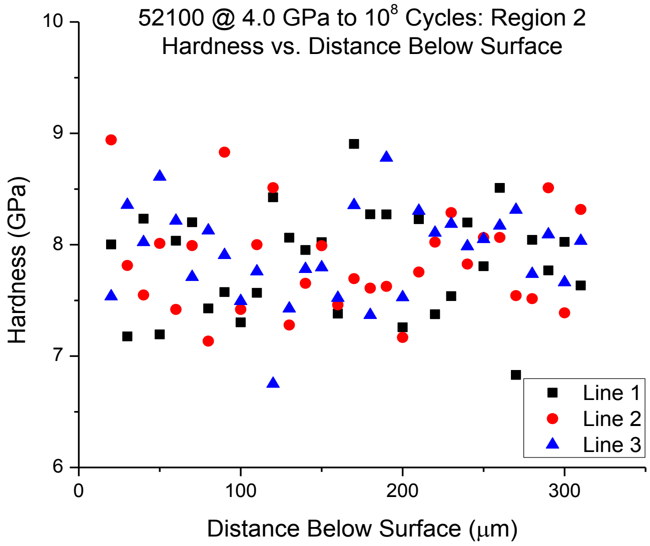

Figure 3.51 Hardness vs. distance below surface in Region 2 of the 4.0 GPa loaded sample to 10^8 cycles.

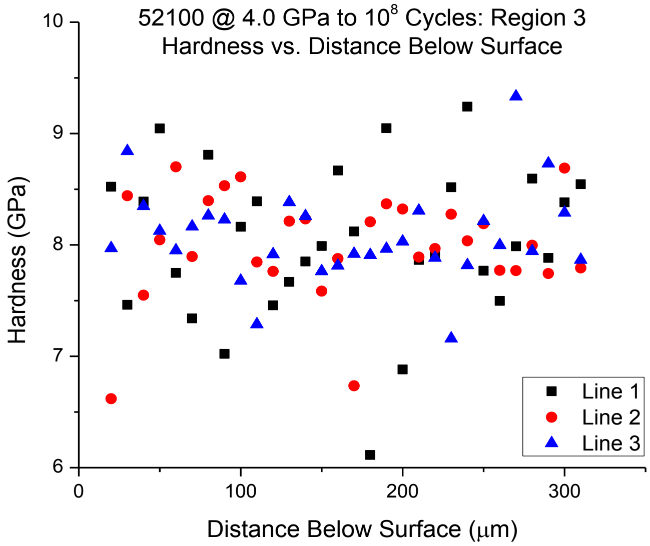

Figure 3.52 Hardness vs. distance below surface in Region 3 of the 4.0 GPa loaded sample to 10^8 cycles.

Table 3.7 Comprehensive hardness table of the different regions for the 4.0/4.5 GPa 52100 samples.

Sample	Average Hardness (GPa)	Std. Deviation
Pristine	7.91	0.41
4.5 52100 Region 1	8.44	0.5
4.5 52100 Region 2	8.01	0.45
4.5 52100 Region 3	8.51	0.41
4.0 52100 Region 1	8.07	0.39
4.0 52100 Region 2	7.89	0.42
4.0 52100 Region 3	8.05	0.38

Similar to the hardness vs. distance below surface graphs of the M50 samples, none of the 52100 regions show a hardness trend relative to the depth below the surface. All of the average hardness values are within a standard deviation of each other and therefore are not statistically different. The Hertzian pressures applied in both tests were high enough to induce plastic deformation within the material. Because of that, a change in hardness would have been expected in the region of maximum shear stress, but that did not occur.

CHAPTER 4. CONCLUSIONS AND FUTURE RECOMMENDATIONS

Four cylindrical rods of M50 and one cylindrical rod of 52100 (two locations) were tested in a rolling contact fatigue test using a 3 ball-on-rod fatigue tester. All samples were subject to 10^8 cycles with two M50 rods (one lubricated, one unlubricated) loaded at 4.5 GPa, two loaded at 5.0 GPa (one lubricated, one unlubricated), one 52100 sample (lubricated) loaded at 4.5 GPa, and one 52100 sample (lubricated) at 4.0 GPa. These experiments were performed to attempt to produce microstructural alterations, specifically dark etching regions and white etching bands, and then to use nanoindentation to characterize these alterations as a function of depth within the surface and position within the wear track.

4.1 Microstructural Alterations

The only samples to produce any microstructural alterations were the M50 rods loaded to 4.5 GPa in which butterflies were produced. No definitive white etching bands were formed in any sample, however, what appeared to be the nucleation of white etching bands were observed in Region 3 of the 4.5 GPa lubricated M50 sample. A higher density of butterflies as well as larger butterflies were observed in the unlubricated sample relative to the lubricated sample. In both samples, the butterflies typically formed an angle of approximately 30° relative to the surface in the rolling direction. White etching bands originally appeared to be present due to no inclusion being observed however, after performing a serial sectioning experiment, they were revealed to be butterflies.

4.2 Hardness

A hardness matrix of 3 columns by 30 rows was performed in Regions 1, 2, and 3 of each sample previously mentioned (with the exception of the 4.5 GPa unlubricated M50 sample) as well as pristine material for both M50 and 52100. Butterfly wings and regions of the possibly nucleated white etching bands were also investigated using scanning probe microscopy.

There was a drop in average hardness observed in the 4.5 GPa lubricated M50 sample from the pristine material to Region 1 of approximately 1.8 GPa. Then, there was an increase in hardness from Region 1 to Region 2 of approximately 0.6 GPa and Regions 2 and 3 had approximately the same average hardness values. No change in hardness was observed in the 5.0 GPa lubricated/unlubricated samples throughout any region. However, the area of interest beneath the surface of the 5.0 GPa M50 samples was spalled off. There were no hardness changes observed in either the 4.0 GPa or 4.5 GPa 52100 samples.

Using scanning probe microscopy, the butterfly wings were investigated and found to have a significantly higher hardness value than that of the surrounding matrix.

The areas containing the possible nucleated white etching bands did not appear to show any specific trend in hardness.

It was concluded that nanoindentation was the better method for evaluating hardness with the specific sample geometry. Nanoindentaiton is also the better method to probe the microstructural alterations that occur due to the indent size. However, to produce more accurate matrix hardness results with less scatter, it is believed that microindentation should be the method of choice since it samples a larger area.

4.3 Suggestions for Future Work

The majority of bearings in which DER and WEBs were observed were in deep groove ball bearings made from 52100 steel. As this is the case, an interesting experiment would be to take ‘x’ number of 52100 cylindrical bars tested at different loads and cycles that previously have corresponded to the formation of microstructural alteration and compare them to ‘x’ number of 52100 deep groove ball bearings tested at the same different loads and cycles as the cylindrical bars. This would allude to whether or not the geometry and possibly size of the rolling contact parts play a role in microstructural alteration formation. It would be important to try to keep other experimental factors consistent if possible such as the type of lubrication, the surface roughness of the parts, and the temperature if possible.

Alternatively, if dark etching regions and white etching bands are indeed produced, using nanoindentation to characterize the hardness of those alterations would be helpful. Even though hardness vs. depth has been completed in the past, the finer indentation spacing would allow more indents to be taken in the region of interest and be completely localized within the band itself. The hardness of the white etching bands could be analyzed to see if hardness within the bands changes as a function of depth, i.e. stress levels experienced.

LIST OF REFERENCES

LIST OF REFERENCES

1 A. Warhadpande, “An Elastic-Plastic Finite Element Model for Rolling Contact Fatigue”; Purdue University, 2012.

2 A. Bhattacharyya, G. Subhash, and N. Arakere, “Evolution of subsurface plastic zone due to rolling contact fatigue of M-50 NiL case hardened bearing steel,” *Int. J. Fatigue*, **59** 102–113 (2014).

3 F. Sadeghi, B. Jalalahmadi, T.S. Slack, N. Raje, and N.K. Arakere, “A Review of Rolling Contact Fatigue,” *J. Tribol.*, **131** [4] 041403 (2009).

4 T.E. Tallian, “Rolling Contact Fatigue,” *Ball Bear. J.*, [217] 5–13 (1983).

5 T.A. Harris, *Rolling Bearing Analysis*, 4th ed. John Wiley & Sons, Inc., 2001.

6 J. Seo, S. Kwon, H. Jun, and D. Lee, “Numerical stress analysis and rolling contact fatigue of White Etching Layer on rail steel,” *Int. J. Fatigue*, **33** [2] 203–211 (2011).

7 A.S. Pandkar, N. Arakere, and G. Subhash, “Microstructure-sensitive accumulation of plastic strain due to ratcheting in bearing steels subject to Rolling Contact Fatigue,” *Int. J. Fatigue*, **63** 191–202 (2014).

8 H.K.D.H. Bhadeshia, “Steels for bearings,” *Prog. Mater. Sci.*, **57** [2] 268–435 (2012).

9 L. Carter, E. V Zaretsky, W.J. Anderson, and L. Thomas, “Effect of hardness and other mechanical properties on rolling-contact fatigue life of four high-temperature bearing steels,” (1960).

10 E. V Zaretsky, “Rolling Bearing Steels — A Technical and Historical Perspective,” [April] (2012).

11 A.P. Voskamp and G.E. Hollox, “Failsafe Rating of Ball Bearing Components”; pp. 102–112 in *ASTM*. 1988.

12 G. Krauss, *Steels: Processing, Structure, and Performance*. ASM International, 2005.

13 E. V Zaretsky, “Selection of Rolling-Element Bearing Steels for Long-Life Applications,” *ASTM*, **STP 987** (1988).

14 E.N. Bamberger, “Materials for Rolling Element Bearings”; pp. 1–46 in *Bear. Des. Asp. Present Technol. Futur. Probl.* The American Society of Mechanical Engineers, 1980.

15 W.T. H.J. Boehmer, F.J. Ebert, “M50NiL Bearing Material-Heat Treatment, Material Properties and Performance in Comparison with M50 and RBD,” *J. Soc. Tribol. Lubr. Eng.*, 28–35 (1992).

16 R. Österlund and O. Vingsbo, “Phase changes in fatigued ball bearings,” *Metall. Trans. A*, **ll** [May] (1980).

17 A.C. Ugural and S.K. Fenster, *Advanced Mechanics of Materials and Applied Elasticity*, 5th ed. 2012.

18 K.L. Johnson, *Contact Mechanics*. n.d.

19 R.G. Budynas and J.K. Nisbett, *Shigley's Mechanical Engineering Design*, 8th ed. 2005.

20 A.. Jones, “Metallographic observations of ball bearing fatigue phenomena”; pp. 35–52 in Philadelphia, 1947.

21 R. Zwirlein and R.C.F. Mech-, “Rolling Contact Fatigue Mechanisms — Accelerated Testing Versus Field Performance,” 358–379 (1982).

22 L.M. Keer and I.A. Polonsky, “ON WHITE ETCHING BAND FORMATION BEARINGS other microstructural changes , are directly related to fatigue failure of bearings . noticeable change in the mode of fatigue spa11 propagation . Fatigue cracks , regardless formation is considered . Based on the ,” **43** [4] (1995).

23 A. Muroga and H. Saka, “Analysis of rolling contact fatigued microstructure using focused ion beam sputtering and transmission electron microscopy observation,” *Scr. Metall. Mater.*, **33** [1] 151–156 (1995).

24 N. Mitamura, H. Hidaka, and S. Takaki, “Microstructural Development in Bearing Steel during Rolling Contact Fatigue,” *Mater. Sci. Forum*, **539-543** 4255–4260 (2007).

[25] R.S. Hyde, "Contact Fatigue of Hardened Steels"; pp. 691–703 in *ASM Handbook, Vol 19 Fatigue Fract.* ASM International, 1996.

[26] J.-H. Kang, B. Hosseinkhani, and P.E.J. Rivera-Diaz-del-Castillo, "Rolling Contact Fatigue in bearings: multiscale overview," *Mater. Sci. Technol.*, **28** (2012).

[27] A.P. Voskamp, "Material Response to Rolling Contact Loading," [84] (1985).

[28] A.P. Voskamp, R. Osterlund, P.C. Becker, and O. Vingsbo, "Gradual changes in residual stress and microstructure during contact fatigue in ball bearings," [January] 14–21 (1980).

[29] K. Sugino, K. Miyamoto, M. Nagumo, and K. Aoki, "Structural Alterations of Bearing Steels," *Trans. Iron Steel Inst. Japan*, **10** [2] 98– (1970).

[30] A.P. Voskamp and E.J. Mittemeijer, "Crystallographic Preferred Orientation Induced by Cyclic Rolling Contact Loading," **27** [NOVEMBER] (1996).

[31] J. Beswick, A. Voskamp, and J. Sanden, "Bearing material/treatment developments at the SKF engineering and research centre," *ASTM Int.*, 222–234 (1991).

[32] H. Schlicht, E. Schreiber, and O. Zwirlein, "Effects of Material Properties on Bearing Steel Fatigue Strength"; in *Eff. Steel Manuf. Process. Qual. Bear. Steels, ASTM STP 987*. 1986.

[33] V. Bhargava, G. Hahn, and C. Rubin, "Rolling contact deformation, etching effects, and failure of high-strength bearing steel," *Metall. Trans. A*, **21a** (1990).

[34] H. Harada, T. Mikami, M. Shibata, D. Sokai, a. Yamamoto, and H. Tsubakino, "Microstructural Changes and Crack Initiation with White Etching Area Formation under Rolling/Sliding Contact in Bearing Steel," *ISIJ Int.*, **45** [12] 1897–1902 (2005).

[35] R. Osterlund, M. Aucouturier, and O. Vingsbo, "High-Resolution Autoradiography Determination of Carbon Diffusion during Rolling-Contact Fatigue in Ball-Bearings," *Scand. J. Metall.*, **10** 67–72 (1981).

[36] N.H. Forster, L. Rosado, W.P. Ogden, and H.K. Trivedi, "Rolling Contact Fatigue Life and Spall Propagation Characteristics of AISI M50, M50 NiL, and AISI 52100, Part III: Metallurgical Examination," *Tribol. Trans.*, **53** [1] 52–59 (2009).

[37] A.D.E. Martin, J A, S.F. Borgese, "Miorostructural Alterations of Rolling — Bearing Steel Undergoing Cyclic Stressing," *J. Basic Eng.*, [65] (1966).

[38] J. Beswick, “Measurements of carbon levels in structurally transformed SAE 52100 ball bearing steel by microprobe analysis,” (1975).

[39] T. Lund, “Structural Alterations in Fatigue-Tested Ball-Bearing Steel,” *Jernkontorets Ann.*, **153** [7] 337–343 (1969).

[40] H. Swahn, “Martensite Decay During Rolling Contact Fatigue in Ball Bearings,” **7** [August] (1976).

[41] a. Grabulov, U. Ziese, and H.W. Zandbergen, “TEM/SEM investigation of microstructural changes within the white etching area under rolling contact fatigue and 3-D crack reconstruction by focused ion beam,” *Scr. Mater.*, **57** [7] 635–638 (2007).

[42] P.C. Becker, “Microstructural changes around non-metallic inclusions caused by rolling-contact fatigue of ball-bearing steels,” 234–243 (1981).

[43] W.D.J. Callister, *Materials Science and Engineering an Introduction*, 7th ed. 2007.

[44] D.V. Wilson, “Effects of plastic deformation on carbide precipitation in steel,” (1957).

[45] T. Ochi, H. Kanisawa, K. Ooki, and Y. Kusano, *Change in Microstructure and Properties in the Rolling Contact Fatigue of Bearing Steel*. 1999.

[46] R.G.H. Bush, J.J., Grube W.L., “Microstructural and Residual Stress Changes in Hardened Steel Due to Rolling Contact,” *Trans. Am. Soc. Met.*, **54** 390–412 (1961).

[47] a. Grabulov, R. Petrov, and H.W. Zandbergen, “EBSD investigation of the crack initiation and TEM/FIB analyses of the microstructural changes around the cracks formed under Rolling Contact Fatigue (RCF),” *Int. J. Fatigue*, **32** [3] 576–583 (2010).

[48] T.Y.-M. Hui, “Performance Characteristics of Jet Fuel in Heavily Loaded Contacts”; Purdue University, 2006.

[49] A. Iqbal and M.S. Baig, “European Journal of Scientific Research,” (2007).

[50] D. Glover, “A Ball-Rod Rolling Contact Fatigue Tester”; pp. 107–124 in *Roll. Contact Fatigue Test. Bear. Steels*. Edited by J. Hoo. ASTM International, 100 Barr Harbor Drive, PO Box C700, West Conshohocken, PA 19428-2959, 1982.

[51] W.C. Oliver and G.M. Pharr, "An Improved Technique for Determining Hardness and Elastic Modulus using Load and Displacement Sensing Indentation Experiments," *J. Mater. Res.*, **7** (1992).

[52] J. Bridge, G. Maniar, and T. Philip, "Carbides in M-50 high speed steel," *Metall. Mater. Trans.* , **2** [August] 2209–2214 (1971).

[53] G. Roberts, G. Krauss, and R. Kennedy, *Tool Steels*, 5th ed. ASM International, 1998.

[54] S. Zafferer, *Phase Identification of Carbide Precipitates*. n.d.

[55] G. Vander Voort, *Revealing Prior-Austenite Grain Boundaries in Heat Treated Steels*, (n.d.).